Analytical Techniques for Short-Term Ocean Current Forecasting

Andrew James White

University College London
University of London

A thesis submitted for the degree of

Doctor of Philosophy.

October 2004

Supervisors

Dr. N.R. McDonald
Prof. J. Stark

ProQuest LLC
789 East Eisenhower Parkway
P.O. Box 1346
Ann Arbor, MI 48106-1346

Abstract

This thesis concerns the motion of oceanic vortices and comprises two parts. Part I examines the dynamics of point vortices in a two-layer fluid near large amplitude, sharply varying topography, e.g. continental shelf regions. Topography takes the form of an infinitely long step change in depth and the two-layer stratification is chosen such that the height of topography in the upper layer is a small fraction of the overall depth, enabling quasi-geostrophic theory to be used in both layers even though the topography is large amplitude. An analytic expression for the dispersion relation of free topographic waves in this system is found. Weak lower-layer vortices are studied using linear theory and, depending on their sign, are able to produce significant topographic wave radiation in their wakes. Upper-layer vortices produce relatively small amplitude topographic wave radiation. Contour dynamics results are used to investigate the nonlinear regions of parameter space. For lower-layer vortices linear theory is a good approximation, but for upper-layer vortices complicated features evolve and linear theory is only valid for weak vortices. The motion of hetons (two vortices, one in each layer) and dipoles are also studied.

Part II involves the investigation and prediction of the motion of Loop Current Eddies (LCE's) in the Gulf of Mexico. By incorporating the major features of LCE's into a simple eddy model it is attempted to discover if it is possible to deduce the characteristics of a distant eddy from a set of measured velocities at a fixed location and further, predict the subsequent motion of the eddy. First, a circular model for the eddy shape is adopted and the Helmholtz equation is solved in the far-field. Second, a more sophisticated, precessing, elliptical model is developed, the solution involving Mathieu functions. In both cases comparison with actual current meter data is used to demonstrate the validity of the models.

Acknowledgements

I am grateful to my supervisors Dr. Robb McDonald and Professor Jaroslav Stark for their constant support, advice and many comments improving this thesis. I am particularly indebted to Dr. McDonald for initially encouraging me to embark on these thoroughly rewarding years of research.

Acknowledgement is made to Fugro GEOS for financial assistance and in particular to Gus Jeans and Robin Stephens for their guidance and help obtaining valuable data. Further, I wish to thank those at BHP Billiton for making the data available and going out of their way to assist me.

I also gratefully acknowledge the financial support of EPSRC and of the Marine Information Council.

Finally, I appreciate the backing of friends and family, especially to Andrea who has had to put up with me for the last few years!

Contents

List of Figures

Chapter 1

Overview

The theme central to this research is the motion of vortices (sometimes termed eddies) and the interaction of these vortices with the surrounding fluid. Vortices and patches of vorticity are rotating, often large, long lived, structures common in both the oceans and the atmosphere. For instance, the Loop Current system in the eastern Gulf of Mexico periodically sheds large, anticyclonic vortices called Loop Current Eddies. These Loop Current Eddies are on average, approximately 300 km in diameter and have a life span of about one year, see Elliott [1982] (Loop Current Eddies will be discussed in more detail in part II.). Similarly, the Agulhas Retroflection produces warm eddies which drift into the south Atlantic off the south coast of Africa. The so called Agulhas Rings have been observed to have diameters of 400 km and have residence times in the south Atlantic of 3–4 years (Byrne et al. 1995). Figure 1.1 shows evidence of Agulhas Rings in the Atlantic Ocean from satellite sea surface altimeter data. The figures on the contours indicate the depth (in metres) of the upper layer of the ocean. Several large, localised, relatively deep upper-layer regions are indicative of Agulhas Rings which correspond to significant veloc-

ity signatures up to 700 m into the ocean. The area shown also encompasses large and significant topographic features, e.g. the Walvis ridge runs roughly north-south along a longitude of 5°E.

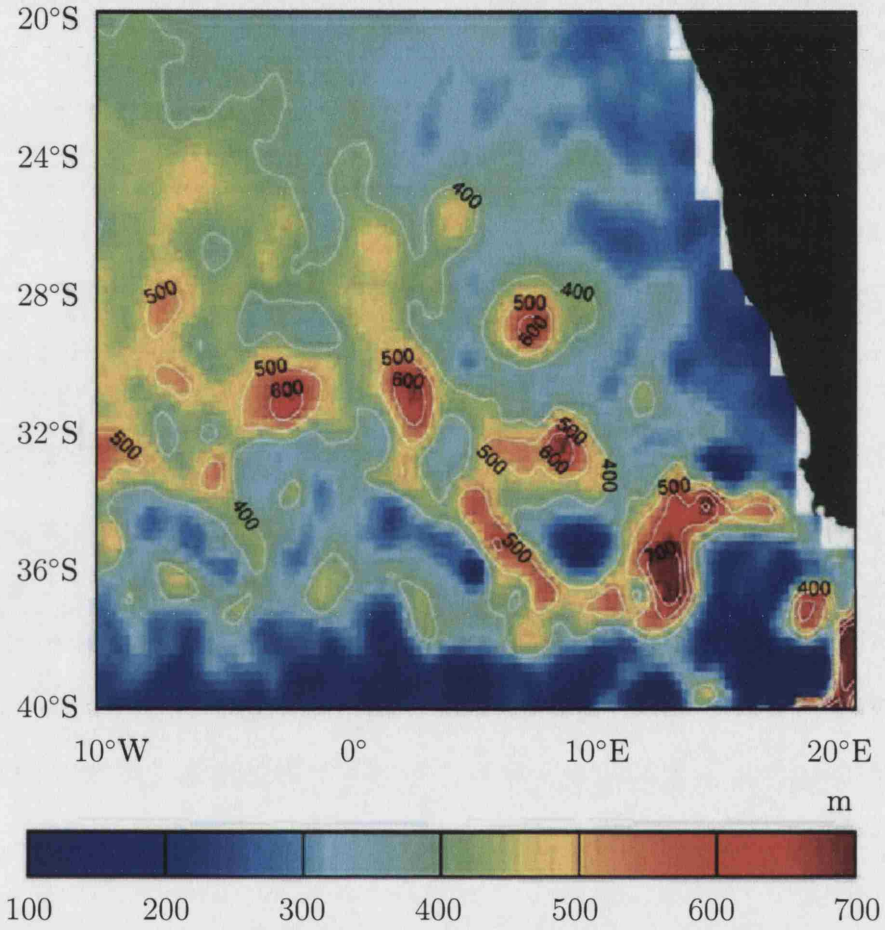

Figure 1.1: Agulhas Rings depicted in the layer thickness derived from altimeter data (TOPEX/POSEIDON and ERS) and World Ocean Atlas (1998) hydrographic data during September 26, 1999.

An example of an atmospheric vortex is the wintertime polar vortex (McIntyre 1995). This vortex is situated in the stratosphere, and can affect the chemistry of ozone depletion.

This thesis will concentrate on the motion of oceanic vortices. These vor-

tices are extremely important as they possess the ability to self-propagate and can, therefore, transport vast quantities of heat, salt and momentum, large distances throughout the oceans. For example, typical Agulhas Rings transport 2.2 to 3.3 $\times 10^{20}$ J yr^{-1} of heat and 14 to 21 $\times 10^{12}$ kg yr^{-1} of salt and are responsible for a mass transfer of 2.6 to 3.8 $\times 10^{6}$ m^3 s^{-1} from the Indian to the Atlantic Ocean (Duncombe Rae et al. 1996). A number of factors affect the propagation speed and direction of vortices. These include the effects of the curvature of the rotating Earth (the β-effect), the local topography, the influence of other nearby vortices and advection by the surrounding mean flow. Loop Current Eddies and Agulhas Rings generally translate westward, owing to the β-effect (McDonald 1999), at a rate of between approximately 2 and 10 cm s^{-1} ($\approx$ 2–9 km day^{-1}, Hamilton et al. 1999 and Byrne et al. 1995). Note that the translation speed of Agulhas Rings varies significantly when they encounter the topography of the Walvis ridge (Byrne et al. 1995). Such variations in vortex behaviour owing to topography are crucial in determining their transport properties and are a motivation for this study.

Knowledge of the motion of vortices is therefore of great importance. Predicting the paths of oceanic vortices and the large currents they can induce has applications to the shipping and off-shore oil industries where there is potential for environmental disaster and loss of life. Also, since oceanic vortices redistribute large amounts of salt and heat, they play a significant role in determining the weather and have been linked to climate change. For example, de Ruijter et al. [1999] postulate that the shut off of production of Agulhas Rings may have led to a cessation of important Atlantic circulations and subsequent climate change. More obviously, intense atmospheric vortices such as tropical cyclones, can be devastating natural phenomena.

This thesis consists of several parts. Part I comprises chapters 2 to 7 and is concerned with the motion of various vortex configurations near large amplitude topography in a two-layer fluid. As already mentioned, the local topography is an important factor in determining the trajectories of vortices. In such regions the effects of the local planetary curvature can be neglected in favour of those of the sharply varying topography. The motion of isolated vortices and different combinations of two vortices in two fluid layers are considered. Further, the effects of the presence of the vortices on the fluid overlying the topography is discussed in detail. Included in this part are chapters 3 and 4, which form the basis of a paper that has been accepted for publication in the *Journal of Physical Oceanography* (White and McDonald 2004).

Part II consists of chapters 8 to 11 and investigates the modeling and prediction of the motion of Loop Current Eddies in the Gulf of Mexico. The Gulf of Mexico is a particularly oil rich region and therefore predicting the motion of these large current inducing vortices is of great practical importance to the day-to-day running of offshore oil recovery operations. Models are developed to simulate a Loop Current Eddy and applied to actual Gulf of Mexico data to test their validity.

Part I

The motion of some point vortex configurations near large amplitude topography in a two-layer fluid

Chapter 2

Introduction and review

This chapter aims to give an overview of some of the literature that forms the basis of this part of the research, namely the motion of configurations of point vortices near large amplitude topography in a two-layer fluid. The fundamental principles governing large scale rotating flows are introduced and the main concepts explained before a review of preceding work more specific to the problem considered here is presented.

The Coriolis force and governing equations

The dynamics of fluid motions on the Earth are best described in a reference frame fixed relative to the surface of the rotating Earth. The effect of the rotation gives rise to the apparent force known as the Coriolis force. This force acts at right-angles to the direction of the fluid velocity and the Coriolis parameter, f, measures its variation with the sine of the latitude, ϕ. This thesis studies fluid dynamics near mid-latitudes. In such regions the Coriolis parameter is approximated by a constant based on some mean latitude, ϕ_0,

plus a linear variation in the local north-south (y) coordinate, i.e.

$$f \approx f_0 + \beta y, \tag{2.1}$$

where $f_0 = 2\Omega_E \sin\phi_0$, Ω_E being the angular velocity of the Earth and

$$\beta = \frac{2\Omega_E}{r_E} \cos\phi_0, \tag{2.2}$$

where r_E is the radius of the Earth. This approximation is called the β-plane approximation and the motions it gives rise to, the β-effect. In this work the β-effect will be negligible compared to other factors but it will be useful to compare the motion of vortices near topography to that of vortices on the β-plane, since their dynamics are, in many instances, analogous. An overview of vortex motion on a β-plane is given in McDonald [1999]. In general, vortices tend to drift in the westward direction. In both hemispheres, the β-effect causes the westward drift of anticyclonic and cyclonic vortices. This mechanism is described later (see also McDonald 1999 for a physical explanation). The evolution of an intense finite area vortex can be described in three distinct stages. In the first stage the vortex is accelerated westward by the β-effect. In the second stage the vortex decelerates due to secondary circulations and finally the vortex is distorted so much by these secondary circulations that it is destroyed. Characterising time scales in this way, Reznik et al. [2000] analytically and numerically estimate the lifetime of intense vortices and show why large time vortex motion can be well approximated by simply examining the initial β-effect stage.

The fluid motions considered in this part (and also in part II) occur over large length scales compared with the depth of the ocean. For instance, Loop Current Eddies may travel the entire width of the Gulf of Mexico, a distance of some 650 km, the depth of which is a maximum of about 3500 m. On such

length scales, the ocean can be thought of as a thin rotating shell on a solid rotating sphere and the traditional equations of motion can be approximated by the shallow water equations, see Pedlosky [1987] for a derivation of these equations. In a homogeneous, inviscid fluid the shallow water equations are

$$\frac{\partial \boldsymbol{u}}{\partial t} + (\boldsymbol{u} \cdot \nabla)\,\boldsymbol{u} + f\boldsymbol{k} \times \boldsymbol{u} = -g\nabla h, \tag{2.3}$$

and

$$\frac{\partial H}{\partial t} + \nabla \cdot (\boldsymbol{u}H) = 0. \tag{2.4}$$

Here $\boldsymbol{u} = (u, v)$ is the horizontal component of the velocity and $H(x, y, t) = h(x, y, t) - h_B(x, y)$ is the thickness of the fluid layer, where h is the deviation of the free surface from a flat position and h_B is the bottom topography. The acceleration due to gravity is $-g\boldsymbol{k}$. The independent variables x, y, are the horizontal coordinates and t is the time variable.

Cross differentiating the two components of the momentum equation (2.3), subtracting and defining the relative vorticity (to an observer in the rotating frame) by, $\zeta = v_x - u_y$, gives

$$\frac{\partial \zeta}{\partial t} + u\frac{\partial \zeta}{\partial x} + v\frac{\partial \zeta}{\partial y} = -(\zeta + f)\left(\frac{\partial u}{\partial x} + \frac{\partial v}{\partial y}\right), \tag{2.5}$$

or

$$\frac{D}{Dt}\left(\frac{\zeta + f}{H}\right) = 0, \tag{2.6}$$

where

$$\frac{D}{Dt} \equiv \frac{\partial}{\partial t} + (\boldsymbol{u} \cdot \nabla), \tag{2.7}$$

is the advective derivative. The quantity $(\zeta + f)/H$ is called the potential vorticity. Expression (2.6) is central to the work presented in this part and indeed the subject of geophysical fluid dynamics in general. It states that potential vorticity is conserved, i.e. any changes in the depth of the fluid or

the planetary vorticity field must be compensated for by an appropriate change in the relative vorticity. For example, figure 2.1 depicts a perturbed interface between two regions of different (constant) potential vorticity, which may arise from a change in the topography (H) or the background shear in the velocity field. Fluid which has been advected from the region of low potential vorticity to higher potential vorticity must acquire negative relative vorticity to conserve its potential vorticity. This corresponds to a local clockwise circulation, shown by the circular arrow. (Note, throughout this thesis, directions of rotation are described as applied to the northern hemisphere, i.e. clockwise flow coincides with anticyclonic rotation.) Similarly fluid which has been advected into the region of low potential vorticity gains positive relative vorticity and circulates anticlockwise. The initial disturbance is advected by these circulations (as shown by the dashed perturbation) and subsequently propagates with higher potential vorticity to the right as indicated by the arrow. Several types of waves

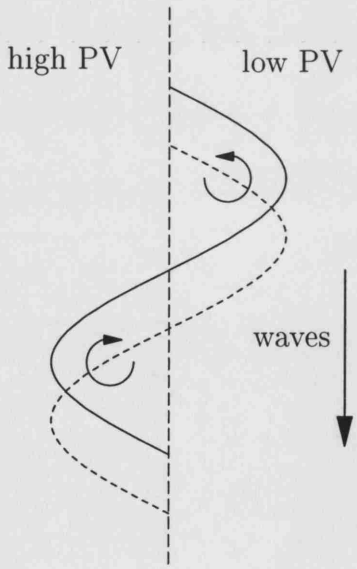

Figure 2.1: Mechanism of wave generation by potential vorticity conservation. The waves propagate with higher potential vorticity to the right.

can be generated by this mechanism, one example of which is the Rossby wave where the β-effect gives rise to the necessary background potential vorticity gradient. Rossby waves have recently been observed in the ocean, see for example Chelton and Schlax [1996] and Cipollini et al. [1997]. Another class of waves which arise due to the mechanism depicted in figure 2.1 are continental shelf waves (Gill 1982). The background potential vorticity gradient in this case is provided by changes in the bottom topography.

An important parameter in the study of geophysical fluid dynamics is the Rossby number,

$$Ro = \frac{U}{f_0 L}, \tag{2.8}$$

where U is a typical velocity and L is a typical length scale. The Rossby number measures the importance of the Earth's rotation compared with the advective dynamics of the problem under consideration. For example, for Agulhas Rings $Ro \approx 0.1$ (McDonald 1999) and therefore the Earth's rotation plays a significant role in their evolution. The flows considered in this thesis will all have the property that the Rossby number is small. However in most cases, the variation in the background potential vorticity will be contributed to mostly by changes in topography rather than the β-effect which arises due to variations of the Coriolis force with latitide (see chapter 3). For small Rossby numbers the leading order balance in a rotating fluid is geostrophy, where the horizontal pressure gradient is matched by the horizontal Coriolis acceleration. Small departures from this state will be of interest here and are called quasi-geostrophic dynamics. In this case, the shallow water equations can be rescaled by expanding in a series using the Rossby number as the small parameter, see Pedlosky [1987] for details. This leads to the conservation relation,

$$\frac{DQ}{Dt} = 0, \tag{2.9}$$

where Q is the (here, non-dimensional) quasi-geostrophic potential vorticity (compare with equation (2.6)) expressed in terms of a streamfunction, ψ, i.e.

$$Q = \begin{cases} \nabla^2\psi + sh_B, & \text{in a single layer with a rigid lid,} \\ \nabla^2\psi - \psi + sh_B, & \text{in a single layer with a free-surface,} \end{cases} \tag{2.10}$$

where the β-effect is assumed to be negligible and s is a dimensionless parameter quantifying the effect of the topography, h_B, on the flow. Note that the work presented in this part concerns fluid that can consist of either one or two layers and the quasi-geostrophic potential vorticity, Q, has a different form accordingly, i.e. either, or both, definitions of the potential vorticity in (2.10) are required to describe the flow.

The dynamics of vortices in quasi-geostrophic regimes have been extensively studied. For example, the motion of singular and intense vortices on a β-plane have been studied analytically by Reznik [1992] and Sutyrin and Flierl [1994] respectively and more recently by Lam and Dritschel [2001] numerically. It should be noted that quasi-geostrophic models are restricted in that the Rossby number must be small and that there exist other models in which this constraint is not required. However, as the previously cited studies indicate, quasi-geostrophic dynamics are useful in modeling vortices and the ocean in general and will be employed in this part of the thesis.

Previous work on vortex-topography interaction

The h_B term in equation (2.10) implies that varying topography plays an important role in the dynamics of ocean currents. Near continental margins such as the Gulf of Mexico the topographic gradients are sufficiently sharp as to be the dominant contributor to variations in the local potential vorticity with planetary curvature, or β-effect, having relatively little impact. This study will

concentrate on such regions and, in particular, how topography influences the trajectories of vortices, or eddies, and the effects of the radiation of topographic waves on their motion. As stated before, the Loop Current system in the eastern Gulf of Mexico periodically sheds eddies. These Loop Current Eddies propagate westward across the Gulf of Mexico before interacting with the steep topography at the Mexican coast (Hamilton et al. 1999). Similarly, Agulhas Rings off the west coast of Africa have been observed (Gründlingh 1995) to interact strongly with local topography, i.e. features such as the Walvis ridge and the south Atlantic mid-ocean ridge. What follows is a brief review of some of the existing literature regarding the interaction of vortices with potential vorticity gradients such as could arise from changes in topography.

In a single layer of fluid McDonald [1998b] has investigated the behaviour of an intense point vortex near an escarpment and Dunn et al. [2001] have studied numerically the motion of moderate and weak point vortices near escarpments. A vortex is said to be intense if the time scale for vortex circulation is much shorter than the time scale for topographic wave generation, i.e. the topography has a relatively small effect compared to advection. For a weak vortex, the reverse is true and topography inhibits transport across the escarpment. Using quasi-geostrophic theory, asymptotic results for both strong and weak vortices show that, at large times, they propagate parallel to the escarpment and topographic wave generation is possible depending on the direction of this propagation. Both these studies show that such wave radiation also leads to a slow drift of the vortex towards or away from the escarpment depending on the sign of the circulation.

Wang [1992] has investigated the motion of one-layer eddies near escarpments of finite non-zero (i.e. not in the quasi-geostrophic limit) height and con-

tinuously varying topography. He finds that cyclones and anticyclones behave differently, i.e. cyclones can cross step-like topography whereas anticyclones are reflected. He shows that it is possible for eddies to generate waves of the type shown in figure 2.1 over the topography.

Stern and Flierl [1987] and Bell [1990] have studied dynamically analogous one-layer problems in which the potential vorticity gradient is provided by a background jet rather than topography. Stern and Flierl [1987] examine the motion of vortices near such jets using quasi-geostrophic theory both analytically and numerically. Distant vortices tend to perturb the edge of the jet. This deformation, in turn, causes the vortex to move parallel but in the opposite direction to the jet. Vortices closer to the jet deform it in a nonlinear way and can capture and wind up the interface of the jet. Further, waves in the wake of the vortex may be excited which cause the vortex to drift towards, or away from, the jet depending on the sign of the vortex circulation. Bell [1990] generalises the vortex-jet interaction problem by solving an initial value problem. Through use of momentum arguments, more complex shear flows can be considered. It is concluded that positive vortices drift in the direction of increasing potential vorticity by radiating Rossby waves.

Numerical simulations of vortex-jet interaction using a three-dimensional, primitive equation model and a one-and-a-half layer fluid with more complex potential vorticity structures have been further considered by Sutyrin et al. [2001] and Vandermeirsch et al. [2003] respectively. Sutyrin et al. [2001] show that meanders in jets grow into waves that can generate eddies at large depths. These deep eddies provide a positive feedback mechanism for the meander growth. However, they also show that the presence of (even weak) topography inhibits the formation of these deep eddies. Vandermeirsch et al. [2003] study

vortex-jet interaction using both quasi-geostrophic and shallow water models. They investigate the effects of increasing the strength of a finite area vortex and extend the work of Stern and Flierl [1987] and Bell [1990] by allowing the vortex to cross the jet. They find, in both models, that weak vortices drift parallel to the jet, stronger vortices cross the jet and tear meanders from it, forming dipoles. Stronger vortices still again cross the jet but only tear a small vortex filament from it.

Zavala Sansón [2002] and Zavala Sansón and van Heijst [2000] have also conducted laboratory experiments of the motion of barotropic vortices near coastal and ridge topography, demonstrating the strong influence of secondary vortex motions induced by potential vorticity conservation. They find marked differences between the behaviour of cyclones and anticyclones. Cyclones drift towards coastal topography situated at a western boundary following a northwesterly path, due to the β-effect (simulated in the laboratory by a uniformly sloping bottom). They are then deflected southwards by the topography. Anticyclones approach in a southwesterly direction (again due to the β-effect) but on encountering coastal topography, tend to drag fluid of oppositely signed vorticity (due to potential vorticity conservation) downslope. This fluid forms a dipole with the anticyclone which then reflects back from the topography in an easterly direction. Strong cyclones interact in a complicated way with ridge topography. On encountering the ridge, several anticyclonic cells of fluid are created due to effects of the topography. These cells act to deform the original cyclone and can in severe cases split it in two.

Dipole formation also occurs when vortex patches encounter seamounts. Using a quasi-geostrophic model, McDonald and Dunn [1999] find that sufficiently strong vortices can sweep fluid off a seamount which subsequently

acquires a cyclonic circulation, again due to the conservation of potential vorticity. If the original vortex is an anticyclone it pairs up with the displaced fluid to form a dipole which propagates away from the seamount. Thus the formation of dipoles is a frequently observed phenomenon in investigations of vortex-topography interaction. Dipole formation and their behaviour near topography is studied in the present work (see chapters 4 and 6).

Vortex-topography interaction in a stratified ocean is less well studied. Beismann et al. [1999] numerically studied the motion of Agulhas Rings near ridge-like topography using a two-layer quasi-geostrophic model. They found that only eddies with a significant dynamic signal in the lower layer were influenced by topography. Such eddies, initially propagating in a northwestward direction, slow down on encountering the north-south oriented ridge-like topography and follow a more northerly path before traversing the ridge in a wide curve. Sufficiently strong topographic slopes can even block the northwesterly translation and force eddies to translate parallel to the topography. More recently Herbette et al. [2003] used a shallow water isopycnic model to study the interaction of a surface vortex with a seamount. They found that deep circulations caused by advection by the vortex of deep fluid parcels across isobaths influenced the trajectory of the vortex and could lead to its erosion through filamentation.

The two-layer ocean

As stated earlier this part of the thesis is concerned with vortices in a two-layer fluid. Two layers are chosen as it permits the use of quasi-geostrophic theory near large amplitude topography (chapter 3) and further, oceans in general are well approximated by two-layer models. See, for example, figure 2.2 in which

the temperature, salinity and density of a typical oceanic region are plotted as functions of depth. In each graph a sharp change in gradient can be seen at about 600 m indicating quite distinct upper and lower portions of the ocean, thus motivating the use of two layers. Gill [1982] and Pedlosky [1987] also argue that two-layer models give rise to fluid motions consistent with observed ocean currents. The model used in this part of the thesis, described later, will

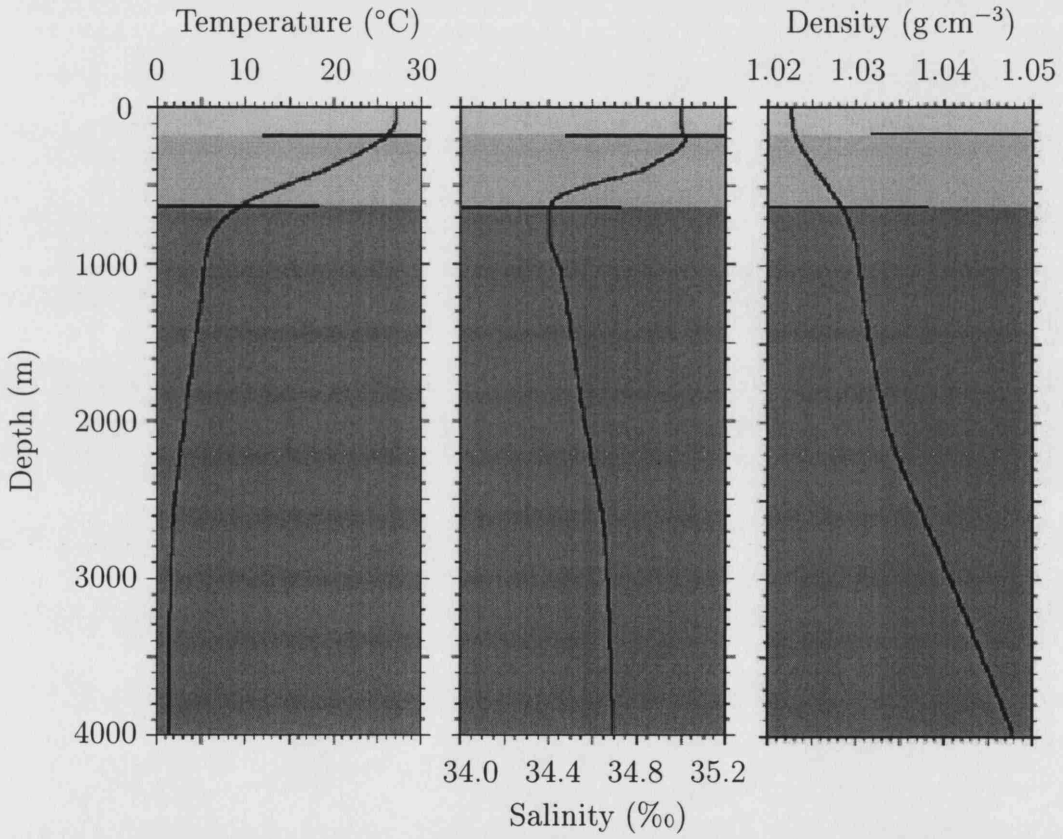

Figure 2.2: Motivation for a two-layer model.

consist of two regions, one with a single layer and one with two layers. In order to make analytical progress, it will therefore be necessary to decompose some of the variables describing the fluid motion into barotropic and baroclinic modes. In the single homogeneous layer, the fluid is said to be barotropic as there are no density differences and the flow is independent of depth. However,

in the two-layer fluid a baroclinic mode is also required to take into account the fact that there is no net depth integrated flow (Gill 1982).

Contour dynamics

The linear theory developed in this part of the thesis is complemented with numerical experiments which are tested by appealing to the linear limit. The contour dynamics algorithm developed by Zabusky et al. [1979] is used to indicate over what region of parameter space, linear theory is a good approximation and further investigate the nonlinear parameter space. Here a brief, general overview of contour dynamics is given. A more detailed description, including specific adaptations relevant to the present work, can be found in chapter 4.

The contour dynamics algorithm integrates the full nonlinear governing equation (2.9). To derive the algorithm, equation (2.9) is restated in a different form. Following Dritschel [1985], the quantity q is defined as

$$q = \mathcal{L}(\psi) \tag{2.11}$$

where ψ is the streamfunction and

$$\mathcal{L} = \begin{cases} \nabla^2, & \text{in a single layer with a rigid lid,} \\ \nabla^2 - 1, & \text{in a single layer with a free-surface.} \end{cases} \tag{2.12}$$

In a two-layer fluid, as will be seen, it is necessary to decompose the upper- and lower-layer streamfunctions into barotropic and baroclinic modes which correspond, respectively, to the $\mathcal{L} = \nabla^2$ and $\mathcal{L} = \nabla^2 - 1$ operators. Equation (2.10) implies

$$Q = q + sh_B, \tag{2.13}$$

i.e. as the topography varies, q and hence (2.11) demands ψ also changes to conserve potential vorticity (2.9). The streamfunction can be expressed by inverting the operator, (2.12), i.e.

$$\psi(x,y) = \iint q(x',y')G(r)dx'dy', \tag{2.14}$$

where $r^2 = (x-x')^2 + (y-y')^2$, the integral is taken over the entire fluid domain and G is the Green's function of $\mathcal{L}$. In particular,

$$G(r) = \begin{cases} \dfrac{1}{2\pi}\log(r), & \text{in a single layer with a rigid lid,} \\ -\dfrac{1}{2\pi}K_0(r), & \text{in a single layer with a free-surface.} \end{cases} \tag{2.15}$$

The velocity field is therefore

$$\boldsymbol{u}(x,y) = (u,v) = \left(-\frac{\partial\psi}{\partial y}, \frac{\partial\psi}{\partial x}\right) = \iint q(x',y')\frac{\partial G}{\partial r}\left(-\frac{\partial r}{\partial y}, \frac{\partial r}{\partial x}\right)dx'dy'. \tag{2.16}$$

Now suppose that the anomalous potential vorticity distribution, q, is piecewise constant in the regions A_k which divide the whole fluid domain, i.e. $q(x,y) = q_k$ if $(x,y) \in A_k$. Then equation (2.16) becomes

$$\boldsymbol{u}(x,y) = \sum_k q_k \iint_{A_k} \frac{\partial G}{\partial r}\left(-\frac{y-y'}{r}, \frac{x-x'}{r}\right)dx'dy'. \tag{2.17}$$

Applying Stokes theorem,

$$\iint_A \left(\frac{\partial R}{\partial x} - \frac{\partial P}{\partial y}\right)dxdy = \int_C Pdx + Rdy, \tag{2.18}$$

where C is the boundary of region A, to u with $P = -G$ and $R = 0$, and to v with $R = -G$ and $P = 0$, gives the velocity field in terms of line integrals,

$$\boldsymbol{u}(x,y) = \sum_k \Delta q_k \int_{C_k} G(r_k)\, d\boldsymbol{x}_k, \tag{2.19}$$

where C_k is the (exterior) boundary of A_k, $\boldsymbol{x}_k = (x_k, y_k)$ is a point on C_k and $r_k^2 = (x-x_k)^2 + (y-y_k)^2$. Further, Δq_k is the jump in the quantity q

across C_k, see Dritschel [1985]. The C_k are called contours and enclose fluid of constant potential vorticity. No fluid can cross these contours and it is easy to follow their time evolution since the velocity at each point (or node) on the contours is given by (2.19). Also, this method is much more computationally efficient than, say, dividing the domain up into a two dimensional grid since there are, at least for relatively simple contours, far fewer nodes.

Figure 2.3 shows how the contours enclose regions of piecewise constant potential vorticity for a flow regime similar to that considered in this part of the thesis. As in figure 2.1, the fluid domain is divided into two areas with different potential vorticities, the boundary denoted by the dashed line. The line of fluid particles (solid line) which initially overlies the divide between these two areas has been perturbed. This line of fluid particles and the boundary between the high and low ambient potential vorticities provide contours enclosing three regions of different (constant) potential vorticity. Fluid in region A_1 has been advected from a region of high potential vorticity to low potential vorticity and vice versa for region A_2. Fluid in regions A_3 has not crossed the boundary and potential vorticity here remains as the initial value. Therefore, only regions A_1 and A_2 contribute to the velocity field and the direction around the contours that the integrations in (2.19) should be performed are indicated by the arrows. Computationally this is achieved by a single contour integral along the perturbed interface followed by one along the straight dashed line representing the topography. Since this latter integration is along an invariant line, it is performed only once in the algorithm with the velocities it produces stored for use when required.

A useful addition to the contour dynamics algorithm is that of contour surgery developed by Dritschel [1988] (see also Dritschel and Ambaum 1997),

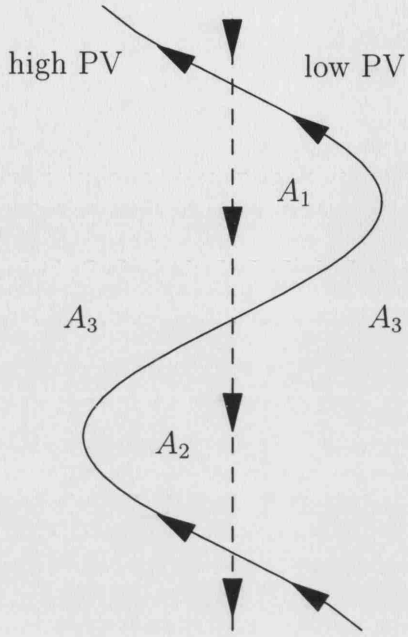

Figure 2.3: The contours and the regions, A_k, of constant potential vorticity that they enclose.

which allows contours to break and join. This improves computational efficiency by keeping the number of nodes reasonable. For example, long, thin filaments of vorticity are a frequently observed feature in contour dynamics experiments. These naturally occurring filaments have to be described by many nodes but since they are so thin, they enclose only small areas and hence make little contribution to the surrounding flow. Contour surgery therefore allows truncation of the filaments in order to stop them stretching out and introducing more nodes and further allows them to be absorbed by nearby vorticity patches, hence dramatically reducing the total number of nodes in each step of the computation.

Part I of this thesis is organised as follows. Chapter 3 examines analytically the interaction between a single point vortex which may exist in either of the

two layers and its associated waves. In chapter 4 the nonlinear interaction of a point vortex and large amplitude waves is studied using contour dynamics. Chapters 5 and 6 study configurations of two vortices near large amplitude topography. In chapter 5 the particular case where the vortices are located in different layers and have different sign circulations (a heton) is discussed. In chapter 6 the case where the vortices exist in the same layer (a dipole) is investigated. Both lower- and upper-layer dipoles are considered. Applications of some of the above configurations are discussed and finally, conclusions are presented in chapter 7.

Chapter 3

The motion of a point vortex near large amplitude topography in a two-layer fluid

3.1 Introduction

A relatively simple model of a continental shelf is used to investigate the motion of a point vortex near large amplitude topography. In particular, large step-like topography with two-layer fluid on one side of the step and just one layer on the other side (figure 3.1(a)) is studied. The height of topography in the upper layer is small compared to the depth of the upper layer, enabling application of quasi-geostrophic theory (see chapter 2). Thompson [1993] uses a similar arrangement to study two-layer flow over a right circular cylinder. It is emphasised that, even though quasi-geostrophic theory is used, the topography is genuinely large in that it occupies a large fraction of the depth of the two-layer fluid. As will become evident, the dynamics of vortices and

topographic waves in this model is significantly different than that of more conventional (and less relevant to real ocean continental shelf regions) quasi-geostrophic models with topography occupying a small fraction of the depth of the lower layer only.

The aim of the present work is to study the interaction of steep topography with vortices in a two-layer fluid. In order to keep the model relatively simple and allow some analytical progress, following Stern and Flierl [1987], Bell [1990] and Dunn et al. [2001], point vortices near topography which is piecewise flat are studied. A particular aim is to contrast the behaviour of upper- and lower-layer vortices. Note that the use of point vortices is, in many cases, a good model for finite area vortices, see, for example, Johnson and McDonald [2004a,b].

In section 3.2 the structure of two-layer quasi-geostrophic point vortices in the absence of topography is briefly reviewed. In section 3.3 the general expressions for both upper- and lower-layer vortex streamfunctions in the presence of large amplitude step topography are derived. The dispersion relation of freely propagating topographic waves is derived in section 3.4. In section 3.5, the wave-lower-layer vortex interaction problem is studied, including an analytic solution for the limiting case of an infinitely deep lower layer. The case of an upper-layer vortex is considered in section 3.6.

3.2 Two-layer quasi-geostrophic vortices

Quasi-geostrophic dynamics of a two-layer fluid with rigid upper- and lower-layer boundaries implies the conservation of the potential vorticities q_1 and q_2 by fluid columns in the upper and lower layers respectively, where, in the

absence of topography,

$$q_1 = \nabla^2\psi_1 - \frac{1}{1+\delta}(\psi_1 - \psi_2), \tag{3.1}$$

and

$$q_2 = \nabla^2\psi_2 + \frac{\delta}{1+\delta}(\psi_1 - \psi_2), \tag{3.2}$$

where ψ_1 and ψ_2 are streamfunctions in the upper and lower layers respectively and $\delta = H_1/H_2$ is the ratio of the undisturbed upper-layer depth, H_1 to the undisturbed lower-layer depth, H_2 (see Pedlosky 1987 and the general theory outlined in chapter 2). Note, lengths are scaled by the baroclinic deformation radius, $L_D = (g'H_1H_2/(H_1+H_2))^{1/2}/f_0$, streamfunctions by $Rof_0L_D^2$ and time by $(Rof_0)^{-1}$, where $Ro = U/f_0L_D$ is the Rossby number (required to be small for quasi-geostrophic dynamics). Here U is a typical velocity, f_0 is the constant Coriolis parameter and g' is the reduced gravity.

Let

$$\psi_C = \psi_1 - \psi_2, \tag{3.3}$$

and

$$\psi_T = \frac{\delta}{1+\delta}\psi_1 + \frac{1}{1+\delta}\psi_2, \tag{3.4}$$

be the baroclinic and barotropic streamfunctions respectively. Note, the upper- and lower-layer streamfunctions can be recovered from ψ_T and ψ_C according to $\psi_1 = \psi_T + (1/(1+\delta))\psi_C$ and $\psi_2 = \psi_T - (\delta/(1+\delta))\psi_C$.

Following Hogg and Stommel [1985], point vortices can be represented by delta-functions in the potential vorticity. Here, unlike the two-layer hetons of Hogg and Stommel [1985], a point vortex exists in only one of the layers. Introducing a point vortex of strength s in the upper layer gives

$$\psi_1 = \frac{\delta}{1+\delta}\frac{s}{2\pi}\log r - \frac{1}{1+\delta}\frac{s}{2\pi}K_0(r), \tag{3.5}$$

and

$$\psi_2 = \frac{\delta}{1+\delta}\frac{s}{2\pi}\log r + \frac{\delta}{1+\delta}\frac{s}{2\pi}K_0(r), \tag{3.6}$$

where $r = |(x-x', y-y')|$ and (x', y') is the location of the vortex. The fluid velocities $\boldsymbol{u_1} = (u_1, v_1)$ and $\boldsymbol{u_2} = (u_2, v_2)$ in the upper and lower layers are given by $u_{1,2} = -\partial\psi_{1,2}/\partial y$ and $v_{1,2} = \partial\psi_{1,2}/\partial x$, i.e.

$$u_1 = -\frac{s}{2\pi}\frac{\delta}{1+\delta}\frac{y-y'}{(x-x')^2+(y-y')^2} - \frac{s}{2\pi}\frac{1}{1+\delta}\frac{(y-y')K_1\left(((x-x')^2+(y-y')^2)^{1/2}\right)}{((x-x')^2+(y-y')^2)^{1/2}}, \tag{3.7}$$

$$v_1 = \frac{s}{2\pi}\frac{\delta}{1+\delta}\frac{x-x'}{(x-x')^2+(y-y')^2} + \frac{s}{2\pi}\frac{1}{1+\delta}\frac{(x-x')K_1\left(((x-x')^2+(y-y')^2)^{1/2}\right)}{((x-x')^2+(y-y')^2)^{1/2}}, \tag{3.8}$$

$$u_2 = -\frac{s}{2\pi}\frac{\delta}{1+\delta}\frac{y-y'}{(x-x')^2+(y-y')^2} + \frac{s}{2\pi}\frac{\delta}{1+\delta}\frac{(y-y')K_1\left(((x-x')^2+(y-y')^2)^{1/2}\right)}{((x-x')^2+(y-y')^2)^{1/2}}, \tag{3.9}$$

$$v_2 = \frac{s}{2\pi}\frac{\delta}{1+\delta}\frac{x-x'}{(x-x')^2+(y-y')^2} - \frac{s}{2\pi}\frac{\delta}{1+\delta}\frac{(x-x')K_1\left(((x-x')^2+(y-y')^2)^{1/2}\right)}{((x-x')^2+(y-y')^2)^{1/2}}. \tag{3.10}$$

Alternatively, introducing a point vortex in the lower layer gives

$$\psi_1 = \frac{1}{1+\delta}\frac{s}{2\pi}\log r + \frac{1}{1+\delta}\frac{s}{2\pi}K_0(r), \tag{3.11}$$

and

$$\psi_2 = \frac{1}{1+\delta}\frac{s}{2\pi}\log r - \frac{\delta}{1+\delta}\frac{s}{2\pi}K_0(r). \tag{3.12}$$

So the fluid velocities in the upper and lower layers are

$$u_1 = -\frac{s}{2\pi}\frac{1}{1+\delta}\frac{y-y'}{(x-x')^2+(y-y')^2} + \frac{s}{2\pi}\frac{1}{1+\delta}\frac{(y-y')K_1\left(((x-x')^2+(y-y')^2)^{1/2}\right)}{((x-x')^2+(y-y')^2)^{1/2}}, \quad (3.13)$$

$$v_1 = \frac{s}{2\pi}\frac{1}{1+\delta}\frac{x-x'}{(x-x')^2+(y-y')^2} - \frac{s}{2\pi}\frac{1}{1+\delta}\frac{(x-x')K_1\left(((x-x')^2+(y-y')^2)^{1/2}\right)}{((x-x')^2+(y-y')^2)^{1/2}}, \quad (3.14)$$

$$u_2 = -\frac{s}{2\pi}\frac{1}{1+\delta}\frac{y-y'}{(x-x')^2+(y-y')^2} - \frac{s}{2\pi}\frac{\delta}{1+\delta}\frac{(y-y')K_1\left(((x-x')^2+(y-y')^2)^{1/2}\right)}{((x-x')^2+(y-y')^2)^{1/2}}, \quad (3.15)$$

$$v_2 = \frac{s}{2\pi}\frac{1}{1+\delta}\frac{x-x'}{(x-x')^2+(y-y')^2} + \frac{s}{2\pi}\frac{\delta}{1+\delta}\frac{(x-x')K_1\left(((x-x')^2+(y-y')^2)^{1/2}\right)}{((x-x')^2+(y-y')^2)^{1/2}}. \quad (3.16)$$

3.3 Bottom topography and general solution

Consider a two-layer fluid in which there is a step at $x = 0$ with shallow water for $x < 0$ and deep water for $x > 0$ (figure 3.1(a)). The shallow water, $x < 0$, is homogeneous, while the deep water for $x > 0$ comprises of a two-layer stratification.

When the fluid is at rest, the non-dimensional potential vorticity is $q = 1/h$, where h is the layer depth. Hence, the upper-layer potential vorticity, q_1

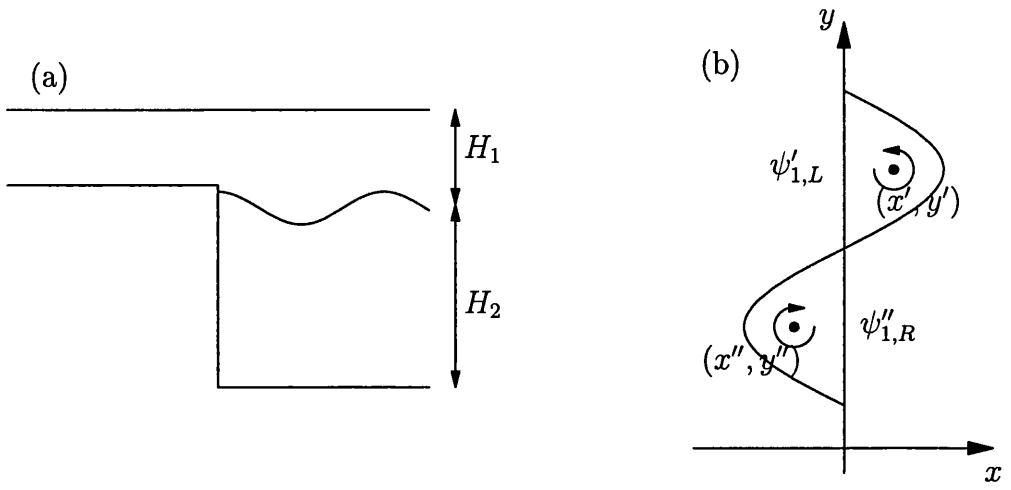

Figure 3.1: Bottom topography and free waves notation. (a) Side view, and (b) top view, showing displacement of the line of fluid particles in the upper layer which initially overlay the step $x = 0$.

is larger for $x < 0$ and smaller for $x > 0$. Therefore, the non-dimensional potential vorticity jump, s, across $x = 0$, can be defined by

$$s = q_1|_{x^-} - q_1|_{x^+} > 0. \tag{3.17}$$

Further, the topography is assumed to be such that on the right, the height of topography in the upper layer is a small fraction of overall depth, again see figure 3.1(a). This ensures that the demands of quasi-geostrophic theory are satisfied and therefore that (3.1) and (3.2) are valid for $x > 0$. Thompson [1993] considered a similar arrangement in which a large amplitude circular seamount penetrated only a small depth of the upper layer of a two-layer fluid, enabling quasi-geostrophic theory to be used in both layers.

Consider the effects of anomalous vorticity on either side of the step generated by a disturbance, $\eta(y, t)$, in the material line separating the two regions of constant potential vorticity in the upper layer which initially overlays $x = 0$. This is done, using the method of Green's functions, so that the anomalous

vorticity regions are taken to be delta-functions in the first instance.

The boundary conditions are

$$u_2 = 0 \text{ at } x = 0, \tag{3.18}$$

and

$$u_1, v_1 \text{ continuous at } x = 0. \tag{3.19}$$

First, consider a point vortex in the upper layer at (x', y') with $x' > 0$ (figure 3.1(b)). The vorticity of the vortex may be thought of as having arisen from a fluid column crossing from $x < 0$ to $x > 0$ and therefore, by potential vorticity conservation, has strength s. A velocity field with zero potential vorticity is then added so that the velocities at the step ($x = 0$) satisfy the boundary conditions, (3.18) and (3.19). The streamfunctions $\psi'_{1,R}$, in the upper layer for $x > 0$, $\psi'_{1,L}$, in the upper layer for $x < 0$ and $\psi'_{2,R}$, in the lower layer, due to a point vortex located at $x' > 0$ can then be deduced. (Note, the 'L' and 'R' subscripts stand for left- and right-hand side.)

Now consider a vortex at (x'', y'') with $x'' < 0$ (figure 3.1(b)). Again, the boundary conditions are satisfied by adding a zero potential vorticity field to the vortex generated velocities. This gives streamfunctions $\psi''_{1,R}$, in the upper layer for $x > 0$, $\psi''_{1,L}$, in the upper layer for $x < 0$ and $\psi''_{2,R}$, in the lower layer, due to a point vortex located at $x'' < 0$.

Note, in the above arguments and what follows, quantities with a single dash arise due to the presence of the point vortex at (x', y') with $x' > 0$, and all quantities with double dashes arise due to the influence of the vortex at (x'', y'') with $x'' < 0$.

The streamfunctions owing to the vortices and zero potential vorticity fields are combined to give the total streamfunctions in the upper layer due to a displacement, $\eta(y, t)$, of the contour which initially overlays the step. The Green's

function method is now used to obtain the response for a continuous distribution of vorticity associated with a wave-like disturbance shown in figure 3.1(b). For $x \geq 0$,

$$\begin{aligned}\psi_{1,R}(x,y,t) &= \int_{\eta>0}\int_{0}^{\eta(y',t)} \psi'_{1,R}(x,x',y-y')dx'dy' \\ &+ \int_{\eta<0}\int_{\eta(y'',t)}^{0} \psi''_{1,R}(x,x'',y-y'')dx''dy'', \end{aligned} \tag{3.20}$$

where the first integral is over y' values such that $\eta > 0$ and the second integral is over y'' values such that $\eta < 0$. Similarly, for $x \leq 0$

$$\begin{aligned}\psi_{1,L}(x,y,t) &= \int_{\eta>0}\int_{0}^{\eta(y',t)} \psi'_{1,L}(x,x',y-y')dx'dy' \\ &+ \int_{\eta<0}\int_{\eta(y'',t)}^{0} \psi''_{1,L}(x,x'',y-y'')dx''dy''. \end{aligned} \tag{3.21}$$

Further, the lower-layer streamfunction is given by,

$$\begin{aligned}\psi_{2,R}(x,y,t) &= \int_{\eta>0}\int_{0}^{\eta(y',t)} \psi'_{2,R}(x,x',y-y')dx'dy' \\ &+ \int_{\eta<0}\int_{\eta(y'',t)}^{0} \psi''_{2,R}(x,x'',y-y'')dx''dy''. \end{aligned} \tag{3.22}$$

Thus, the streamfunction due to an upper-layer disturbance of the potential vorticity contour initially overlaying the step is determined by (3.20), (3.21) and (3.22). The quantities $\psi'_{1,R}$, $\psi''_{1,R}$, $\psi'_{1,L}$, $\psi''_{1,L}$, $\psi'_{2,R}$ and $\psi''_{2,R}$ are now derived.

3.3.1 Calculation of zero potential vorticity fields

The zero potential vorticity equations for this system are,

$$\nabla^2\psi'_{T_{\text{zero}}} = 0, \tag{3.23}$$

and

$$\nabla^2\psi'_{C_{\text{zero}}} - \psi'_{C_{\text{zero}}} = 0, \tag{3.24}$$

for the two-layer fluid region, $x \geq 0$, and

$$\nabla^2 \psi'_{1,L_{\text{zero}}} = 0, \tag{3.25}$$

for the single-layer fluid region, $x \leq 0$. The zero potential vorticity equations are solved using Fourier transforms. Throughout, Fourier and inverse Fourier transforms are defined by,

$$F^*(k) = \int_{-\infty}^{\infty} F(y) e^{-iky} dy, \tag{3.26a}$$

and

$$F(y) = \frac{1}{2\pi} \int_{-\infty}^{\infty} F^*(k) e^{iky} dk. \tag{3.26b}$$

Hence the solution of (3.23) which remains bounded as $x \to \infty$ can be written,

$$\psi'_{T_{\text{zero}}}(x,y) = \frac{1}{2\pi} \int_{-\infty}^{\infty} A(k) e^{-|k|x+iky} dk. \tag{3.27}$$

Similarly the solution of (3.24) is,

$$\psi'_{C_{\text{zero}}}(x,y) = \frac{1}{2\pi} \int_{-\infty}^{\infty} B(k) e^{-x\left(k^2+1\right)^{1/2}+iky} dk, \tag{3.28}$$

where $A(k)$ and $B(k)$ are, for the moment, arbitrary functions. The solution of (3.25) which remains bounded as $x \to -\infty$ is

$$\psi'_{1,L_{\text{zero}}}(x,y) = \frac{1}{2\pi} \int_{-\infty}^{\infty} C(k) e^{|k|x+iky} dk, \tag{3.29}$$

where $C(k)$ is another arbitrary function to be found.

By differentiating (3.27), (3.28) and (3.29), writing the velocities at $x = 0$ due to a point vortex at $x' > 0$ in terms of its Fourier transform and substituting into the boundary conditions, three equations for the unknowns, A, B and C are found. These may be solved to give,

$$\begin{aligned} A(k) \;=\; & \frac{s\delta e^{-iky'}}{2(1+\delta)} \left(\frac{e^{-|k|x'}}{|k|} - \frac{e^{-x'\left(k^2+1\right)^{1/2}}}{\left(k^2+1\right)^{1/2}} - \frac{2\delta e^{-|k|x'}}{(2\delta+1)|k| + \left(k^2+1\right)^{1/2}} \right. \\ & \left. + \frac{e^{-x'\left(k^2+1\right)^{1/2}}}{\left(k^2+1\right)^{1/2}} \left(\frac{(2\delta+1)|k| - \left(k^2+1\right)^{1/2}}{(2\delta+1)|k| + \left(k^2+1\right)^{1/2}} \right) \right), \end{aligned} \tag{3.30}$$

$$B(k) = \frac{-s\delta e^{-iky'-|k|x'}}{(2\delta+1)|k|+(k^2+1)^{1/2}} + \frac{se^{-iky'-x'(k^2+1)^{1/2}}}{2(k^2+1)^{1/2}}\left(\frac{(2\delta+1)|k|-(k^2+1)^{1/2}}{(2\delta+1)|k|+(k^2+1)^{1/2}}\right), \quad (3.31)$$

$$C(k) = \frac{-se^{-iky'}}{(2\delta+1)|k|+(k^2+1)^{1/2}}\left(\delta e^{-|k|x'}+e^{-x'(k^2+1)^{1/2}}\right). \quad (3.32)$$

The upper-layer streamfunction for $x > 0$ due to a point vortex at $x' > 0$ is given by,

$$\psi'_{1,R}(x,y) = \psi'_{T_{\text{zero}}}(x,y) + \frac{1}{1+\delta}\psi'_{C_{\text{zero}}}(x,y) + \psi'_{1,V}(x,y), \quad (3.33)$$

where $\psi'_{1,V}$ is the streamfunction due to a point vortex in the upper layer at (x',y') (with $x' > 0$). $\psi'_{1,V}$ is calculated by transforming the fluid velocity in the upper layer, u_1 (or v_1), to Fourier space and back and integrating. Through the use of identities in Gradshteyn and Ryzhik [1994],

$$\psi'_{1,V}(x,y) = -\frac{s}{2\pi}\int_{-\infty}^{\infty}\frac{e^{ik(y-y')}}{1+\delta}\left(\frac{\delta e^{-|k||x-x'|)}}{2|k|}+\frac{e^{-|x-x'|(k^2+1)^{1/2}}}{2(k^2+1)^{1/2}}\right)dk. \quad (3.34)$$

Therefore substituting (3.27) and (3.28) (through use of (3.30) and (3.31)) into (3.33) gives an explicit form for $\psi'_{1,R}$ (not shown), the upper-layer streamfunction for $x > 0$ due to a point vortex at $x' > 0$. Similarly, using the fact that the streamfunction in $x < 0$ due to a point vortex at $x' > 0$ is given simply by,

$$\psi'_{1,L}(x,y) = \psi'_{1,L_{\text{zero}}}(x,y), \quad (3.35)$$

substituting (3.29) (through use of (3.32)) into (3.35), gives,

$$\psi'_{1,L}(x,x',y-y') = -\frac{s}{2\pi}\int_{-\infty}^{\infty}\frac{e^{ik(y-y')+|k|x}\left(\delta e^{-|k|x'}+e^{-x'(k^2+1)^{1/2}}\right)}{(2\delta+1)|k|+(k^2+1)^{1/2}}dk. \quad (3.36)$$

Furthermore, in the lower layer,

$$\psi'_{2,R}(x,y) = \psi'_{T_{\text{zero}}}(x,y) - \frac{\delta}{1+\delta}\psi'_{C_{\text{zero}}}(x,y) + \psi'_{2,V}(x,y), \quad (3.37)$$

where $\psi'_{2,V}$ is the lower-layer streamfunction due to a point vortex in the upper layer at (x', y') (with $x' > 0$), which in Fourier space is

$$\psi'_{2,V}(x,y) = \frac{s}{2\pi}\int_{-\infty}^{\infty} \frac{\delta e^{ik(y-y')}}{2(1+\delta)}\left(-\frac{e^{-|k||x-x'|}}{|k|} + \frac{e^{-|x-x'|\left(k^2+1\right)^{1/2}}}{\left(k^2+1\right)^{1/2}}\right) dk. \quad (3.38)$$

Again, substituting (3.27) and (3.28) into (3.37) gives an explicit form for the lower-layer streamfunction for $x > 0$ due to a point vortex at $x' > 0$.

Consider, now, the case in which the point vortex is located at (x'', y'') with $x'' < 0$. In the same way, the zero potential vorticity equations (3.23),(3.24) and (3.25) can again be solved giving,

$$\psi''_{T_{\text{zero}}}(x,y) = \frac{1}{2\pi}\int_{-\infty}^{\infty} D(k)e^{-|k|x+iky}dk, \quad (3.39)$$

$$\psi''_{C_{\text{zero}}}(x,y) = \frac{1}{2\pi}\int_{-\infty}^{\infty} E(k)e^{-x\left(k^2+1\right)^{1/2}+iky}dk, \quad (3.40)$$

for fluid with $x \geq 0$, and

$$\psi''_{1,L_{\text{zero}}}(x,y) = \frac{1}{2\pi}\int_{-\infty}^{\infty} F(k)e^{|k|x+iky}dk, \quad (3.41)$$

for fluid with $x \leq 0$. Here D, E and F are arbitrary functions. Satisfying all boundary conditions in a similar manner to the case for a vortex at (x', y'), $x' > 0$ gives three equations relating D, E and F with solution,

$$D(k) = \frac{s\delta e^{-iky''+|k|x''}}{(2\delta+1)|k| + \left(k^2+1\right)^{1/2}}, \quad (3.42)$$

$$E(k) = \frac{s(\delta+1)e^{-iky''+|k|x''}}{(2\delta+1)|k| + \left(k^2+1\right)^{1/2}}, \quad (3.43)$$

$$F(k) = \frac{se^{-iky''+|k|x''}}{2|k|}\left(\frac{|k| - \left(k^2+1\right)^{1/2}}{(2\delta+1)|k| + \left(k^2+1\right)^{1/2}}\right). \quad (3.44)$$

Thus the streamfunction in the upper layer for $x > 0$ due to a point vortex located at $x'' < 0$ is,

$$\psi''_{1,R}(x,y) = \psi''_{T_{\text{zero}}}(x,y) + \frac{1}{1+\delta}\psi''_{C_{\text{zero}}}(x,y), \quad (3.45)$$

and using (3.39), (3.40), (3.42) and (3.43) this can be written as,

$$\psi''_{1,R}(x,x'',y-y'') = \frac{s}{2\pi}\int_{-\infty}^{\infty} \frac{e^{ik(y-y'')+|k|x''}\left(\delta e^{-|k|x} + e^{-x\left(k^2+1\right)^{1/2}}\right)}{(2\delta+1)|k| + (k^2+1)^{1/2}} dk. \quad (3.46)$$

Similarly, the streamfunction for $x < 0$ due to a point vortex at $x'' < 0$ is

$$\psi''_{1,L}(x,y) = \psi''_{1,L_{\text{zero}}}(x,y) + \psi''_{1,V}(x,y), \quad (3.47)$$

where $\psi''_{1,V}$ is the (single-layer) streamfunction due to a point vortex at (x'',y'') (with $x'' < 0$), which in Fourier space is equivalent to

$$\psi''_{1,V}(x,y) = \frac{s}{2\pi}\int_{-\infty}^{\infty} \frac{e^{ik(y-y'')-|k||x-x''|}}{2|k|} dk. \quad (3.48)$$

Finally, in the lower layer,

$$\psi''_{2,R}(x,y) = \psi''_{T_{\text{zero}}}(x,y) - \frac{\delta}{1+\delta}\psi''_{C_{\text{zero}}}(x,y). \quad (3.49)$$

Hence (using (3.39) and (3.40)),

$$\psi''_{2,R}(x,x'',y-y'') = \frac{s}{2\pi}\int_{-\infty}^{\infty} \frac{\delta e^{ik(y-y'')+|k|x''}\left(e^{-|k|x} - e^{-x\left(k^2+1\right)^{1/2}}\right)}{(2\delta+1)|k| + (k^2+1)^{1/2}} dk. \quad (3.50)$$

Therefore, all the quantities in (3.20), (3.21) and (3.22) are known explicitly. From these expressions for the streamfunctions, the behaviour of vortices and associated topographic waves near the chosen topography can be described.

3.4 Linear topographic waves

An analytic expression for the topographic wave dispersion relation can now be derived. The topography shown in figure 3.1(a) supports topographic waves owing to the jump in potential vorticity across the step. Let the waves have

amplitude given by $\eta(y,t)$ and linearise (3.33) for small amplitude disturbances (i.e. $x' \to 0$) about $x = 0$ giving,

$$\psi'_{1,R}(x,0,y-y') = -\frac{s}{2\pi}\int_{-\infty}^{\infty} \frac{e^{ik(y-y')}\left(\delta e^{-|k|x} + e^{-x\left(k^2+1\right)^{1/2}}\right)}{\left((2\delta+1)|k| + (k^2+1)^{1/2}\right)}dk. \quad (3.51)$$

Now, letting $x'' \to 0$ in (3.46) and making the dummy variable substitution $y' = y''$ in (3.51) gives,

$$\psi'_{1,R}(x,0,y-y'') = -\psi''_{1,R}(x,0,y-y''). \quad (3.52)$$

With $x' = x'' = 0$, (3.20) becomes

$$\begin{aligned}\psi_{1,R}(x,y,t) &= \int_{\eta>0} \eta(y'',t)\psi'_{1,R}(x,0,y-y'')dy'' \\ &\quad - \int_{\eta<0} \eta(y'',t)\psi''_{1,R}(x,0,y-y'')dy''. \end{aligned} \quad (3.53)$$

Substitution of (3.52) into (3.53) and using (3.46), yields

$$\psi_{1,R}(x,y,t) = -\frac{s}{2\pi}\int_{-\infty}^{\infty}\int_{-\infty}^{\infty} \frac{\eta(y'',t)e^{ik(y-y'')}\left(\delta e^{-|k|x} + e^{-x\left(k^2+1\right)^{1/2}}\right)}{(2\delta+1)|k| + (k^2+1)^{1/2}}dkdy''. \quad (3.54)$$

Similarly

$$\psi_{1,L}(x,y,t) = -\frac{s}{2\pi}\int_{-\infty}^{\infty}\int_{-\infty}^{\infty} \frac{\eta(y'',t)e^{ik(y-y'')+|k|x}}{(2\delta+1)|k| + (k^2+1)^{1/2}}(\delta+1)\,dkdy''. \quad (3.55)$$

For completeness, and for use in section 3.5, the lower-layer streamfunction is, under the linear assumption,

$$\psi_{2,R}(x,y,t) = -\frac{s}{2\pi}\int_{-\infty}^{\infty}\int_{-\infty}^{\infty} \frac{\eta(y'',t)\delta e^{ik(y-y'')}\left(e^{-|k|x} - e^{-x\left(k^2+1\right)^{1/2}}\right)}{(2\delta+1)|k| + (k^2+1)^{1/2}}dkdy''. \quad (3.56)$$

A linear plane wave with small amplitude, ε, wavenumber α and frequency $\omega(\alpha)$ has the form

$$\eta = \varepsilon e^{i(\alpha y - \omega(\alpha)t)}, \quad (3.57)$$

and satisfies

$$\frac{\partial \eta}{\partial t} = u_1 \text{ on } x = 0. \tag{3.58}$$

The Fourier transform of (3.58) gives

$$\frac{\partial \eta^*}{\partial t} = u_1^* = \left(-\frac{\partial \psi_1(0,y,t)}{\partial y}\right)^* = -ik\psi_1^*(0,k,t), \tag{3.59}$$

using the properties of the Fourier transform. From (3.54) (or (3.55)),

$$\begin{aligned} \psi_1^*(0,k,t) &= \frac{-s(\delta+1)}{(2\delta+1)+(k^2+1)^{1/2}} \int_{-\infty}^{\infty} \eta(y'',t) e^{-iky''} dy'' \\ &= \frac{-s(\delta+1)\eta^*(k)}{(2\delta+1)+(k^2+1)^{1/2}}. \end{aligned} \tag{3.60}$$

In Fourier space the plane wave has the form

$$\eta^* = \varepsilon e^{-i\omega(k)t}, \tag{3.61}$$

and hence (3.59) and (3.60) finally give the dispersion relation

$$\omega(k) = -\frac{ks(\delta+1)}{(2\delta+1)|k|+(k^2+1)^{1/2}}, \tag{3.62}$$

where k is the wavenumber.

The phase and group velocities (figure 3.2) of these waves are

$$c_p = \frac{\omega}{k} = -\frac{s(\delta+1)}{(2\delta+1)|k|+(k^2+1)^{1/2}}, \tag{3.63}$$

and

$$c_g = \frac{\partial \omega}{\partial k} = -\frac{s(\delta+1)}{(k^2+1)^{1/2}\left((2\delta+1)|k|+(k^2+1)^{1/2}\right)^2}. \tag{3.64}$$

From (3.63), since $s > 0$, the waves travel in the negative y-direction (in the Northern hemisphere), i.e. with shallow water (high potential vorticity) to their right, as is typical of vorticity waves.

In the limit $\delta \to 0$, the dispersion relation (3.62) takes the form,

$$\omega(k) = -\frac{ks}{|k|+(k^2+1)^{1/2}}. \tag{3.65}$$

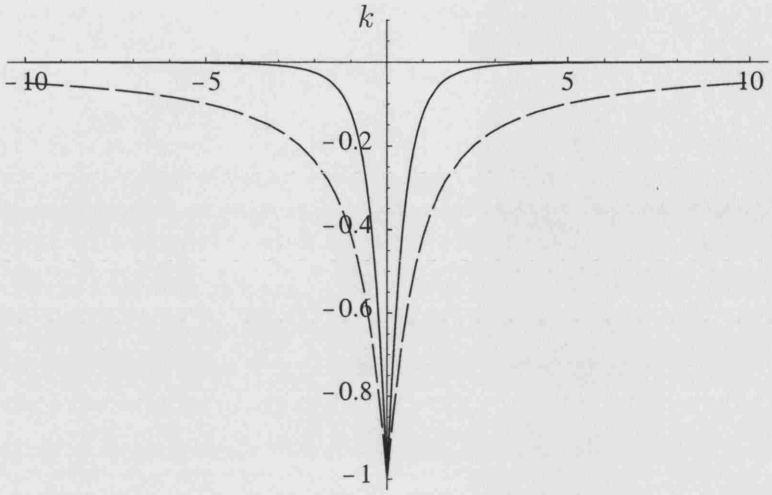

Figure 3.2: Phase speed (dashed) and group speed (solid) for topographic waves with $s = 1$ and $\delta = 0$.

This limit corresponds to an infinitely deep lower layer and, to the author's knowledge, has no analog in the literature. In this case, in section 3.5, the properties of topographic waves generated by moving vortices are examined analytically. On the other hand, the limit $\delta \to \infty$ (vanishing lower-layer depth) corresponds to a one-layer barotropic fluid with a step change in depth, and (3.62) becomes

$$\omega(k) = -\frac{s}{2}\operatorname{sgn} k, \tag{3.66}$$

which is, as expected, the same as the dispersion relation derived by Bell [1990] who studied barotropic waves existing on a piecewise constant potential vorticity distribution. Further, in the limit $k \to \infty$, the dispersion relation (3.62) also takes the form of (3.66). Physically, this implies that very short waves do not 'feel' the lower layer. Finally, observe (figure 3.2) that it is possible for $c_p = c_g$. In this case $k \to 0$ and $\omega \to -ks(\delta + 1)$, i.e. very long waves are non-dispersive. This, as will be shown later, has implications for the behaviour of vortices near such topography. For example, in a system

forced by, say, a vortex moving at the long wave phase speed, energy will not be able to escape the system and the contour displacement will grow without bound leading to a breakdown in linear theory. This scenario is investigated in section 3.5.

3.5 Linear initial value lower-layer vortex problem

This section considers the initial value problem of a lower-layer vortex being 'switched on' at time $t = 0$ in the vicinity of the step topography (figure 3.3). The vortex is able to propagate parallel to the wall relatively quickly due to its 'image'[1] and topographic waves may be generated. This is in contrast to the case of a vortex in the upper layer (Dunn et al. 2001) which propagates only slowly (since there is no image effect owing to a wall). This problem is of particular interest because there is some evidence (e.g. Hamilton 1992) for the existence of intense deep-sea vortices that propagate near sharply varying topography such as continental shelf regions (see also Armi and D'Asaro 1980). Such deep vortices may give rise to significant on-shelf currents owing to excitation of topographic waves (see chapter 7).

The lower-layer vortex is initially centred on the point $(x', y') = (L, 0)$, $L > 0$, and has circulation Γ. Note that the parameters s and the magnitude Γ are not independent (see Dunn et al. 2001) since the quasi-geostrophic potential vorticities (3.1) and (3.2) have been non-dimensionalised by the Rossby

[1]This is not an image in the conventional sense of a vortex with equal and opposite circulation located on the other side of the step. Rather, owing to the particular geometry here, it is more of a partial image effect. However, in the limit $\delta \to 0$, the image effect tends to the conventional equal and opposite case.

number, Ro, which effectively measures the magnitude of Γ. However, in this work Γ is retained as its sign is important and also because, in some cases, it is convenient to treat s as fixed and vary Γ.

The nonlinear interaction of vortices and waves will be studied in chapter 4; however, some progress can be made assuming linear dynamics, $|\eta(y,t)| \ll 1$ (i.e. a weak vortex inducing only small disturbances at the step $x = 0$).

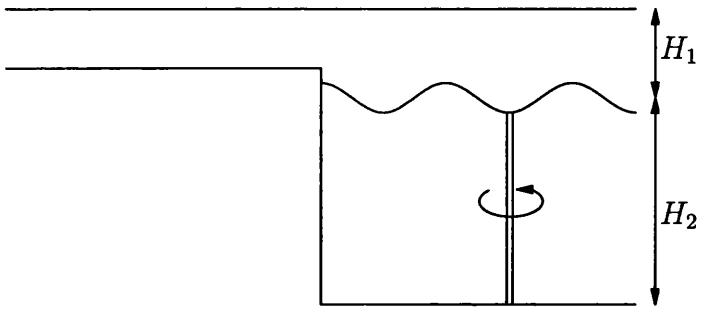

Figure 3.3: Initial value vortex problem. A lower-layer vortex forcing is shown.

The velocity field in the x-direction in the upper layer can be split into two parts:

$$u_1 = u_{1,v} + u_{1,S}, \tag{3.67}$$

where $u_{1,v}$ is the fluid velocity generated by the vortex at $(L, 0)$, and $u_{1,S}$ is the self-induced velocity of the type discussed in section 3.3, owing to potential vorticity conservation as upper-layer fluid is forced across the change in depth at $x = 0$ by the vortex.

The vortex-induced velocity at the step is calculated using

$$u_{1,v}(0,y) = -\frac{\partial \psi'_{1,L_{\text{zero}}}(0,y)}{\partial y}, \tag{3.68}$$

and, for a lower-layer vortex, it can be shown using (3.11) and (3.12) that

$$u_{1,v}(0,y) = -\frac{i\Gamma}{2\pi}\int_{-\infty}^{\infty} \frac{ke^{iky}}{(2\delta+1)|k| + (k^2+1)^{1/2}} \left(e^{-L\left(k^2+1\right)^{1/2}} - e^{-|k|L}\right) dk. \tag{3.69}$$

By differentiating (3.54), the self-induced velocity, $u_{1,S}$, in the limit of small amplitude contour displacements can be deduced:

$$u_{1,S}(0,y,t) = \frac{is}{2\pi}\int_{-\infty}^{\infty}\int_{-\infty}^{\infty} \frac{\eta(y',t)ke^{ik(y-y')}}{(2\delta+1)|k| + (k^2+1)^{1/2}} (\delta+1)\, dkdy', \tag{3.70}$$

which, in terms of the dispersion relation, (3.62), can be written

$$u_{1,S}(0,y,t) = -\frac{i}{2\pi}\int_{-\infty}^{\infty} \eta^*(k,t)\omega(k)e^{iky}dk. \tag{3.71}$$

Thus, taking the transforms of (3.69) and (3.71) and substituting into the Fourier transform of (3.67) gives,

$$u_1^*(0,k,t) = -i\Gamma k\left(\frac{e^{-L\left(k^2+1\right)^{1/2}} - e^{-|k|L}}{(2\delta+1)|k| + (k^2+1)^{1/2}}\right) + is\eta^*(k,t)\frac{k(\delta+1)}{(2\delta+1)|k| + (k^2+1)^{1/2}}. \tag{3.72}$$

Finally, the linearised kinematic condition in a frame moving with the vortex is used,

$$\frac{\partial\eta}{\partial t} + U\frac{\partial\eta}{\partial y} = u_1 \qquad \text{on} \qquad x = 0, \tag{3.73}$$

where $V = -U$ is the vortex speed in the y-direction due to its image. Under the linear assumption the wave effects on the vortex leading to a velocity in the y-direction are required to be small compared to the along escarpment velocity, V. This is demonstrated explicitly later. Taking the Fourier transform, the kinematic condition becomes, using (3.62) and (3.72),

$$\frac{\partial\eta^*}{\partial t} + i\eta^*\left(-kV + \omega\right) = ik\phi(k), \tag{3.74}$$

where

$$\phi(k) = -\Gamma \left(\frac{e^{-L\left(k^2+1\right)^{1/2}} - e^{-|k|L}}{(2\delta+1)|k| + (k^2+1)^{1/2}} \right). \tag{3.75}$$

The propagation speed, V, of a lower-layer vortex centred on $(L, 0)$ with $L > 0$ is given by

$$V = \frac{\partial}{\partial x} \left(\psi'_{T_{\text{zero}}} - \frac{\delta}{1+\delta} \psi'_{C_{\text{zero}}} \right) \Bigg|_{(L,0)}, \tag{3.76}$$

where $\psi'_{T_{\text{zero}}}$ and $\psi'_{C_{\text{zero}}}$ are given by (3.27) and (3.28). This gives

$$\begin{aligned} V = & \frac{\Gamma}{2\pi} \int_{-\infty}^{\infty} -\frac{e^{-2|k|L}}{2(1+\delta)} + \frac{\delta e^{-|k|L} \left(|k| e^{-|k|L} - (k^2+1)^{1/2} e^{-L\left(k^2+1\right)^{1/2}} \right)}{(1+\delta)\left((2\delta+1)|k| + (k^2+1)^{1/2} \right)} \\ & + \frac{e^{-L\left(k^2+1\right)^{1/2}}}{(1+\delta)\,(k^2+1)^{1/2}} \left(-\frac{\delta |k| e^{-|k|L}}{2} + \left(\frac{(2\delta+1)|k| - (k^2+1)^{1/2}}{(2\delta+1)|k| + (k^2+1)^{1/2}} \right) \right. \\ & \left. \times \left(\frac{\delta |k| e^{-|k|L}}{2} - \frac{\delta\,(k^2+1)^{1/2} e^{-L\left(k^2+1\right)^{1/2}}}{2} \right) \right) dk. \end{aligned} \tag{3.77}$$

The propagation speed for varying δ obtained by numerical computation of (3.77) (figure 3.4) is bounded when $L > 0$. As expected the magnitude of the propagation speed decreases as the ratio of the layer depths increases. This is because as δ increases, the relative height of the lower layer, H_2, decreases and therefore the driving vortex is smaller, and hence the image effect is weaker. In the limit $\delta \to 0$, (3.77) becomes

$$V = -\frac{\Gamma}{4\pi L}. \tag{3.78}$$

As expected (3.78) is as if there is an image vortex behind a wall extending through the entire depth of a single-layer fluid since $\delta \to 0$ corresponds to a single-layer rigid-lid barotropic fluid. Also in the limit $\delta \to \infty$, from (3.77),

$$V \to -\frac{\Gamma}{4\pi} \int_{-\infty}^{\infty} e^{-2L\left(k^2+1\right)^{1/2}} dk = -\frac{\Gamma}{2\pi} K_1(2L). \tag{3.79}$$

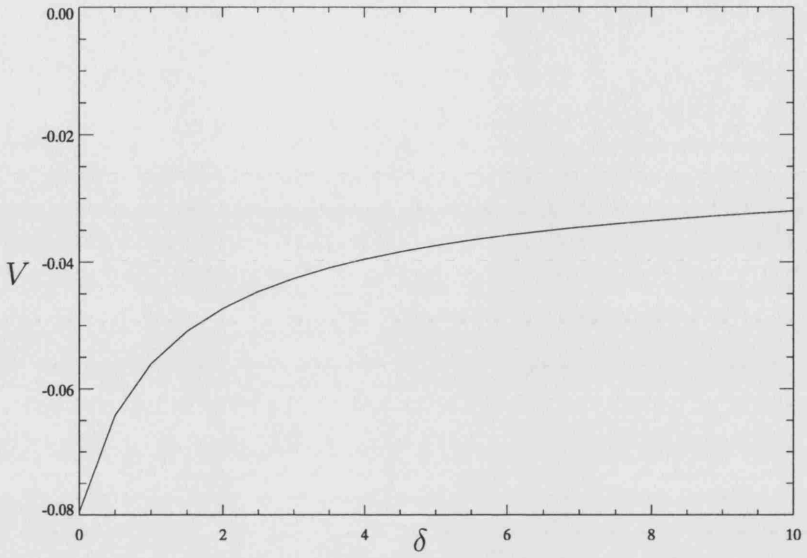

Figure 3.4: Propagation speed for increasing δ ($\Gamma = 1$ and $L = 1$).

Note that this is the speed of a one-and-a-half-layer vortex located a distance L from a wall. Therefore, the translational velocity is bounded by that of the equivalent vortex in a one-layer rigid-lid barotropic fluid and the vortex in a one-and-a-half-layer fluid, i.e. $-\Gamma/4\pi L \leq V \leq -\Gamma K_1(2L)/2\pi$. Since $\operatorname{sgn} V = -\operatorname{sgn} \Gamma$, anticyclones propagate in the positive y-direction and cyclones propagate in the negative y-direction.

3.5.1 Large time behaviour of $\eta(y,t)$

The solution of (3.74), subject to $\eta(y,0) = 0$, is

$$\eta^*(k,t) = \left(\frac{\phi}{-V + \omega k^{-1}}\right)\left(1 - e^{-ik(-V+\omega k^{-1})t}\right). \tag{3.80}$$

As $t \to \infty$, solutions to (3.74) reach the steady state,

$$\eta^*(k) = \frac{\phi(k)}{-V + \omega k^{-1}}, \tag{3.81}$$

provided that the radiation condition that no upstream waves exist is satisfied. If $V = \omega/k$, (3.81) has poles in the complex plane that correspond, in physical

space, to steady downstream waves. Note that ω/k is bounded, i.e. $-s(\delta+1) \leq c_p = \omega/k < 0$ (see figure 3.2 and (3.63)). Therefore the poles only exist for values of the vortex propagation speed in the range, $-s(\delta+1) \leq V < 0$; that is, the vortex propagation speed must be negative (and thus, the vortex must be a cyclone), but not too large, for poles and therefore waves to exist.

When $\Gamma < 0$ the vortex propagates in the positive y-direction, hence there is no wave-like term and only a localised steady response. Likewise, if $V < -s(\delta+1)$, the vortex propagation speed is greater than the phase velocity of topographic waves and poles do not exist and, again, there is only a localised steady response. Note that the radiating solutions are quasi-steady in that the wave drag will induce a drift velocity perpendicular to the step (Dunn et al. 2001). This drift is within the assumptions of linear theory, however, small compared to V. Likewise, the displacement η will induce a velocity parallel to the step, but again this is small compared to V in the linear limit (see section 3.5.3).

3.5.2 Evolution of $\eta(y,t)$

To find the response, $\eta(y,t)$, for arbitrary time, (3.80) is inverted for η^* numerically using the Fast Fourier Transform (FFT) algorithm. All plots shown in this section are moving in a frame with the lower-layer vortex and in each case (unless otherwise stated) the potential vorticity jump across the step is $s = 1$.

A typical evolution of $\eta(y,t)$ for a cyclone is shown in figure 3.5. The vortex initially causes an antisymmetric displacement of the contour which begins to disperse owing to topographic wave radiation. Transient waves are radiated ahead of the vortex, i.e. for negative values of y. As time increases from $t = 100$

to $t = 1000$ the steady downstream wave train ($y > 0$) develops.

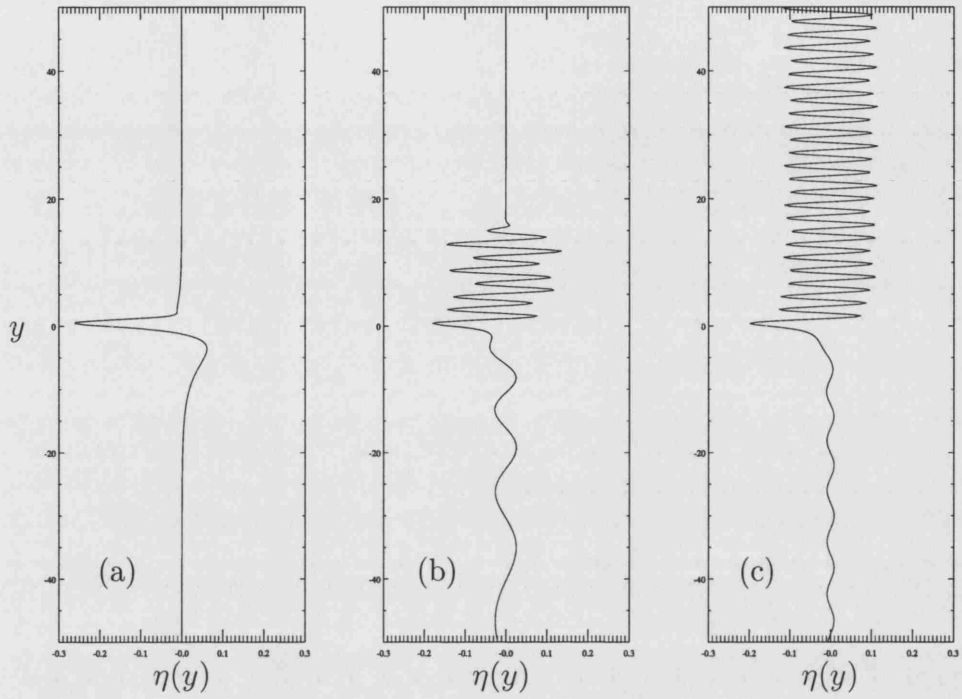

Figure 3.5: FFT evaluation of $\eta(y)$ over $x = 0$ with $\Gamma = 1$, $\delta = 0$ and $L = 0.5$. The varied parameter is time, t evaluated at (a) $t = 10$, (b) $t = 100$ and (c) $t = 1000$.

Figure 3.6 shows how the large-time displacement, $\eta(y)$, depends on the strength of the vortex circulation, Γ, for the case $\delta = 0$. As predicted there is no wake for an anticyclone, $\Gamma = -1$. For $\Gamma > 0$, topographic wave generation is possible and the wake amplitude and wavelength increase with circulation strength for $0 < \Gamma \leq 4\pi L$. In figure 3.6(e), the circulation strength is large enough so that $V < -s(\delta + 1)$ and no downstream wake occurs. Varying the wall-vortex distance, L, has the same effect as varying Γ: the effective strength of the vortex felt at the step is larger for smaller L, and hence wake amplitude and wavelength increase.

The wave amplitude decreases as δ increases (figure 3.7). This can be ex-

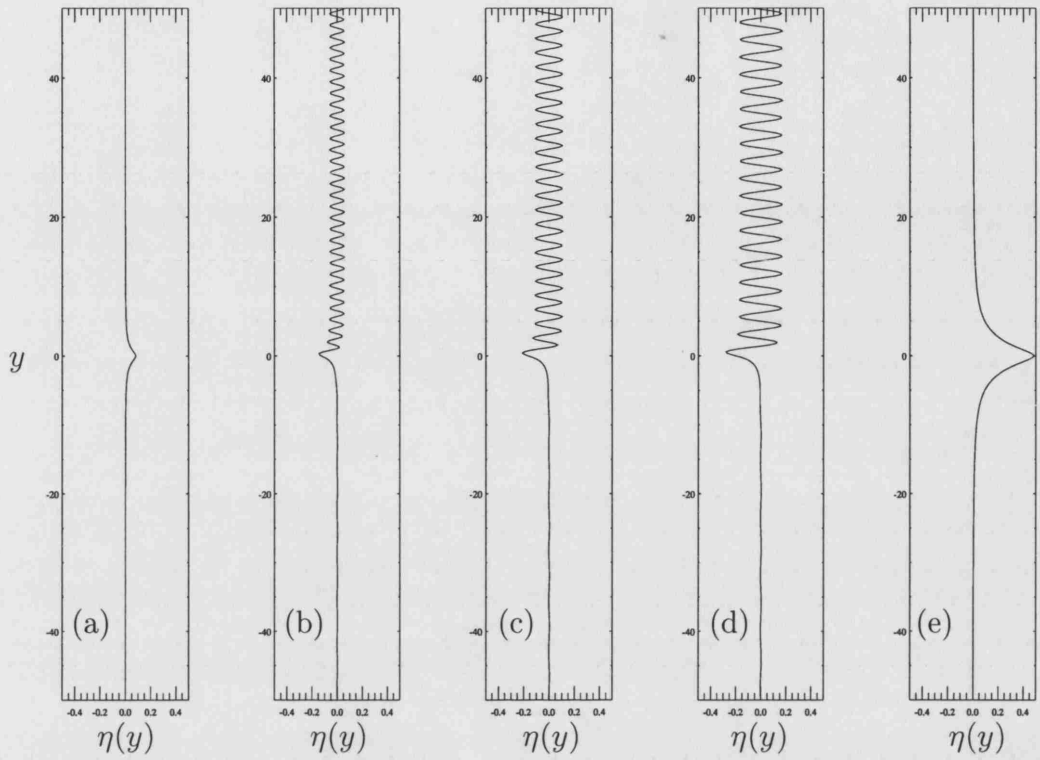

Figure 3.6: FFT evaluation of $\eta(y)$ over $x = 0$ with $t = 15\,000$, $\delta = 0$ and $L = 0.5$. The varied parameter is the circulation (a) $\Gamma = -1.0$, (b) $\Gamma = 0.8$, (c) $\Gamma = 1.0$, (d) $\Gamma = 1.2$ and (e) $\Gamma = 20.0$.

plained through figure 3.8 which shows how the resonant wavenumber, k_{res} (for which $V = \omega(k_{res})/k_{res}$), of the topographic waves varies with the propagation speed. At $V = -s(\delta + 1)$, the resonant wavenumber, k_{res}, vanishes and as $|V| \to 0$, k_{res} increases, i.e. large propagation speeds produce long waves. It is known (from figure 3.4) that, as δ increases the propagation speed, $|V|$, decreases, hence k_{res} increases. The forcing term, $\phi(k_{res})$, (from (3.75)) decays exponentially with k_{res}; therefore $\phi(k_{res})$ is smaller for larger values of δ, resulting in a reduced amplitude. Thus, the faster the vortex speed (up to $|V| = s(\delta + 1)$), the bigger the amplitude of the wake.

Figure 3.9 demonstrates that the steady response may grow without bound.

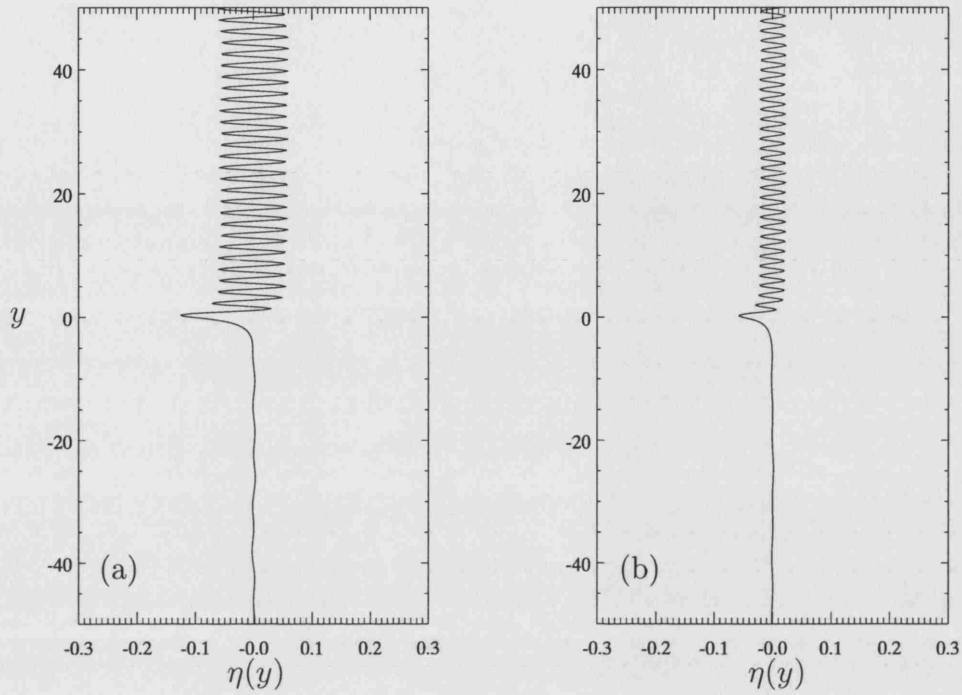

Figure 3.7: FFT evaluation of $\eta(y)$ over $x = 0$ with $t = 15\,000$, $\Gamma = 1.0$ and $L = 0.5$. The varied parameter is the ratio of layer depths, (a) $\delta = 0.5$ and (b) $\delta = 2.0$.

This resonance occurs when the phase and group velocities are equal, and for the particular case, $\delta = 0$, this requires $V = -s$, (this may be achieved, for example, by choosing $s = 1$, $\Gamma = \pi$ and $L = 0.25$, from (3.78)). To obtain figure 3.9, the parameter s is varied and the parameters Γ and L kept constant to show that the increasing response is due to resonance and not vortex characteristics. In figure 3.9(a), $s = 0.9$, and the propagation speed, V, is out of the range for which topographic waves exist, hence only the localised disturbance which doesn't grow with time is seen. In figure 3.9(c), $s = 1.1$, and V is now in the range for which topographic waves exist. The topographic waves downstream of the vortex can be observed. These tend to the steady wake. The localised disturbance has in fact decreased with time here. But

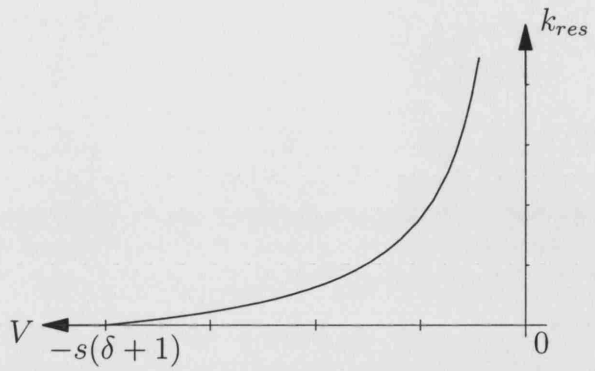

Figure 3.8: Variation of resonant wavenumber with propagation speed.

in figure 3.9(b), where $s = 1$ and $c_p = c_g$, the steady response has grown significantly with time. The response will continue to grow in time (typically with algebraic growth in t; e.g. Dunn et al. 2001) and ultimately linear theory becomes invalid.

3.5.3 The vortex back-reaction

Velocities owing to the displacement of η must, in turn, affect the vortex. This is similar to the positive feedback mechanism that occurs between deep eddies and meanders in Gulf Stream jets as described by Sutyrin et al. [2001]. Here the self induced (i.e. due to the topographic waves) velocities, $u_{2,S}, v_{2,S}$ at the vortex are calculated directly. Through the method of section 3.3,

$$u^*_{2,S} = \frac{iks\eta^*\delta\left(e^{-|k|L} - e^{-L\left(k^2+1\right)^{1/2}}\right)}{(2\delta+1)|k| + \left(k^2+1\right)^{1/2}}, \tag{3.82}$$

and

$$v^*_{2,S} = \frac{s\eta^*\delta\left(|k|e^{-|k|L} - \left(k^2+1\right)^{1/2} e^{-L\left(k^2+1\right)^{1/2}}\right)}{(2\delta+1)|k| + \left(k^2+1\right)^{1/2}}. \tag{3.83}$$

When $\delta = 0$ these self-induced velocities are zero, i.e. there is no vortex back-reaction. In this case, the lower layer is infinitely deep, thus the vortex is huge

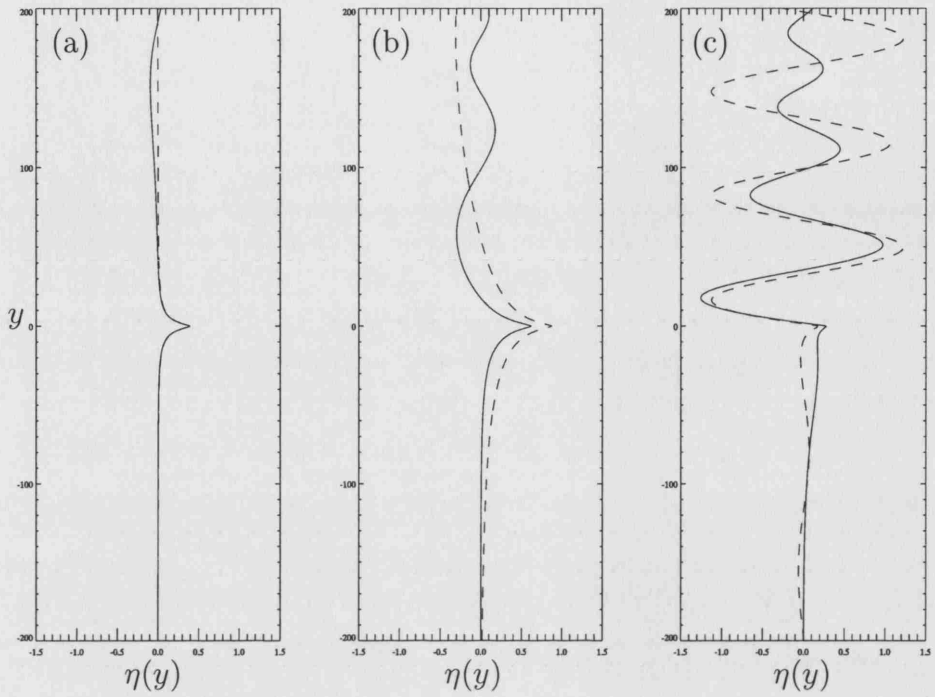

Figure 3.9: The steady response can grow without bound when $V = -1$, as shown at times $t = 1000$ (solid line) and $t = 10\,000$ (dashed line). Parameter values are (a) $s = 0.9$, (b) $s = 1$ and (c) $s = 1.1$.

and will respond infinitely slowly since the lower-layer velocities are vanishingly small in this limit. For non-zero depth ratio, (3.82) and (3.83) may be inverted numerically. Figure 3.10 shows the ratio of the magnitude of the back-reaction velocities $\left(u_{2,S}^2 + v_{2,S}^2\right)^{1/2}$ to the propagation speed for a range of depth ratios, δ. The ratio is always small, i.e. the propagation speed is at least a factor of 10 larger than the back-reaction velocity, and the back-reaction velocity approaches zero as $\delta \to 0$ or $\delta \to \infty$. However, the back-reaction velocity in the x-direction, $u_{2,S}$, may be significant since, though small, it is small compared to zero, leading to a slow drift in the x-direction. This is investigated in chapter 4. The 'noise' in figure 3.10 is a numerical artefact and can be made arbitrarily small by refining the numerical parameters of the Fourier transform

inversion procedure.

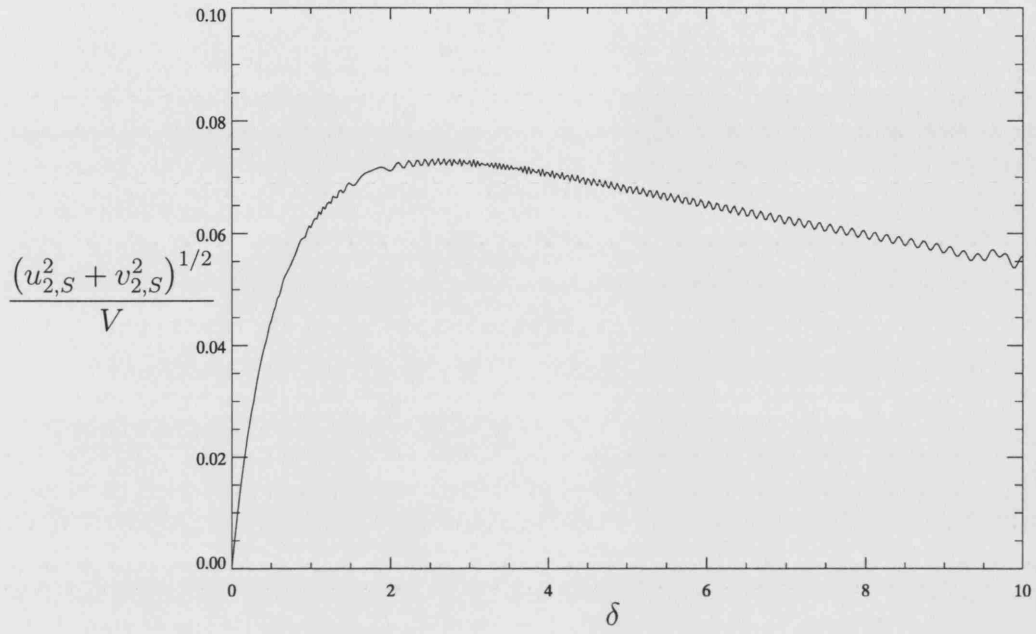

Figure 3.10: The ratio of the vortex back-reaction to the vortex propagation speed for a range of depth ratios. Parameters used are $\Gamma = 1$, $L = 0.5$ and $t = 10\,000$.

3.6 Linear initial value upper-layer vortex problem

For completeness, the problem of an upper-layer vortex being 'switched on' at time $t = 0$ is studied. The vortex is initially centred at $(x_0, 0)$, where the vortex may be situated on either side of the step and, indeed, may cross the step.

The solution of (3.74) for η^* is (3.80) where it can be shown that the forcing

term, $\phi(k)$, is given by

$$\phi(k) = \begin{cases} \Gamma\left(\dfrac{e^{-x_0\left(k^2+1\right)^{1/2}} + \delta e^{-|k|x_0}}{(2\delta+1)|k| + (k^2+1)^{1/2}}\right) & \text{for } x_0 > 0, \\ -\Gamma\left(\dfrac{e^{|k|x_0}(\delta+1)}{(2\delta+1)|k| + (k^2+1)^{1/2}}\right) & \text{for } x_0 \leq 0, \end{cases} \tag{3.84}$$

and the upper-layer vortex translational velocity is

$$V = \begin{cases} \dfrac{\Gamma}{2\pi}\displaystyle\int_{-\infty}^{\infty} -\frac{e^{-2|k|x_0}}{2(1+\delta)} \\ \quad + \dfrac{e^{-|k|x_0}\left(\delta|k|e^{-|k|x_0} + (k^2+1)^{1/2}e^{-x_0\left(k^2+1\right)^{1/2}}\right)}{(1+\delta)\left((2\delta+1)|k| + (k^2+1)^{1/2}\right)} \\ \quad + \dfrac{e^{-x_0\left(k^2+1\right)^{1/2}}}{(1+\delta)\left(k^2+1\right)^{1/2}}\left(-\dfrac{\delta|k|e^{-|k|x_0}}{2}\right. \\ \quad + \left(\dfrac{(2\delta+1)|k| - (k^2+1)^{1/2}}{(2\delta+1)|k| + (k^2+1)^{1/2}}\right) \\ \quad \times \left.\left(\dfrac{\delta|k|e^{-|k|x_0}}{2} + \dfrac{(k^2+1)^{1/2}e^{-x_0\left(k^2+1\right)^{1/2}}}{2}\right)\right) dk & \text{for } x_0 > 0, \\ \dfrac{\Gamma}{2\pi}\displaystyle\int_{-\infty}^{\infty} \frac{e^{2|k|x_0}}{2}\left(\dfrac{|k| - (k^2+1)^{1/2}}{(2\delta+1)\,|k| + (k^2+1)^{1/2}}\right) dk & \text{for } x_0 \leq 0. \end{cases} \tag{3.85}$$

Note $\phi(k)$ depends on $\operatorname{sgn}(x_0)$ since the vortex-induced velocity in the upper layer is dependent on which side of the step the vortex is located. Similarly, the translational velocity, V, is also dependent on $\operatorname{sgn}(x_0)$. For $x_0 > 0$, (3.84) and (3.85) only vary from the lower-layer driving vortex case by factors of δ and $\pm$ signs.

3.6.1 Evolution of $\eta(y,t)$

The evolution of $\eta(y,t)$ is found numerically by inverting (3.80). The results are similar to the lower-layer vortex case in that varying parameters such as

the vortex circulation, Γ or the wall-vortex distance, L, has qualitatively the same effect on the the displacement, $\eta(y)$. Obviously, changing the depth ratio, δ, has the opposite effect.

There are, however, some differences between the upper- and lower-layer vortex cases. First, an upper-layer vortex cannot self-propagate due to an image like the lower-layer vortex can. Therefore the propagation speeds are much lower and topographic waves take much longer to appear (compare evaluation times from figure 3.11 and figure 3.5). Second, since the propagation speeds

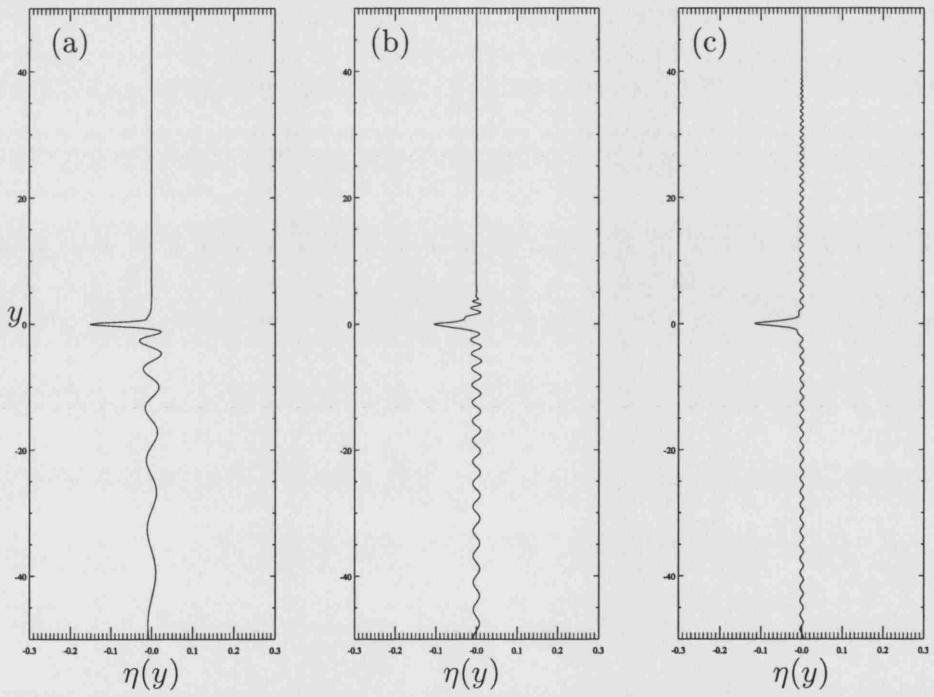

Figure 3.11: FFT evaluation of $\eta(y)$ over $x = 0$ with $\Gamma = 0.2$, $\delta = 0.2$ (realistic oceanic value) and $L = 0.5$. The varied parameter is time, t, evaluated at (a) $t = 100$, (b) $t = 1000$ and (c) $t = 10\,000$.

are much smaller for upper-layer vortices, the resonant wavenumber of the topographic waves, k_{res}, will be larger (figure 3.8) and hence the forcing term, (3.84), will be smaller. Therefore, upper-layer vortices produce significantly

smaller waves than lower-layer vortices in the linear regime.

On the other hand, wave-vortex interaction is potentially much more significant for upper-layer vortices since both the vortex and wave displacement are in the same layer and because there is no rapid drift of the vortex parallel to the step. In the nonlinear limit, it is possible for the vortex to 'wrap up' the contour $\eta(y,t)$, as it does in the single-layer problem studied by Dunn et al. [2001]. Since the back-reaction on the vortex is more significant, especially in the x-direction (depending on the sign of the vortex circulation), it is possible for the vortex to drift across the step causing a highly nonlinear response. This is studied using the method of contour dynamics in the next chapter.

3.7 Discussion

This chapter considers the motion of point vortices in a two-layer fluid near large amplitude topography. The topography is such that it separates regions comprising of one layer and two layers respectively and is such that quasi-geostrophy applies everywhere. The dispersion relation for the free topographic waves of this system, which propagate with shallow water to their right, is obtained analytically.

Analytical results were obtained for point vortices in either layer in the linear limit of small amplitude topographic waves. Lower-layer vortices move due to the influence of an image in the topography with cyclones and anticyclones propagating in opposite directions predominantly parallel to the topography. Analytical predictions also revealed that, for cyclones only, steady topographic wave wakes are possible.

Vortices in the lower layer are largely unaffected by the back-reaction resulting from potential vorticity disturbances across the topography. This is

due to their relatively large velocity parallel to the step meaning they rapidly propagate away from any such disturbances. On the other hand, upper-layer vortices, owing to their small translational velocities, may be significantly advected in the direction perpendicular to the step. In problems involving single fluid layers this frequently causes nonlinear behaviour, (i.e. large amplitude deformation of the vorticity contour overlaying the step) see McDonald [1998b], Dunn et al. [2001] and Stern and Flierl [1987]. This is investigated for the present model using a modified contour dynamics algorithm in the following chapter.

Chapter 4

Nonlinear evolution: contour dynamics

4.1 Introduction

The step topography considered in the previous chapter makes the method of contour dynamics particularly suitable for numerical solution since the upper-layer potential vorticity distribution is piecewise constant. The general theory behind the contour dynamics algorithm is outlined in chapter 2. The contour initially lies along $x = 0$, that is, along the step. A vortex is 'switched on' at time $t = 0$, and the contour evolves according to potential vorticity conservation. The algorithm used is a modified version of that used by Dunn et al. [2001], which in turn is an adaptation of the contour surgery algorithm developed by Dritschel [1988] allowing contours to break and join. The refinement made by Dunn et al. [2001] was to represent the topography as an infinitely long step. The contour dynamics algorithm integrates the full nonlinear quasi-geostrophic potential vorticity equations, namely conservation of the

upper- and lower-layer potential vorticities q_1 and q_2 given by (3.1) and (3.2) by resolving into barotropic and baroclinic modes, and is valid for arbitrary deformations of the initial contour.

In applying contour dynamics to the present problem special consideration needs to be given to the boundary conditions at $x = 0$ owing to the presence of step topography. In particular it is required to ensure that there is no velocity in the x-direction in the lower-layer at $x = 0$ and velocities in the x- and y-directions in the upper-layer at $x = 0$ are continuous (boundary conditions (3.18) and (3.19) respectively). Hence it is necessary to compute the zero potential vorticity fields required to satisfy these boundary conditions from the velocity jumps at $x = 0$ owing to the arbitrary distributions of non-zero vorticity either side of the step, equations (3.27)–(3.29) and (3.39)–(3.41). A similar procedure was used by Thompson [1993] for computing nonlinear two-layer flow past a seamount.

A schematic of the adapted contour dynamics algorithm is shown in figure 4.1, where a typical section of the contour in the region of the topography at $x = 0$ (dashed) is viewed from above. Panels 4.1(a)–(e) represent the main stages in the contour dynamics algorithm. The algorithm comprises of two parts since two fluid layers occupy the region $x > 0$ and just one for $x < 0$.

As remarked on in section 2, note that the contour and the step bound regions of non-zero potential vorticity. The contour dynamics algorithm effectively integrates over these areas by integrating around the boundary of the regions. Thus it is necessary to integrate along the contour and the step.

At each time step the contour is partitioned into n nodes having locations (x_i, y_i), $i = 1, \ldots, n$. First, to compute the contribution to the velocity field of the non-zero potential vorticity anomalies for $x < 0$ (i.e. on the single-layer

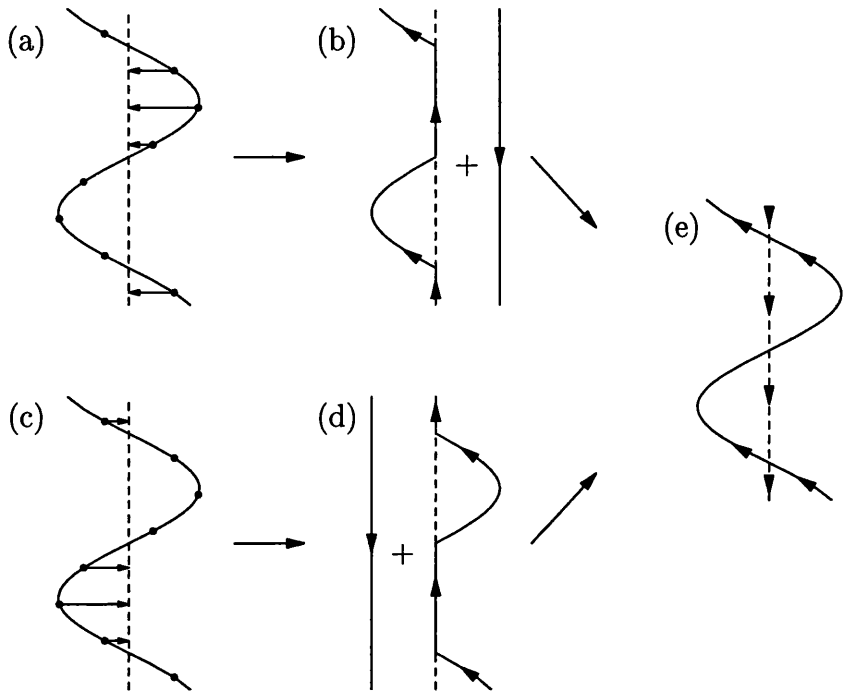

Figure 4.1: Schematic of the contour dynamics algorithm (viewed from above). The dashed line represents the topography at $x = 0$. The solid curves are the displaced contour along which integrations are performed (the directions of which are indicated by the arrows) by partitioning into the nodes $(x_i, y_i), i = 1, \ldots, n$ represented by the dots.

side), any nodes for which $x_i > 0$ are projected back on to the line $x = 0$ (figure 4.1(a)). This technique is employed since only nodes for which $x_i < 0$ give rise to velocities in the region $x < 0$ therefore the projection ensures no spurious velocities from nodes with $x_i > 0$ will be included. (Similarly only nodes for which $x_i > 0$ give rise to velocities in $x > 0$, figure 4.1(c).). Integrations are performed in order to find the barotropic velocity at all nodes due to the i^{th} node, $i = 1, \ldots, n$ (figure 4.1(b)). The contribution to the velocity along $x = 0$ due to the i^{th} node is also calculated (for use later when satisfying the boundary conditions). Further, the velocities due to the i^{th} node at

any vortex centres, (x_0, y_0), are calculated. The topography is also partitioned into a (constant) number of nodes and velocities due to the topography at the (x_i, y_i), $i = 1, \ldots, n$, along the line $x = 0$ and at any vortices are calculated (This integration and its direction are represented by the vertical line in figure 4.1(b)). Thus velocities in $x < 0$ due to contour deformations which occupy the region $x < 0$ have been found. That is, the sum of the projected contour integration and the integration along the topography gives the contribution to the velocity field due to vorticity anomalies located on the $x < 0$ side.

The same process is conducted for the region $x > 0$, i.e. any nodes for which $x_i < 0$ are projected back on to the line $x = 0$ and similar integrations performed (figures 4.1(c) and (d)). However, this time since there are two layers for $x > 0$, an integration to calculate baroclinic velocities is also conducted, i.e. both barotropic and baroclinic velocities are computed according to their appropriate Green's functions.

The resulting velocities (due to the nodes on the contour and the topography) are combined (figure 4.1(e)) according to

$$\boldsymbol{u_1} = \boldsymbol{u_T} + \frac{1}{1+\delta}\boldsymbol{u_C}, \tag{4.1}$$

and

$$\boldsymbol{u_2} = \boldsymbol{u_T} - \frac{\delta}{1+\delta}\boldsymbol{u_C}. \tag{4.2}$$

This gives the total velocity at each node of the upper-layer contour and any vortices (which can only be located in the upper-layer for $x_0 < 0$ but may be located in either layer for $x_0 > 0$). However, these velocities will not in general satisfy the boundary conditions (3.18) and (3.19) and thus the zero potential vorticity fields from the velocity jumps at $x = 0$ must be added, equations (3.27)–(3.29) and (3.39)–(3.41).

The zero potential vorticity fields are calculated in Fourier space through the use of equations (3.30)–(3.32) and (3.42)–(3.44). These are then transformed to real space and added to the velocities $\boldsymbol{u_1}$ and $\boldsymbol{u_2}$ accordingly.

The algorithm has been rigourously tested. Among many others, tests included simulating the motion of a single-layer vortex near a wall, which gave velocities in accordance with analytical theory. Further, the motion of upper-layer vortices and associated contour deformations and vortex trajectories in the limit of a vanishingly small lower-layer ($\delta \rightarrow \infty$) were compared to the equivalent one-and-a-half-layer results of Dunn et al. [2001]. Finally, the effects of decreasing the spatial resolution of the nodes was tested, producing identical results.

The length of time over which the numerical runs are conducted is restricted by the fact that the infinite step and contour must be represented with finite lengths. Waves traveling away from the vortex centre will ultimately produce end effects which may adversely influence the evolution. For strong vortices, $|\Gamma| = 1$, (and a wall of length 200), runs up to $t = 100$ are possible before they become inaccurate. For weaker vortices and therefore smaller displacements, longer runs are possible. Throughout this work, all contour dynamics experiments are conducted using a time step of $\Delta t = 0.1$ and a spatial resolution parameter of $\mu = 0.15$ (Dritschel 1988). Note that to produce the results in this and subsequent chapters, without loss of generality, the parameter $s = 1$ unless otherwise stated.

In what follows, numerical results for lower-layer vortices (both cyclones and anticyclones) and then upper-layer vortices are described.

4.2 Lower-layer anticyclones

The evolution of the contour for a lower-layer anticyclone with $\delta = 0$, $\Gamma = -1$ and initial position $(x_0, y_0) = (0.5, 25)$ is shown in figure 4.2. The vortex causes an initial disturbance in the contour, and the transient waves resulting from this initial disturbance are seen to propagate in the negative y-direction and decay as time increases. However, the initial disturbance remains localised near the vortex, both of which propagate in the positive y-direction for all time. As explained in section 3.5 there are no steady topographic waves for anticyclonic vortices. Qualitative and quantitative comparison with figure 3.6(a) indicates excellent agreement with the linear theory, since lower-layer vortices propagate quickly and, therefore, cannot induce nonlinear behaviour.

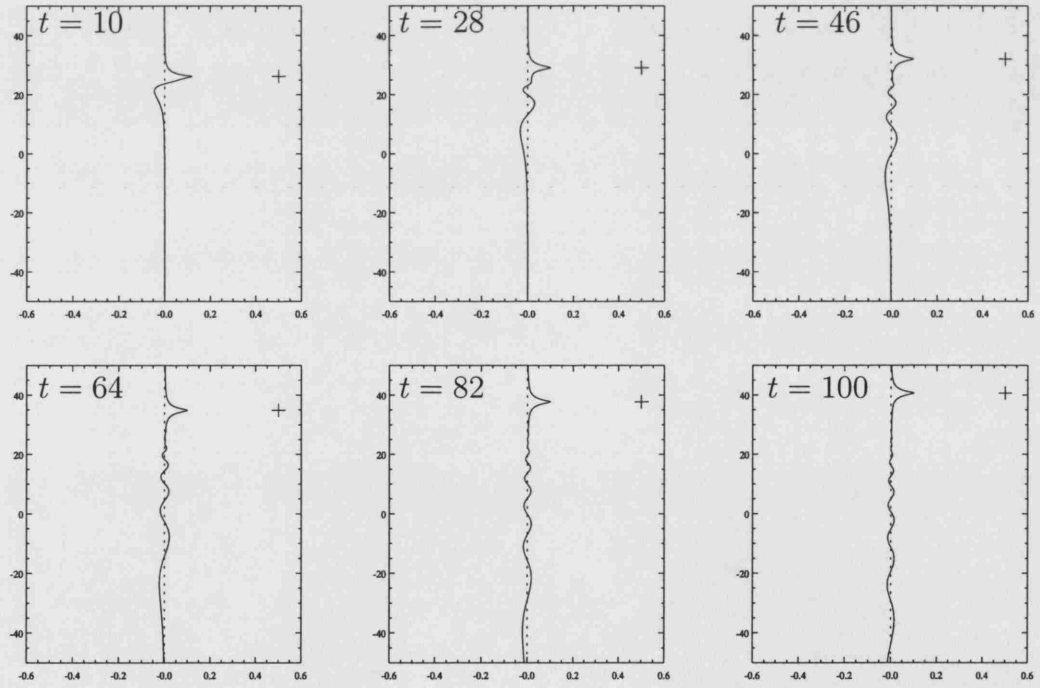

Figure 4.2: Evolution of the contour for a lower-layer anticyclone indicated by the cross. The parameter values used are $\delta = 0$, $\Gamma = -1$ and $(x_0, y_0) = (0.5, 25)$. The position of the step is indicated by the dashed line.

Vortex paths are shown (figure 4.3) for different values of δ, with $\Gamma = -1$ fixed. These are similar to the paths described by Beismann et al. [1999] in their large ridge experiments. Anticyclonic vortices are advected by their image in the positive y-direction as predicted. Consistent with linear theory, there is no back-reaction in the $\delta = 0$ case and the path is exactly as would be obtained using (3.78). For non-zero δ there is a small deviation in the x-direction which is due to the effect of the transient waves. As δ increases the vortex propagation speed in the y-direction decreases, and so the vortex spends more time in the vicinity of any transient waves which advect the vortex towards positive x. As the vortex propagates away from the influence of the transient waves, the trajectory approaches a straight line parallel to the step. Note, given the different scales on the axes, that the dominant motion is parallel to the step.

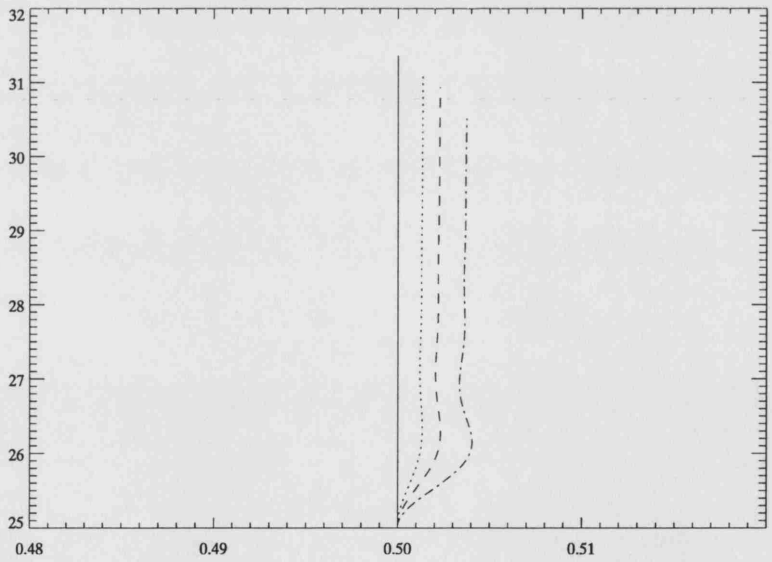

Figure 4.3: Lower-layer anticyclonic vortex trajectories for $0 < t < 40$. The parameter values used are $\Gamma = -1$, $(x_0, y_0) = (0.5, 25)$, $\delta = 0$ (solid line), $\delta = 0.1$ (dotted line), $\delta = 0.2$ (dashed line) and $\delta = 0.5$ (dot-dashed line).

4.3 Lower-layer cyclones

The evolution of the contour for a lower-layer cyclone with $\delta = 0$, $\Gamma = 1$ and initial position $(x_0, y_0) = (0.5, 25)$ is shown in figure 4.4. A lower-layer cyclonic vortex causes an initial disturbance to the contour of opposite sign to that caused by an anticyclonic vortex. As with anticyclonic vortices, the initial disturbance remains localised near the vortex throughout the evolution. Figure 4.4 shows a steady wave train developing, which is well described by linear theory (cf. figures 3.5(a) and 3.5(b)). This is because a lower-layer vortex has a large propagation speed and will propagate away from disturbances quickly, hence, any nonlinear behaviour is small.

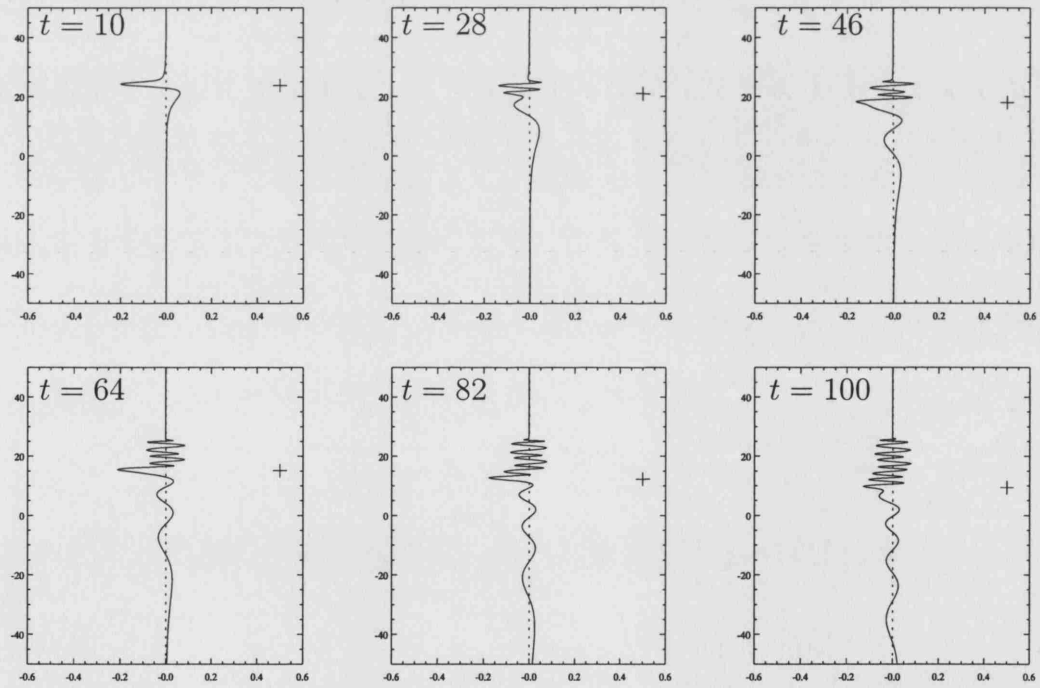

Figure 4.4: Evolution of the contour for a lower-layer cyclone indicated by the cross. The parameter values used are $\delta = 0$, $\Gamma = 1$ and $(x_0, y_0) = (0.5, 25)$. The position of the step is indicated by the dashed line.

Again, vortex paths are shown (figure 4.5) for different values of δ, with $\Gamma = 1$ fixed. Like anticyclonic vortices, there is no back-reaction in the $\delta = 0$ case and the displacement of the vortex is exactly modeled by linear theory. As δ increases the vortex propagation speed decreases and so the vortex spends more time in the vicinity of any transient waves. Thus, the transient waves further advect the vortex for small times causing the oscillatory trajectories. Also the generation of topographic waves will affect the vortex path according to the back reaction velocities, (3.82) and (3.83).

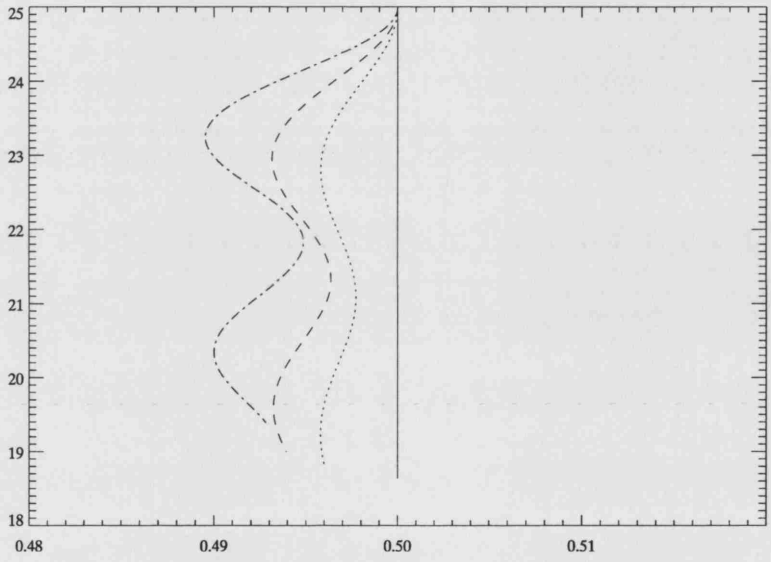

Figure 4.5: Lower-layer cyclonic vortex trajectories for $0 < t < 40$. The parameter values used are $\Gamma = 1$, $(x_0, y_0) = (0.5, 25)$, $\delta = 0$ (solid line), $\delta = 0.1$ (dotted line), $\delta = 0.2$ (dashed line) and $\delta = 0.5$ (dot-dashed line).

4.4 Upper-layer vortices

The evolution of the contour for an upper-layer anticyclone is shown in figure 4.6, where $\delta = 0.2$. The parameter values used are such that direct com-

parison with the lower-layer experiments is possible, i.e. the anticyclone has the same strength, $\Gamma = -1$, and starts the same distance from the topography, $(x_0, y_0) = (0.5, 0)$. Therefore, any differences in behaviour are due to the fact that the vortex is located in the upper rather than the lower layer. The response of the contour is much larger than for a vortex in the lower layer since upper-layer vortices have smaller propagation speeds and therefore remain in the vicinity of the displaced contour and are able to 'wrap up' the contour. The back-reaction of the contour on the vortex is also much more pronounced and the vortex and contour interact in a highly nonlinear way. The contour is wrapped around the vortex and eventually part of the contour is pinched off. This forms a dipole and the vortex and separated contour will drift away from the topography. Similar dipole formation was observed in the numerical experiments of Wang [1992] and Dunn et al. [2001] and the laboratory experiments of Zavala Sansón et al. [1999].

The evolution of the contour for an upper-layer cyclone is shown in figure 4.7, where again $\delta = 0.2$. As for the upper-layer anticyclone, parameter values are chosen such that comparison with the lower-layer case is possible ($\Gamma = 1$ and $(x_0, y_0) = (0.5, 0)$). The vortex wraps the contour causing the vortex to drift across the step. Again, the evolution is similar to the single-layer experiments of Wang [1992] and Dunn et al. [2001]. Note that upper-layer cyclones are able to pass over the step whereas anticyclones are not. The anticyclone drifts away from the step due to the formation of a dipole with fluid 'torn' from the shallow side of the step. In the cyclonic case, fluid dragged from the shallow region to the deep region has vorticity of the same sign as the vortex. Therefore, rather than forming a dipole which reflects the vortex, the cyclonic structure further advects the vortex across the step. Zavala Sansón

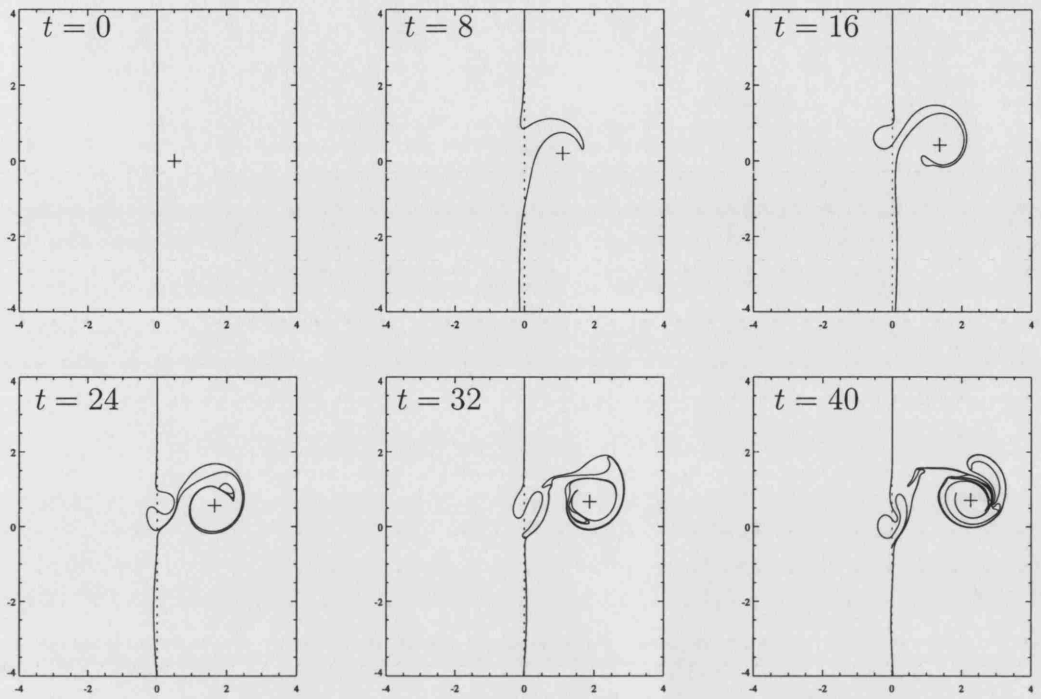

Figure 4.6: Evolution of the contour for an upper-layer anticyclone indicated by the cross. The parameter values used are $\delta = 0.2$ (realistic oceanic value), $\Gamma = -1$ and $(x_0, y_0) = (0.5, 0)$. The position of the step is indicated by the dashed line.

et al. [1999] and Zavala Sansón and van Heijst [2000] describe similar behaviour in their single-layer experiments where the topographic effects outweigh the β-effect.

Experiments for different intensities, Γ, have also been conducted (not shown) and the contour evolution is similar to that shown in figures 4.6 and 4.7 with a general trend of larger displacements and a correspondingly faster vortex drift for stronger vortices. Weaker cyclonic/anticyclonic vortices drift comparatively slowly toward/away from the topography, i.e. the topography has a greater effect, inhibiting transport across the escarpment (cf. Zavala Sansón 2002).

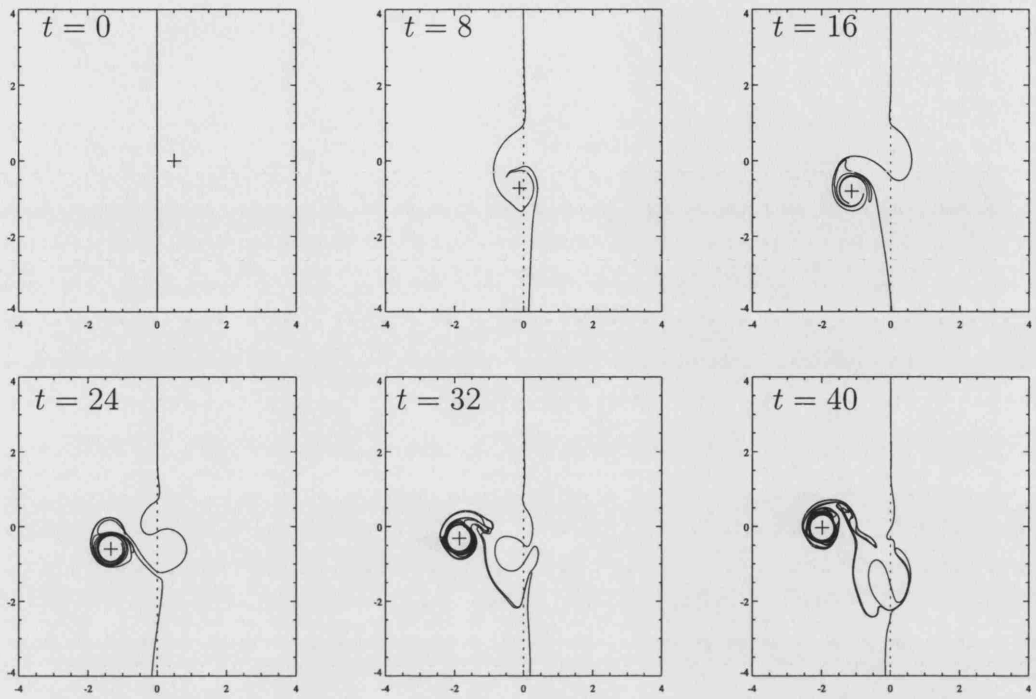

Figure 4.7: Evolution of the contour for an upper-layer cyclone indicated by the cross. The parameter values used are $\delta = 0.2$ (realistic oceanic value), $\Gamma = 1$ and $(x_0, y_0) = (0.5, 0)$. The position of the step is indicated by the dashed line.

4.5 Discussion

This chapter complements the analytic work done in chapter 3 by investigating the nonlinear parameter space using a modified contour dynamics algorithm.

Importantly, the lower-layer vortex contour dynamics results agree well with the linear theory, indicating that linear theory is robust and holds over a large region of parameter space. This is because lower-layer vortices have a larger propagation speed than upper-layer vortices and will propagate away from any contour deflections quickly. They are therefore unable to induce nonlinearity. Furthermore, lower-layer vortices and upper-layer contour deflections

are located in different layers and therefore their associated velocities have a reduced influence on each other. Conversely, vortices in the upper layer readily exhibit nonlinear behaviour and contour dynamics predict that cyclones propagate towards and may cross the step whereas anticyclones propagate away from the step due to dipole formation. Hence lower-layer vortices produce relatively little on-shelf motion whereas upper-layer vortices can drive much stronger currents which may have significant oceanographic implications such as, for example, mixing on-shelf and off-shelf waters.

The use of quasi-geostrophic theory does have some limitations. For example, in contrast to the upper-layer anticyclone case examined here, dipole formation and subsequent drift away from the topography does not occur if the topography is small in the quasi-geostrophic sense and is wholly contained in the lower layer enabling an anticyclone to pass over the step in the presence of the β-effect as in Sutyrin et al. [2003]. Also, for large topography wholly contained in the lower layer (which cannot be studied using quasi-geostrophic theory), intense topographic wave radiation may disperse lower-layer circulations. The effects of such radiation depends on the size of the vortex (Thierry and Morel 1999). Further, for large amplitude topography contained in the lower layer, baroclinic dipoles may form (Herbette et al. 2003) which influence the evolution of the vortex.

Chapter 5

The motion of a heton near large amplitude topography in a two-layer fluid

5.1 Introduction

Hogg and Stommel [1985] studied a particular type of baroclinic vortex pair which they called a heton. A heton is a two-layer, quasi-geostrophic vortex configuration in which the vortices are of opposite sign and in different layers (figure 5.1(a)). It is well known that two vortices of opposite sign and equal strength, in the same layer (called a dipole, see chapter 6) advect each other along parallel paths. Similarly, a heton is self-propagating. The vortex in the lower layer induces a velocity on the vortex in the upper layer, while the vortex in the upper layer induces a velocity on the lower-layer vortex (figure 5.1(b)).

The induced velocities will be in the same direction (perpendicular to the line joining the vortex centres) and have a magnitude dependent on the ratio

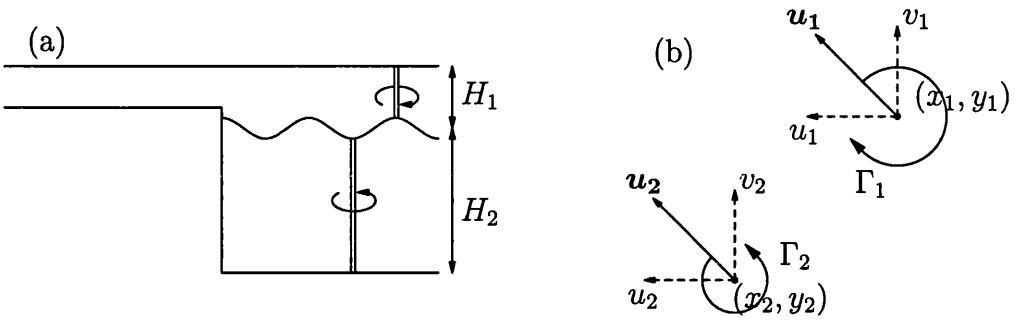

Figure 5.1: A heton (near topography). (a) Side view. (b) Top view.

of the layer depths, δ, the relative sizes of the vortex circulations, Γ_1 and Γ_2, and the distance between the vortices or the separation, d, where

$$d = \sqrt{(x_1 - x_2)^2 + (y_1 - y_2)^2}, \tag{5.1}$$

and (x_1, y_1) and (x_2, y_2) are the positions of the upper- and lower-layer vortices respectively. In the absence of topography, the self-propagation velocities in the x- and y-directions of the lower- and upper-layer vortex components of the heton, (u_2, v_2) and (u_1, v_1) (figure 5.1(b)), are given by equations (3.9) and (3.10), and (3.13) and (3.14) where $(x, y) = (x_2, y_2)$, $(x', y') = (x_1, y_1)$, $s = \Gamma_1$ and $(x, y) = (x_1, y_1)$, $(x', y') = (x_2, y_2)$, $s = \Gamma_2$ respectively, i.e.

$$u_2 = -\frac{\Gamma_1}{2\pi}\frac{\delta}{1+\delta}\frac{y_2 - y_1}{(x_2 - x_1)^2 + (y_2 - y_1)^2} + \frac{\Gamma_1}{2\pi}\frac{\delta}{1+\delta}\frac{(y_2 - y_1)\, K_1\left(\left((x_2 - x_1)^2 + (y_2 - y_1)^2\right)^{1/2}\right)}{\left((x_2 - x_1)^2 + (y_2 - y_1)^2\right)^{1/2}}, \tag{5.2}$$

$$v_2 = \frac{\Gamma_1}{2\pi}\frac{\delta}{1+\delta}\frac{x_2 - x_1}{(x_2 - x_1)^2 + (y_2 - y_1)^2} - \frac{\Gamma_1}{2\pi}\frac{\delta}{1+\delta}\frac{(x_2 - x_1)\, K_1\left(\left((x_2 - x_1)^2 + (y_2 - y_1)^2\right)^{1/2}\right)}{\left((x_2 - x_1)^2 + (y_2 - y_1)^2\right)^{1/2}}, \tag{5.3}$$

and

$$u_1 = -\frac{\Gamma_2}{2\pi}\frac{1}{1+\delta}\frac{y_1 - y_2}{(x_1 - x_2)^2 + (y_1 - y_2)^2} + \frac{\Gamma_2}{2\pi}\frac{1}{1+\delta}\frac{(y_1 - y_2)\, K_1\left(\left((x_1 - x_2)^2 + (y_1 - y_2)^2\right)^{1/2}\right)}{\left((x_1 - x_2)^2 + (y_1 - y_2)^2\right)^{1/2}}, \quad (5.4)$$

$$v_1 = \frac{\Gamma_2}{2\pi}\frac{1}{1+\delta}\frac{x_1 - x_2}{(x_1 - x_2)^2 + (y_1 - y_2)^2} - \frac{\Gamma_2}{2\pi}\frac{1}{1+\delta}\frac{(x_1 - x_2)\, K_1\left(\left((x_1 - x_2)^2 + (y_1 - y_2)^2\right)^{1/2}\right)}{\left((x_1 - x_2)^2 + (y_1 - y_2)^2\right)^{1/2}}. \quad (5.5)$$

Equivalently, the magnitudes of the propagation velocities, $\boldsymbol{u_2}$ and $\boldsymbol{u_1}$, of each vortex component are given by

$$|\boldsymbol{u_2}| = \frac{\Gamma_1}{2\pi}\frac{\delta}{1+\delta}\left(\frac{1}{d} - K_1(d)\right), \quad (5.6)$$

and

$$|\boldsymbol{u_1}| = \frac{\Gamma_2}{2\pi}\frac{1}{1+\delta}\left(\frac{1}{d} - K_1(d)\right). \quad (5.7)$$

Note that, in general $|\boldsymbol{u_1}| \neq |\boldsymbol{u_2}|$ and the hetons follow a curved path as demonstrated by Hogg and Stommel [1985]. However, it is possible for $|\boldsymbol{u}| \equiv |\boldsymbol{u_1}| = |\boldsymbol{u_2}|$ and hence the heton to travel in a straight line. In this case, the ratio of the layer depths and the heton circulations are related, i.e. equating (5.2) and (5.4) gives

$$\Gamma_2 = -\delta\Gamma_1. \quad (5.8)$$

Figure 5.2 shows how the magnitude of this self-propagation velocity, $|\boldsymbol{u}|$, of a heton (traveling in a straight line) varies with the separation for the case when $\delta = 1$ and $|\Gamma| = 1$, where $\Gamma = \Gamma_1$ or Γ_2. Note that this velocity is bounded for a heton whereas the propagation velocity for a dipole increases without bound as the separation is decreased. For the heton, the separation for which

the propagation velocities are a maximum can be found by differentiating either (5.6) or (5.7) with respect to d, analytically. The resulting expression is equated to zero which gives a transcendental equation for d which is solved numerically. This distance is independent of Γ and δ and occurs at $d \approx 1.11$.

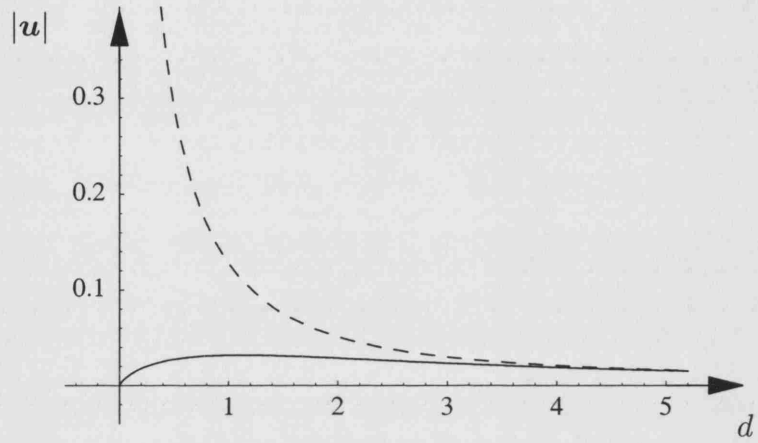

Figure 5.2: Self-propagation velocities for a heton (solid) and a dipole (dashed). These were found using equation (5.6) or (5.7) with $\delta = 1$ and $|\Gamma| = 1$, where $\Gamma = \Gamma_1$ or Γ_2.

Vortex pairs (both single layer and hetons) have the ability to trap and transport anomalous fluid large distances and are therefore a potentially important transport mechanism in the ocean. Indeed, Hogg and Stommel [1985] coined the term 'heton' since a heton transports heat in the direction of movement of the vortex pair. For example, an anticyclonic ($\Gamma < 0$) vortex in the upper layer will cause the interface between the two layers to be depressed at its centre and can thus be considered a warm anomaly. As stated in section 3.2 point vortices can be thought of as local anomalies (delta-functions) in the potential vorticity. To conserve potential vorticity, equations (3.1) and (3.2), the height of the vortex must be such that it compensates for the change in vorticity. This so called vortex stretching will have the effect of raising/lowering

the interface between the layers accordingly. Associated with the expansion (compression) of the upper layer is a warming (cooling). A cyclonic ($\Gamma > 0$) vortex in the lower layer is also warm as it causes the interface to be pulled down. This is precisely the arrangement of a heton (figure 5.3(a)) and thus the interface deformations or, equivalently, heat is transferred as the heton self-propagates. (Note, there is an analogous cold heton, figure 5.3(b).) Hogg and Stommel [1985] have calculated the relationship between the magnitude of the heat transported by a heton and the heton strengths and separation.

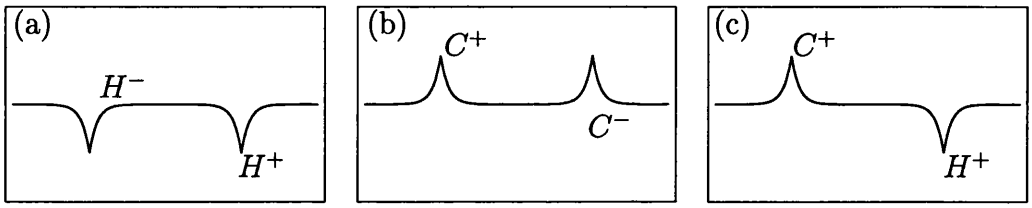

Figure 5.3: Some heton arrangements and the interface deformations they cause. (a) A hot heton. (b) A cold heton. (c) An anti-heton. Following Hogg and Stommel [1985], the $\pm$ signs represent the sign of the circulation. Warm anomalies are denoted H and cold anomalies, C.

Hogg and Stommel [1985] derive coupled ordinary differential equations for the trajectories of pairs of hetons. These are then solved numerically and the behaviour of the trajectories as δ, the heton strength and deformation radii vary, is discussed. They examine the interactions of hot-cold, hot-hot and cold-cold heton pairs. They also examine the dynamics of anti-hetons (figure 5.3(c)). These are a system of two vortices, one in each layer but having the same sign circulation. They tend to rotate about their centre rather than propagate large distances and hence will not be investigated here. Hogg and Stommel [1985] did not consider heton interaction with boundaries although, by symmetry, their hot-cold heton interaction results (their figure 3) could

be used to interpret motion of hetons near an infinitely long wall (occupying both layers) by employing the 'method of images'. This section aims to extend their study by examining heton motion near large scale topography of the type introduced in chapter 3.

Young [1985] also studied the interaction of two and four quasi-geostrophic vortices in a two-layer fluid, including hetons. As well as the trajectories of the component vortices, he examines the flow around hetons and dipoles. Importantly, he notes that an upper-layer (or lower-layer) dipole transports no lower-layer (upper-layer) fluid if $d < 1.72$. In contrast, the amount of trapped fluid transported by a heton increases as d decreases. Young [1985] examines heton collisions and also finds that hetons are able to 'exchange partners'.

Legg and Marshall [1993] use hetons to model the sinking and spreading phase of open-ocean deep convection. They used a 'cloud' of cold hetons to represent a patch of anomalously cold water resulting from open-ocean deep convection. Such 'clouds' were shown to be unstable and rapidly dispersed and thus represent a mechanism for the dispersal of cold water produced by deep convection.

More recent work on hetons has been done by Gryanik et al. [2000] who studied three-dimensional hetons embedded in a continuously stratified fluid. Further, Sutyrin et al. [2003] present numerical evidence for deep flows influencing the dynamics of upper-layer vortices. It is of interest therefore to model the behaviour of structures having both upper- and lower-layer vorticity anomalies (e.g. hetons) near topography like that considered here.

5.2 Problem formulation

The case where the heton self-propagation velocity is initially directed exactly perpendicularly towards the topography is investigated. Hetons which are initially incident at some non-right angle are not considered here. That is, each vortex comprising the heton induces an equal velocity on the other, which is normal to the topography. The depth ratio, δ, and the heton vortex strengths, Γ_1 and Γ_2, must be related through equation (5.8).

Note also, then, that initially $v_1 = v_2 = 0$ and, in terms of the upper-layer vortex parameters,

$$u_1 = u_2 = \frac{\Gamma_1}{2\pi}\frac{\delta}{1+\delta}\left(\frac{1}{2y_1} - K_1(2y_1)\right), \tag{5.9}$$

where without loss of generality $y_1 = -y_2$. Note that $\operatorname{sgn} u_1 = \operatorname{sgn} u_2 = \operatorname{sgn} \Gamma_1$ (see figure 5.2) and so $\Gamma_1 < 0$ (or $\Gamma_2 > 0$) for $u_1 = u_2 < 0$, i.e. a heton starting to the right of the topography ($x > 0$) propagates toward the topography.

In a sense, the following numerical experiments are more natural than those of chapter 4 in that the heton propagates in from infinity and so avoids the question, which arises in the single vortex case, of how the vortex came to be close to the topography in the first instance.

5.3 Results

A similar contour dynamics investigation is performed on the heton as was used for the single vortex case in chapter 4. The algorithm is adapted to include the effects of each vortex on the other (occupying a different layer), namely equations (5.2)–(5.5).

Figure 5.4 shows the heton trajectories for various depth ratios, δ, with $\Gamma_1 = -1$. In this case, the upper-layer vortex component of the heton is circulating

clockwise (anticyclonically) and is initially located at $(x_1, y_1) = (2, 0.25)$ and the lower-layer vortex is circulating anticlockwise (cyclonically) and is initially located at $(x_2, y_2) = (2, -0.25)$. In the absence of topography this two-layer vortex structure will propagate steadily in the negative x-direction. The upper-layer vortex path is indicated by the solid line and the filled circles represent the position of the upper-layer vortex at 10 time unit intervals. The lower-layer vortex path is indicated by the dashed line and the empty circles give the position of the lower-layer vortex at the same intervals. For the $\delta = 0.2$ case (figure 5.4(a)), runs up to $t = 100$ can be performed before end-effects produce inaccuracies. For $\delta = 1$ (figures 5.4(b)) runs up to $t = 70$ are possible and for $\delta = 5$ (figures 5.4(c)), $t = 40$ is the maximum before significant end-effects occur.

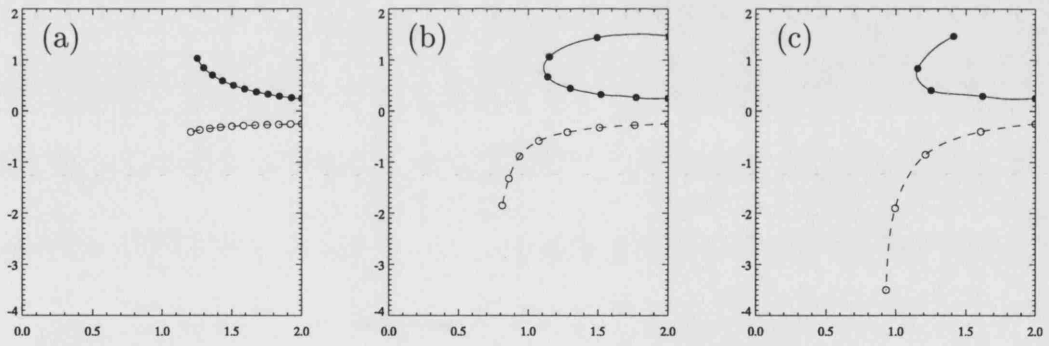

Figure 5.4: Heton trajectories with $\Gamma_1 = -1$ for (a) $0 < t < 100$, $\delta = 0.2$, (b) $0 < t < 70$, $\delta = 1$ and (c) $0 < t < 40$, $\delta = 5$. In all cases, the heton centre is initially located at $(2, 0)$ and $d = 0.5$. The solid line indicates the path of the upper-layer vortex and the dashed line, the lower-layer vortex.

The heton is expected to propagate in the negative x-direction, towards the topography. As the heton approaches, the effect of the topography increases and the motion of the upper- and lower-layer vortices begins to evolve according to the theory developed in chapter 3. The lower-layer vortex will be mainly

affected by its image which will cause it to be advected in the negative y-direction. Meanwhile, the upper-layer vortex motion is mostly determined by the deflected contour. This is clearly seen in figure 5.4(c), the $\delta = 5$ case. Here, according to equation (5.8), there is a relatively weak (i.e. small circulation) vortex in the upper layer and a strong (i.e. large circulation) vortex (with a correspondingly strong image) in the lower layer. The image effect is not so pronounced on the upper-layer vortex, therefore it remains in the vicinity of any contour displacements (as mentioned in section 4.4) and will interact with it in a nonlinear way. (See also figure 5.5 where each successive frame represents the vortex position as shown by the circles in the vortex path plot.) In this case, the upper-layer vortex and the deflected contour form a dipole (figure 5.5, $t = 40$), which propagates in the positive y-direction and away from the topography. The effects of the topography have caused the heton to split and it can no longer be considered a coherent two-layer structure. The upper- and lower-layer vortex paths (and to a large extent, the contour displacement) exhibit similar characteristics to those seen in figures 4.6 and 4.4 respectively. The heton splitting is also seen in the $\delta = 0.2$ and $\delta = 1$ cases (figures 5.4(a) and (b)). The splitting takes longer to occur in these two cases because the heton translation speed is proportional to $\delta/(1 + \delta)$ (equation (5.9)) hence smaller depth ratios give smaller velocities perpendicular to the topography, so it takes a longer time for the vortices to reach the region where topographic effects become noticeable.

As mentioned in section 5.1, these results are similar, at least for the lower-layer vortex, to those in Hogg and Stommel [1985] (their figure 3), where they consider the interaction of (initially untilted, i.e. zero separation) hot and cold hetons of equal strength. In both Hogg and Stommel [1985] and figure 5.4

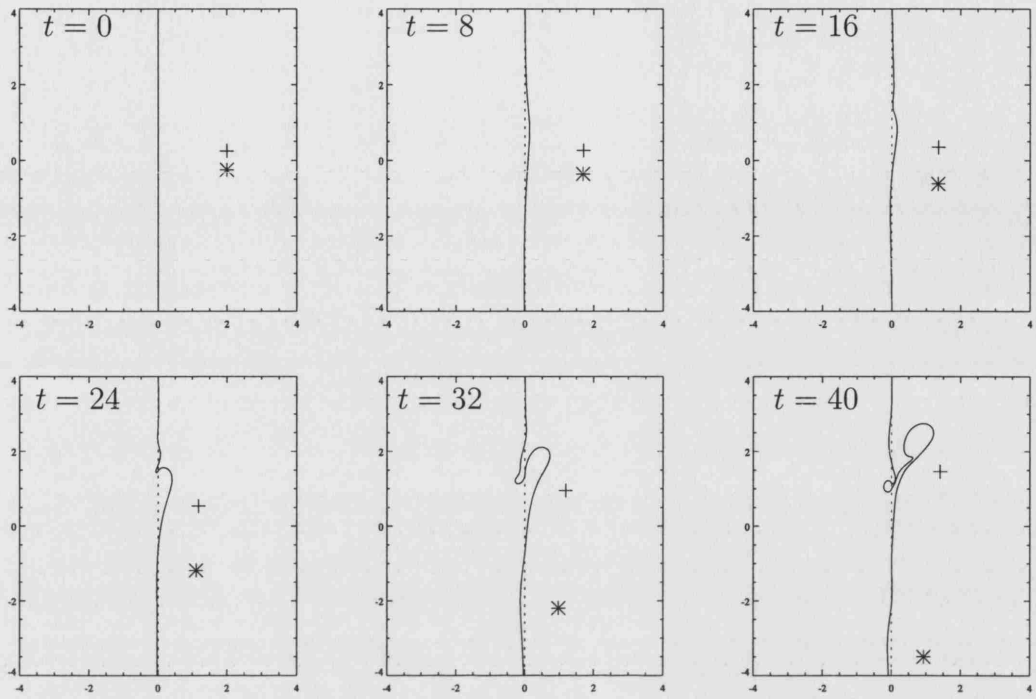

Figure 5.5: Contour displacement for $0 < t < 40$, $\delta = 5$ and $\Gamma_1 = -1$. The heton centre is initially located at $(2, 0)$ and $d = 0.5$. The cross indicates the position of the upper-layer vortex and the star, the lower-layer vortex.

the hetons split as they approach each other or the topography. However, the subsequent behaviour of the upper-layer vortex for this experiment differs in that it is reflected via the dipole mechanism.

The polarity of the heton is now reversed. That is, the upper-layer vortex component of the heton is circulating anticlockwise (cyclonically) and is initially located at $(x_1, y_1) = (2, -0.25)$ and the lower-layer vortex is circulating clockwise (anticyclonically) and is initially located at $(x_2, y_2) = (2, 0.25)$. Figure 5.6 shows the heton trajectories for various depth ratios, δ, with $\Gamma_1 = 1$. The initial path of the heton is as in the $\Gamma_1 = -1$ case, namely towards the topography. Also, as before, for the $\delta = 0.2$ case (figure 5.4(a)), runs up to $t = 100$ can be performed before end-effects produce inaccuracies. For $\delta = 1$

and $\delta = 5$ (figures 5.4(b) and (c)) runs up to $t = 70$ and $t = 40$, respectively, are possible before significant end-effects occur.

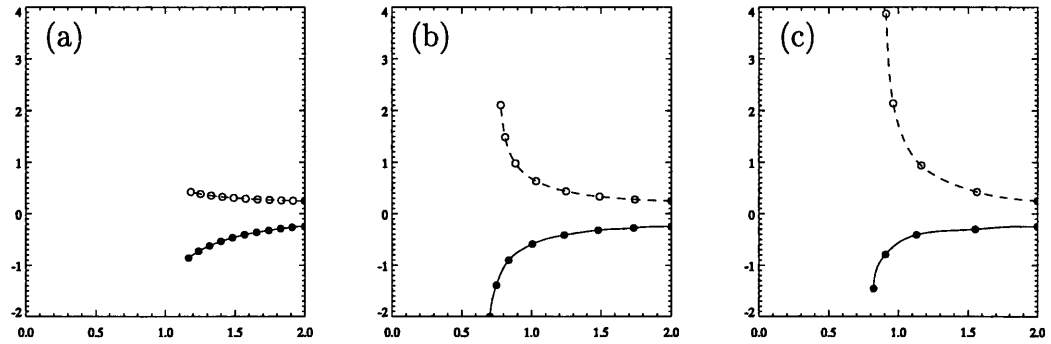

Figure 5.6: Heton trajectories with $\Gamma_1 = 1$ for (a) $0 < t < 100$, $\delta = 0.2$, (b) $0 < t < 70$, $\delta = 1$ and (c) $0 < t < 40$, $\delta = 5$. In all cases, the heton centre is initially located at $(2, 0)$ and $d = 0.5$. The solid line indicates the path of the upper-layer vortex and the dashed line, the lower-layer vortex.

Figures 5.6(a), (b) and (c) all exhibit a similar splitting to the $\Gamma_1 = -1$ case. The reasons for this behaviour are also the same. The lower-layer vortex (circulating in the opposite sense to before) is now advected in the positive y-direction by the action of its image and the upper-layer vortex remains local to, and is advect by, the contour displacements.

Again, figure 5.6(c) which has the largest value of the depth ratio shows this behaviour most dramatically due to the larger perpendicular speeds. Figure 5.7 shows the contour displacement for this particular run. That is, $0 < t < 40$, $\delta = 5$ and $\Gamma_1 = 1$.

It is worth noting that, in the $\Gamma_1 = -1$ case, the anticyclonic upper-layer vortex tears fluid from the shallow side of the step forming a dipole which back reflects, much like the single vortex experiment of figure 4.6. For $\Gamma_1 = 1$ it therefore might be expected that the upper-layer component of the heton crosses the step as in figure 4.7. However, this is not the case. The upper-

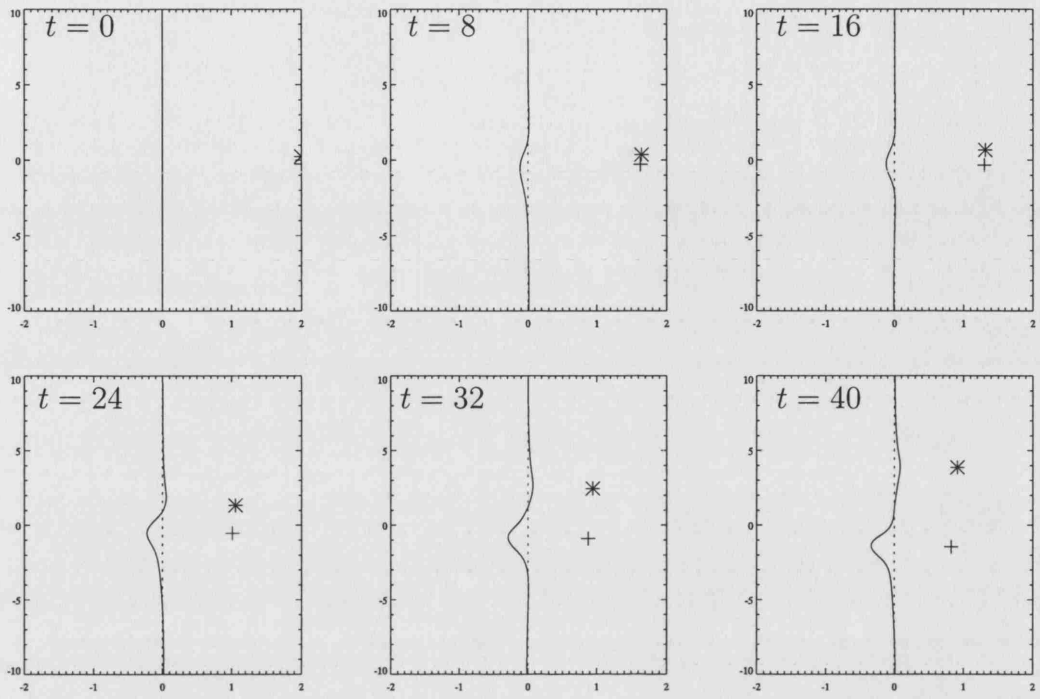

Figure 5.7: Contour displacement for $0 < t < 40$, $\delta = 5$ and $\Gamma_1 = 1$. The heton centre is initially located at $(2, 0)$ and $d = 0.5$. The cross indicates the position of the upper-layer vortex and the star, the lower-layer vortex.

layer vortex, being a cyclone, tends to propagate parallel to the step rather than cross it. This is because the upper-layer vortex is far enough from the topography as to be unable to wrap up the contour and the linear result of a upper-layer vortex and its associated localised disturbance in the contour propagating in the negative y-direction ensues.

Again, this behaviour is similar to that of Hogg and Stommel [1985] in their interaction of a hot and cold heton with equal strengths. Differences between this experiment and theirs arise due to the fact that vortex components don't have equal strength, i.e. these satisfy (5.8). The trajectories are also influenced by the contour deflections, in particular when the upper-layer vortex is an anticyclone.

5.4 Discussion

Motivated by the work of chapters 3 and 4, where the motion of a point vortex near large amplitude topography in a two-layer fluid was studied, in this chapter, the motion of an arrangement of two vortices (called a heton) near similar topography was investigated. It is emphasised that this arrangement of vortices provides a natural mechanism for vortices to come close to and interact with the step rather than just 'switching on' vortices as was required in chapters 3 and 4.

Studies were restricted to the case where the heton motion is initially perpendicular to the topography. Contour dynamics results showed that the heton splits regardless of the polarity of the heton. Once the heton gets close to the topography, as in chapter 4, the lower-layer vortex moves under the influence of an 'image' in the topography and the upper-layer vortex remains local to disturbances in the potential vorticity across the contour and exhibits nonlinear behaviour. Depending on the polarity of the heton, the upper-layer vortex may form a dipole with fluid torn from the shallow side or propagate parallel to the topography. As expected and required, the motion subsequent to splitting (of the vortices originally comprising the heton) and the evolution of the contour is found to be consistent with that of chapter 4. There are some differences (i.e. the upper-layer vortex in figure 5.7 doesn't cross the step) which are due to the differing vortex strengths.

Chapter 6

The motion of a dipole near large amplitude topography in a two-layer fluid

6.1 Introduction

A configuration of two vortices in the same layer is called a dipole. Dipoles are much studied and interesting structures since they are able to trap and transport fluid large distances, see for example Lamb [1932] and Batchelor [1967]. Moreover, they are relatively stable structures. For example, Gorshkov et al. [2000] demonstrate analytically that dipoles consisting of vortex patches remain coherent when subject to perturbations in the background flow whereas monopoles tend to destruct. Further, as in the numerical experiments of McWilliams [1990b] (see his figure 1), they can arise from 'chaotic', turbulent, random, initial conditions and persist for long times (see also McWilliams 1990a). They are, in a sense, attractors of the flow. Dipoles consisting of vor-

tices with the same sign circulation rotate about their centres, whereas dipoles consisting of equal and opposite sign vortices advect each other along parallel paths. The self-propagation velocity of a dipole increases as the separation between the vortices decreases. This has already been demonstrated (in figure 5.2) for a dipole located in one layer of a two-layer fluid.

Given that they have the ability to self-propagate large distances, oppositely signed dipoles will invariably encounter varying topography and barriers. In the absence of viscous effects, Saffman [1979] shows, both analytically and numerically, that a symmetrical dipole consisting of two patches of oppositely signed vorticity propagating towards a plane wall at right angles must approach the wall monotonically, i.e. the velocity of the (centroids of the) vortices towards the wall does not change sign. The vortices begin to separate under the action of the image vorticity in the wall and the motion of their centres asymptote to a straight line parallel to the wall as they propagate in opposite directions. A lower-layer dipole approaching the large amplitude topography studied here is expected to exhibit similar behaviour.

In contrast to the results of Saffman [1979], the numerical investigations of Orlandi [1990] show that dipoles approaching walls may rebound if the effects of viscosity are included. The dipole rebounds due to the creation of vorticity at the wall in a viscous boundary layer, i.e. this vorticity sheet at the wall becomes unstable and detaches from the wall due to the influence of the dipole. The sheet forms two vortices which pair up with the original dipole (each new pair consisting of two oppositely signed vortices) and stop its constituent vortices splitting and propagating away from each other, parallel to the wall. Instead the new pairs form two dipoles which propagate away from the wall. Further motions are discussed in more detail in Orlandi [1990]. Viscosity will not

be considered in the present study. However, potential vorticity conservation can produce oppositely signed vorticity in inviscid fluids (as in their boundary layer) which will in turn effect the resultant motion of dipoles. For example, the potential vorticity in the numerical and laboratory experiments of Carnevale et al. [1997] is generated by the β-effect. Dipoles approaching a wall advect fluid parallel to the wall (due to image effects) this fluid in turn acquires relative vorticity as potential vorticity is conserved (owing to the β-effect) creating new dipoles which reflect away from the wall. In this work the topography plays an analogous role to the β-effect and the associated potential vorticity conservation will influence the subsequent motion of dipoles.

Experimental studies of dipoles have been conducted by Couder and Basdevant [1986], among others. They find dipoles are produced spontaneously in the turbulent wake field in a thin soap film and can transport energy from one area to another. The study of dipoles (like that of hetons) is therefore relevant and important to transport processes in the ocean.

Oceanic observations of dipoles are described in Merrell and Morrison [1981]. They observed an anticyclone and a cyclone in close proximity in the western Gulf of Mexico near the steep topographical gradients there. This 'dipole' was able to transport fluid eastward at the significant rate of 29.7×10^6 m^3 s^{-1}. Also, Vidal et al. [1994] have observed cyclonic-anticyclonic-cyclonic systems (also in the Gulf of Mexico) which dominate the local circulation. Systems of interacting vortices, including dipoles, are observed and therefore have important oceanic applications.

Recently, Johnson and McDonald [2004c] have studied, analytically and numerically, the motion of dipoles comprising of both singular vortices and vortex patches in a one-layer non-rotating fluid with a rigid-lid (and so differ-

ences between their study and that presented in this chapter are expected). They find that dipoles approaching normally to step topography separate as they cross from deep to shallow water. If, on the other hand, they approach from shallow to deep water the separation between the vortices comprising the dipole decreases and it accelerates. Importantly, they found that point vortices, in most circumstances, well-modeled the trajectories of the centroids of finite area vortex patches.

Further, Richardson [2000] has investigated the motion of dipoles over continuously varying topography in a non-rotating fluid. He finds that isolated vortices propagate along isobaths and the effect of topography on a dipole is to reduce or increase the separation between the component vortices, producing larger (or smaller) propagation speeds depending on whether they are translating from shallow to deep fluid or vice versa, respectively.

In this chapter the motion of vortex configurations near large amplitude topography is further investigated by examining the behaviour of dipoles. Both lower- and upper-layer dipoles incident at right angles to the isobath are considered in sections 6.2 and 6.3 respectively.

6.2 Lower-layer dipoles

In chapter 4 the motion of single point vortices near large amplitude topography was investigated. Vortices were 'switched on' a certain distance away from the topography and the subsequent motion was investigated. The dominant motion was parallel to the step and topographic waves could be radiated depending on the sign of the vortex circulation. Rather than just 'switching on' vortices, the self-propagation of dipoles provides a natural mechanism for vortices to approach topography. It is therefore possible and of interest to

compare the motion of dipoles approaching topography to the single vortex experiments of chapter 4. The most direct comparison can be made between the motion of lower-layer vortices and lower-layer dipoles since a dipole in the lower-layer is expected to split under the action of its image and the two vortices subsequently propagate independently and parallel to the step as the single vortices of chapter 4 (The motion of upper-layer dipoles which may not split and therefore exhibit different behaviour from single upper-layer vortices will also be compared in section 6.3.).

To, fairly, quantitatively compare single lower-layer vortices and lower-layer dipoles (after splitting) the dipole is required to propagate at approximately the same distance from the topography as does the single-layer vortex of chapters 3 and 4. The initial lower-layer dipole parameters must therefore be carefully chosen. These parameters are calculated by appealing to an approximation of the streamfunction of a lower-layer dipole.

The streamfunction in the lower layer of a lower-layer dipole near large amplitude topography in a two-layer fluid may be approximated by replacing the topography with a wall which extends throughout the depth of both layers. Exact streamfunctions would include effects owing to the deflections of the upper-layer contour. These effects are, however, negligible for small depth ratios (see equations (3.82) and (3.83) and figure 3.10).

The streamfunction for a lower-layer dipole near a wall is given by adding four streamfunctions, two corresponding to the dipole itself and two more due to its image in the topography. In this case, the dipole streamfunction is made up of two vortices with equal and opposite circulation, themselves each satisfying equation (3.12), i.e. each of the four components of the total dipole

streamfunction has the form

$$\psi_2 = \frac{1}{1+\delta}\frac{\Gamma}{2\pi}\log\left(\left((x-x')^2+(y-y')^2\right)^{1/2}\right) - \frac{\delta}{1+\delta}\frac{\Gamma}{2\pi}K_0\left(\left((x-x')^2+(y-y')^2\right)^{1/2}\right), \quad (6.1)$$

where (x', y') is the location of the relevant vortex and the circulation, Γ, is defined as figure 6.1. Without loss of generality, the dipole centre is assumed

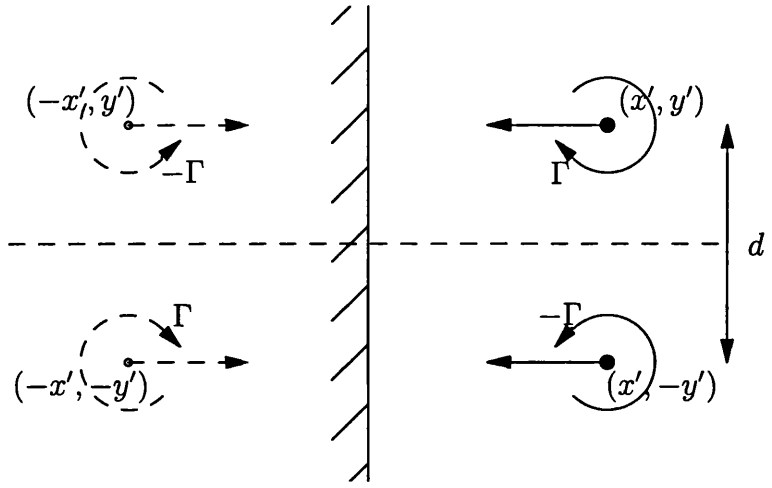

Figure 6.1: Dipole parameters. Also shown is the lower-layer dipole image behind the topography at $x = 0$.

to coincide with the x-axis. By symmetry, for the $\delta = 0$ case, the dipole centre will lie on $y = 0$ for all time and the dipole streamfunction, ψ_D, is given by

$$\psi_D = \psi_2(\Gamma, x, y, x', y') + \psi_2(-\Gamma, x, y, x', -y') + \psi_2(-\Gamma, x, y, -x', y') + \psi_2(\Gamma, x, y, -x', -y'), \quad (6.2)$$

where, due to the choice of topography, $x' > 0$, again see figure 6.1.

The motion of (each vortex component of) the dipole may now be calculated from (6.2) by examining the gradient of ψ_D less the singular part of the

streamfunction at the vortex under consideration, all evaluated at the vortex centre, i.e. the gradient of

$$\psi_D(x',y') = \psi_2(-\Gamma, x = x', y = y', x', -y') + \psi_2(-\Gamma, x = x', y = y', -x', y) + \psi_2(\Gamma, x = x', y = y', -x', -y'). \quad (6.3)$$

Using (6.1) this becomes

$$\psi_D(x',y') = -\frac{\Gamma}{2\pi}\frac{1}{1+\delta}\left(\log(2x') + \log(2y') - \log\left(2\sqrt{x'^2+y'^2}\right)\right) + \frac{\Gamma}{2\pi}\frac{\delta}{1+\delta}\left(K_0(2x') + K_0(2y') - K_0\left(2\sqrt{x'^2+y'^2}\right)\right). \quad (6.4)$$

Recall that, to compare with the single point vortex experiments, each vortex component of the dipole should end up a distance $x' = 0.5$ from the topography. For the $\delta = 0$ case the parameters required for this are straightforward to calculate. The method is detailed in Lamb [1932] and reproduced here for completeness. The velocities of the vortex centre are given by differentiating (6.4), i.e.

$$u' = -\frac{\partial \psi_D}{\partial y'} = \frac{dx'}{dt} = \frac{\Gamma}{2\pi}\frac{x'^2}{y'(x'^2+y'^2)}, \quad (6.5)$$

and

$$v' = \frac{\partial \psi_D}{\partial x'} = \frac{dy'}{dt} = -\frac{\Gamma}{2\pi}\frac{y'^2}{x'(x'^2+y'^2)}. \quad (6.6)$$

Dividing (6.6) by (6.5) yields a separable differential equation for the vortex centre (x', y'),

$$\frac{dx'}{x'^3} + \frac{dy'}{y'^3} = 0, \quad (6.7)$$

which has solution

$$\frac{1}{x'^2} + \frac{1}{y'^2} = K, \quad (6.8)$$

where K is an arbitrary constant. This solution is depicted in figure 6.2 for different values of K (see also Johnson and McDonald 2004c). As $t \to \infty$,

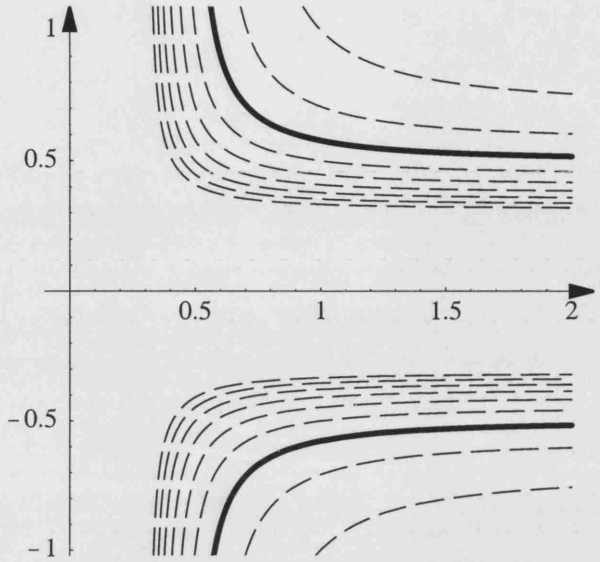

Figure 6.2: Dipole trajectories calculated analytically. The solid line indicates the trajectory for which the vortices asymptote toward $x = 0.5$.

$y' \to \pm\infty$ and to compare with the single vortex experiments of chapter 4 it is required that $x' \to 0.5$. Substituting these values into equation (6.8) gives $K = 4$. Therefore, choosing a dipole starting at $x' = 2$, for example, requires initial values of y' given by

$$y' = \pm\frac{1}{\sqrt{(4-(1/2)^2)}} = \pm\frac{2}{\sqrt{15}}. \tag{6.9}$$

If $\delta \neq 0$ the parameters are found by examining the level curve of (6.4) which passes through $x_p = 0.5$. (Recall that this is an approximation of the streamfunction of a lower-layer dipole with the topography replaced by a wall.) In general, the particular level curve of (6.4) that passes through (x_p, y_p) is a solution to the equation

$$\psi_D(x', y') - \psi_D(x_p, y_p) = 0. \tag{6.10}$$

Assuming $|y_p| \to \infty$, (6.10) becomes

$$\frac{1}{2}\log\left(\frac{x_p^2}{x'^2}+\frac{x_p^2}{y'^2}\right) + \delta\left(K_0(2x')+K_0(2y')-K_0\left(2\sqrt{x'^2+y'^2}\right)-K_0(2x_p)\right)=0. \quad (6.11)$$

Now given a depth ratio, δ and choosing the dipole to start at $x' = 2$ and such that each vortex comprising the original dipole asymptotes to a distance $x_p = 0.5$ from the topography, the initial dipole separation, $2y'$, can be found by solving (6.11) numerically. Figure 6.3 shows the variation of this initial dipole separation as the depth ratio, δ is varied given that $x_p = 0.5$ and $x' = 2$. As $\delta \to \infty$ the value of $d \to 1.0024$ as shown by the dashed asymptote in figure 6.3. Further, observe that, as expected, for $\delta = 0$ the initial separation $d = 4/\sqrt{15} \approx 1.0328$, which is exactly the same as derived using the method detailed by Lamb [1932], equation (6.9).

Again note, equation (6.11) and figure 6.3 don't take into account the effect the displacements of upper-layer fluid have on the position of the lower-layer vortices. However, these effects are small (see the vortex back-reaction section 3.5.3) and for the purposes of comparing dipole paths with the single-layer vortex experiments of chapter 4, (6.11) provides an excellent first approximation of $2y'$ for a dipole passing through x_p.

Again the contour dynamics algorithm is used to investigate the response in the upper layer as a lower-layer dipole approaches the topography and, in turn, the effects any upper-layer displacements have on the motion of the lower-layer dipole. As in chapter 5, the contour dynamics algorithm has to be modified to include the effects of each vortex on the other (occupying the same the layer), namely equation (6.4).

Figure 6.4 shows the contour evolution for a lower-layer dipole with $\delta = 0$

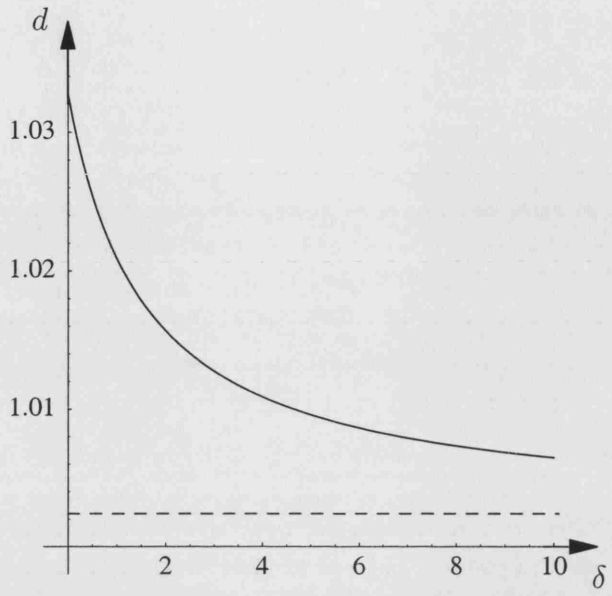

Figure 6.3: Variation of initial dipole separation, d, required for the vortices to asymptote toward $x = 0.5$ with the ratio of the layer depths, δ. The value of d corresponding to the limit $\delta \to \infty$ is represented by the dashed asymptote.

and $\Gamma = -1$ (with Γ defined as in figure 6.1). The dipole is initially located at $x' = 2$ and self-propagates in the negative x-direction. It subsequently splits under the influence of its image when sufficiently close to the topography (as the method of images and analytical streamlines (figure 6.2) predict, see also Saffman 1979). The initial separation of the dipole is such that $x' \to 0.5$ as $t \to \infty$ (calculated from (6.11)). In this way, comparison with figures 4.2 and 4.4 is possible. As in figure 4.2 the anticyclonic component of the dipole is advected in the positive y-direction. It causes a disturbance in the contour which remains localised near the vortex. The cyclonic part causes another disturbance (of opposite sign, as in figure 4.4) which propagates in the negative y-direction with the cyclonic vortex and a steady topographic wave develops in its wake. Note that, as expected, magnitudes and wavelengths of the initial disturbances and the topographic waves of figures 4.2, 4.4 and 6.4 are in excellent agreement.

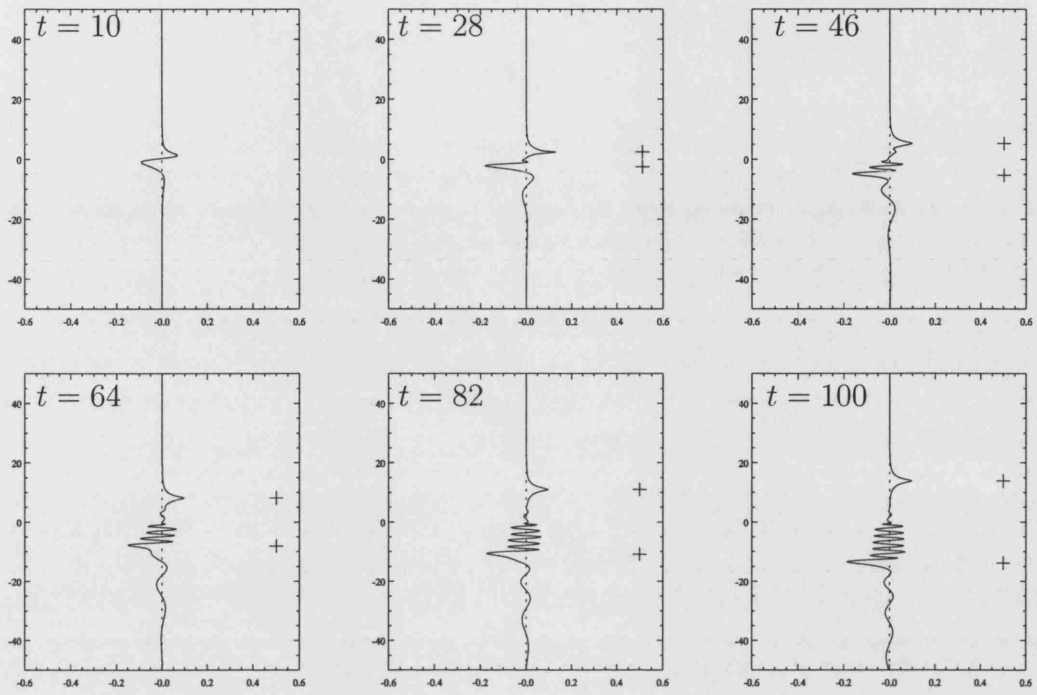

Figure 6.4: Evolution of the contour for a lower-layer dipole with $\delta = 0$ and $\Gamma = -1$. The dipole centre is initially located at $(2, 0)$ and $d = 4/\sqrt{15}$ such that the vortices end up at $x_p = 0.5$.

Figure 6.5 shows lower-layer dipole trajectories for various depth ratios. In each case d is calculated using equation (6.11) so that the vortices end up at $x_p \approx 0.5$. The final x-displacement (in the $\delta = 0$ case) is not exactly 0.5 due to end effects. The lower-layer vortices can be made to asymptote to exactly 0.5 by increasing the length of the topography, however, this increases computing time, hence the compromise shown here. The symbols represent the positions of the lower-layer dipoles at 10 time unit intervals. Figure 6.5 compares well with figures 4.3 and 4.5. As in figure 4.5, the cyclonic component is advected in the negative y-direction. Also, as δ is increased the vortex spends more time in the vicinity of any transient waves causing increasingly significant displacement in the x-direction. The anticyclonic component is advected in

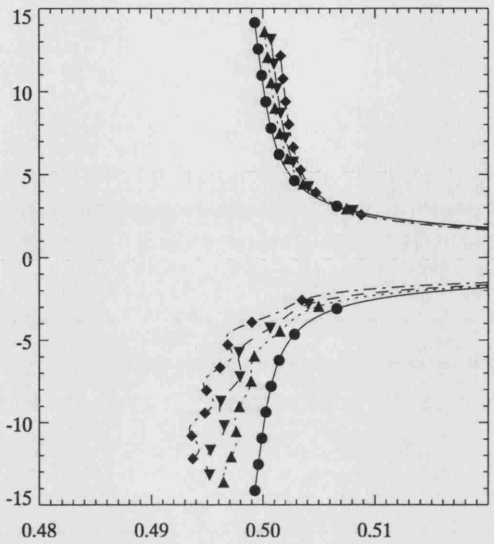

Figure 6.5: Lower-layer dipole trajectories for $0 < t < 100$. The initial separation d is calculated so that each vortex ends up at $x_p \approx 0.5$. Other parameter values are $\Gamma = -1$, $x' = 2$, $\delta = 0$ (solid line), $\delta = 0.1$ (dotted line), $\delta = 0.2$ (dashed line) and $\delta = 0.5$ (dot-dashed line). The symbols represent the positions of the lower-layer dipoles at 10 time unit intervals.

the positive y-direction and behaves in a similar way to those in figure 4.3 as δ is increased due to the transient wave effects. Note that, in contrast to section 4.2 where anticyclonic vortices are unable to produce, and therefore be affected by, topographic waves, the generation of topographic waves by a dipole (figure 6.4) can affect both the constituent cyclonic and anticyclonic vortex trajectories.

6.3 Upper-layer dipoles

In chapter 4 the length of time over which the contour dynamics experiments could be performed was restricted due to end effects. In contrast, in this section, that time is restricted by the number of nodes. Due to the highly non-

linear nature of the interaction between the contour and upper-layer vortices, the number of nodes quickly becomes unmanageable. Nonetheless, interesting conclusions can be drawn. The behaviour of upper-layer dipoles depends on whether they approach the topography from the deep ($x_0 > 0$) or the shallow ($x_0 < 0$) side. Each case is treated separately.

6.3.1 $x_0 > 0$

Figure 6.6 shows the contour evolution for an upper-layer dipole with initially positive x-position for the case where $\delta = 0.2$ and $\Gamma = -1$ (and defined as in figure 6.1). This value of δ is the most realistic for oceanic applications and so it could be expected that dipoles approaching steep topography would be deflected in this way (see also chapter 7). It is observed that the dipole prop-

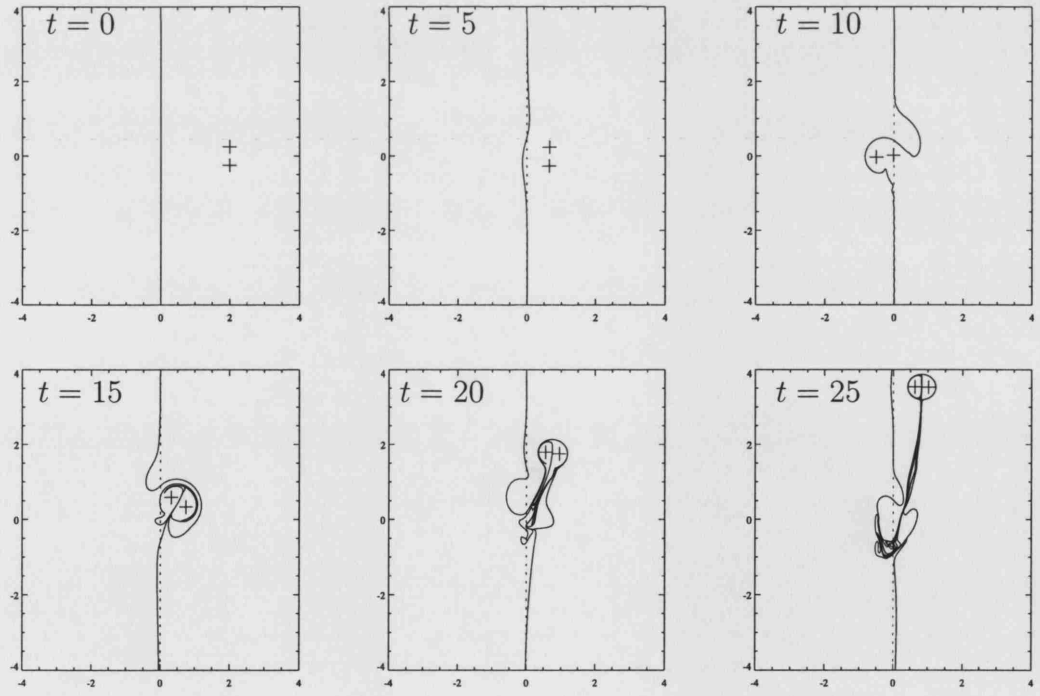

Figure 6.6: Evolution of the contour for an upper-layer dipole with $\delta = 0.2$ and $\Gamma = -1$. The dipole centre is initially located at $(2, 0)$ and $d = 0.5$.

agates towards the topography causing displacements of the contour initially overlying the step ($t = 5$). Once the vortices cross the topography they begin to turn clockwise as they are engulfed by fluid rotating clockwise (due to the conservation of potential vorticity) itself having been advected from the shallow to the deep side of the step ($t = 10$, see also figure 6.8, which depicts a blow up of this particular frame showing the directions of the rotation of different parts of the fluid). The dipole reverses direction and returns to the shallow region dragging fluid with it. Now, the structure is wrapped again by anti-clockwise rotating fluid ($t = 15$) which acts to deflect the dipole back towards the topography ($t = 20$). The dipole might be expected to continue oscillating over the step due to the periodic wrapping of the contour, however, in this case the subsequent motion is almost parallel to the topography ($t = 25$). This is due to the fact that for small δ, relatively little secondary entrainment occurs once the dipole returns to the shallow region, i.e. little wrapping of ambient fluid about the dipole ($t = 15$), and the dominant motion of the dipole after returning to the shallow region is due to its self-propagation parallel to the topography.

Figure 6.7 shows the upper-layer dipole trajectories for various depth ratios, δ, for a dipole approaching from the deep side of the topography ($x_0 > 0$) also with $\Gamma = -1$. For the $\delta = 0.2$ case, runs up to $t = 30$ only, can be performed until the number of nodes becomes unmanageable. For $\delta = 1$, $t = 25$ is the maximum and for $\delta = 5$, $t = 20$. The filled circles represent the position of the upper-layer dipole at 5 time unit intervals, i.e. for $\delta = 0.2$ the circles correspond exactly to the position of the dipole shown in each successive frame of the contour plot, figure 6.6.

In each case the dipole propagates towards the topography and at least one

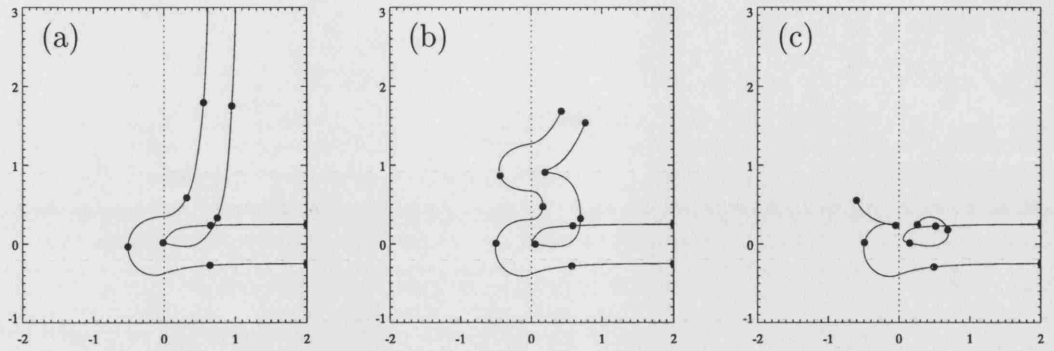

Figure 6.7: Dipole trajectories with $\Gamma = -1$ for (a) $0 < t < 30$, $\delta = 0.2$, (b) $0 < t < 25$, $\delta = 1$ and (c) $0 < t < 20$, $\delta = 5$. In all cases, the dipole centre is initially located at $(2, 0)$ and $d = 0.5$. The filled circles represent the position of the upper-layer dipole at 5 time unit intervals.

vortex crosses it. They begin to turn clockwise as explained above and reverse direction. For the $\delta = 1$ case (figure 6.7(b)) this process continues, creating the oscillating path alluded to above. As the process continues the oscillations become less dramatic due to the 'shielding' (or reduced net circulation) effect the wrapped up contour has on the dipole. Note that now the dipole remains a coherent structure, i.e. in contrast to the lower-layer example, it does not split. This is especially true for the $\delta = 0.2$ and $\delta = 1$ cases.

As the ratio of the layer depths, δ, increases more fluid can be wrapped around the dipole and hence the dipole will stay in the vicinity of any further contour disturbances. Therefore for small δ (figures 6.7(a) and 6.6 where $\delta = 0.2$) relatively little secondary wrapping occurs and the dominant motion of the dipole after returning to the shallow region is in the positive y-direction, due to self-propagation. For large δ (figure 6.7(c) where $\delta = 5$) much fluid is entrained and the dipole quickly becomes shielded. Therefore, the subsequent motion is due to a shielded dipole which behaves as if it is circulating in one sense only and hence doesn't self propagate, rather, it remains local to any

further contour displacements.

The oscillatory behaviour of propagating dipoles about potential vorticity gradients has also been observed by Nycander and Isichenko [1990], Hesthaven et al. [1993] and Zabusky and McWilliams [1982]. Nycander and Isichenko [1990] and Hesthaven et al. [1993] describe the motion of (tilted) dipoles in a constant potential vorticity gradient (due to the β-effect) and find oscillations due to the periodic trapping and release of fluid particles by the dipole. Both Nycander and Isichenko [1990] and Hesthaven et al. [1993] consider dipoles consisting of point vortices both analytically and numerically, however Nycander and Isichenko [1990] study the short time oscillatory motion whereas Hesthaven et al. [1993] generalise to investigate the long time behaviour where the oscillations relax to a steady uni-directional propagation. The oscillations are caused by the β-effect in these works and are analogous to the topographic effects in the present study. Consequently, similar oscillatory and the subsequent relaxation behaviour is observed here. Hesthaven et al. [1993] also explain, through conservation of potential vorticity arguments, that eastward propagating dipoles are stable with respect to these oscillations whereas westward propagating dipoles are unstable to small perturbations, i.e. they perform a large loop, changing direction and become eastward propagating dipoles. Zabusky and McWilliams [1982] also find oscillatory motion in their analytical and numerical study of point potential-vortices on the β-plane. They also explain that the motion is due to the conservation of potential vorticity, i.e. they use a 'modulated' representation in which the vortices conserve their potential vorticity by allowing the strength of their circulation to vary, causing the oscillations.

Note that all dipoles, regardless of their strength, will turn back towards

the step once they have crossed it. A dipole consisting of vortices with large circulations, $|\Gamma| \gg 1$, will 'punch' into the contour initially overlying the step, however it will always drag fluid it which acts to turn it clockwise (figure 6.8). Subsequently the dipole and fluid act as a single clockwise rotating structure. Note that the effects of this turning may not be seen until large times for such strong dipoles.

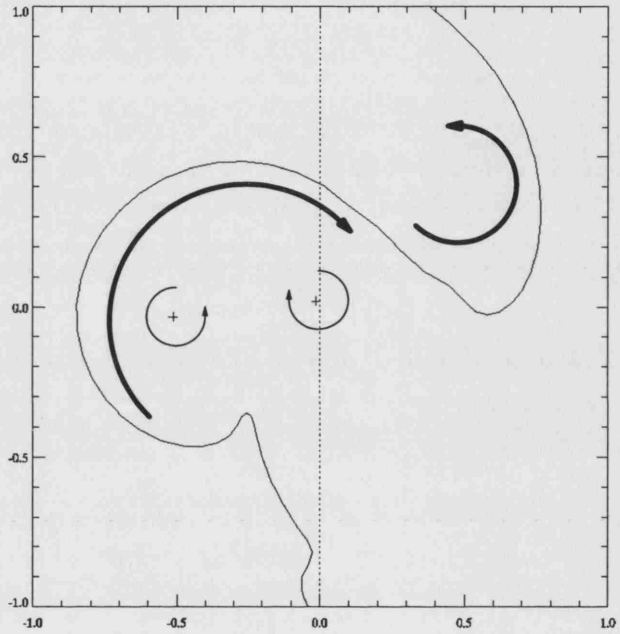

Figure 6.8: The upper-layer dipole and contour with $\delta = 0.2$ and $\Gamma = -1$ at $t = 10$ (detail of figure 6.6, $t = 10$). The dipole turns back towards the step under the influence of the clockwise rotating fluid (large bold arrow) which has been advected from deep to shallow water. Note also the fluid rotating anticlockwise (small bold arrow) which has been advected from shallow to deep water. The vortex circulations within the dipole are indicted by the small normal-weight arrows.

6.3.2 $x_0 < 0$

Figure 6.9 shows a typical contour evolution for the upper-layer dipole with initially negative x-position and with $\Gamma = 1$ (referring to the vortex with $y_0 > 0$). This particular figure depicts the $\delta = 0.2$ case. Clearly, the behaviour

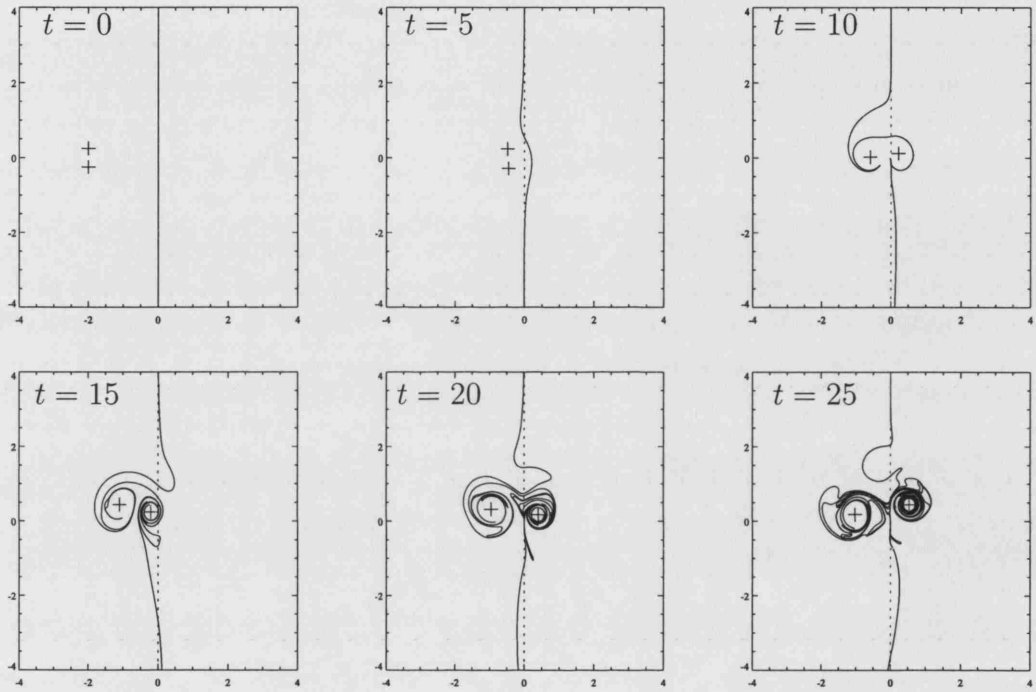

Figure 6.9: Evolution of the contour for an upper-layer dipole with $\delta = 0.2$ and $\Gamma = 1$. The dipole centre is initially located at $(-2, 0)$ and $d = 0.5$.

of a dipole with $x_0 < 0$ differs to the previous experiment, where $x_0 > 0$. First, the dipole causes displacements of the contour initially overlying $x = 0$ ($t = 5$) of the opposite sign to the $x_0 > 0$ case. However, in this case, only one vortex component of the dipole manages to cross the step, $x = 0$ ($t = 10$). The vortex that remains on the shallow ($x < 0$) side of the step is able to wrap up the contour consisting of fluid initially from the $x > 0$ region, this fluid is therefore rotating clockwise and in the opposite sense to the vortex itself. The result is a vortex-like structure with a net circulation less than that of

the original vortex. This vortex is 'shielded' from the other vortex component of the dipole and they have a reduced influence on each other. Consequently the vortex which has crossed the step is also able to wrap up the contour ($t = 15$), the fluid contained in which is again rotating in the opposite sense to the vortex, creating a further shielding. Thus, the vortices have a reduced net circulation and, therefore, reduced influence on one another, have no great y-displacement and propagate as if they are separate entities ($t = 20$). The subsequent behaviour ($t = 25$) is similar to that shown in chapter 4 in that anticyclones are located in $x > 0$ and cyclones in $x < 0$ for large times.

Figure 6.10 shows the upper-layer dipole trajectories for various depth ratios, δ, for a dipole starting on the shallow side of the topography ($x_0 < 0$) also with $\Gamma = 1$ (referring to the vortex with $y_0 > 0$). Again, for the $\delta = 0.2$ case, runs up to $t = 30$ only, can be performed until the number of nodes becomes unmanageable. For $\delta = 1$, $t = 25$ is the maximum and for $\delta = 5$, $t = 20$. Again, the filled circles represent the position of the upper-layer dipole at 5 time unit intervals.

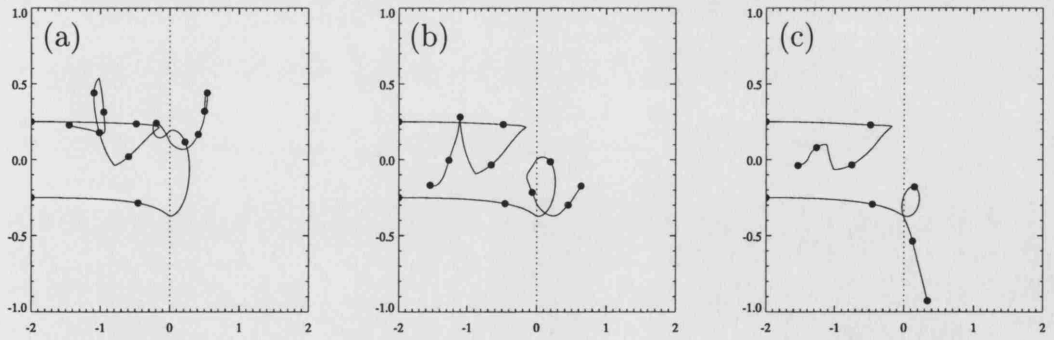

Figure 6.10: Dipole trajectories with $\Gamma = 1$ for (a) $0 < t < 30$, $\delta = 0.2$, (b) $0 < t < 25$, $\delta = 1$ and (c) $0 < t < 20$, $\delta = 5$. In all cases, the dipole centre is initially located at $(-2, 0)$ and $d = 0.5$. The filled circles represent the position of the upper-layer dipole at 5 time unit intervals.

Again, the dipoles propagate towards the topography, this time from the shallow side of the step. Only one vortex component of the dipole manages to cross the step ($x = 0$). The other vortex reflects back and stays in the region $x < 0$ for all time. The vortex that manages to cross the step performs a loop under the influence of the contour wrapped around it, and eventually the two components of the dipole split and they drift away from each other. After encountering the topography, there is no dominant motion in the y-direction owing to self-propagation as there is for a dipole approaching the topography from the deep side (figures 6.7(a) and 6.7(b)) since the dipole is no longer a coherent structure.

6.4 Discussion

This chapter further explores the motion of vortices near large amplitude topography in a two-layer fluid. In chapters 3 and 4 single vortices in either layer were investigated and in chapter 5 an arrangement of two vortices, one in each layer (a heton) was considered. Here the motion of dipoles (two vortices in the same layer) has been studied. As with hetons, dipoles are self-propagating and therefore also provide a mechanism for vortices to approach and interact with the step. Indeed, it has been shown that as lower-layer dipoles approach the topography, they split under the influence of their image and their subsequent behaviour is exactly as the single lower-layer point vortices of chapter 4 which were just 'switched on'.

The motion of upper-layer dipoles, crucially, depends on which direction they approach the topography from. A dipole approaching the topography from the deep side of the step ($x_0 > 0$) will, on reaching the topography, tend to perform oscillations about the step change while propagating toward the

positive y-direction due to conservation of potential vorticity and the wrapping up of the contour. In contrast, a dipole approaching the topography from the shallow side ($x_0 < 0$) tends to wrap up the contour more quickly and each vortex component of the dipole becomes shielded from the other. The vortices then evolve as separate entities.

The behaviour of the upper-layer dipoles compares well to other studies, notably Nycander and Isichenko [1990] and Hesthaven et al. [1993] for the oscillating $x_0 > 0$ case. For dipoles with $x_0 < 0$, where shielding is the dominant mechanism, similar effects are described by Valcke and Verron [1997].

Chapter 7

Applications and conclusions

In this chapter some of the results of the previous chapters are briefly applied to the real ocean before conclusions to part I are presented.

Typical on-shelf velocities produced by this model using parameter values appropriate to the western boundary of the Gulf of Mexico are estimated. Depths change from about 500 m to 2500 m in a relatively short distance giving $\delta = 500/2500 = 0.2$. (The upper-layer contour dynamics experiments in chapter 4 used this value of δ.) For the Gulf of Mexico, $g' = 0.02\,\mathrm{m\,s^{-2}}$ (Gill 1982) and $f_0 = 6 \times 10^{-5}\,\mathrm{s^{-1}}$ giving $L_D = (g'H_1H_2/(H_1 + H_2))^{1/2}/f_0 \approx 50$ km.

A lower-layer eddy is chosen to situate at $L = 0.5 \approx 25$ km away from the step. Note that a typical value for the Rossby number is $Ro = 10^{-1}$ (and so quasi-geostrophic theory is a reasonable approximation), hence model speeds scale as $Rof_0L_D \approx 0.3\,\mathrm{m\,s^{-1}}$. In most of the model experiments, the size of the circulation is $|\Gamma| = 1$ giving single vortex propagation speeds, parallel to the topography, of $V \approx 0.05\,\mathrm{m\,s^{-1}}$. The velocity field measured at $x = -0.1 \approx$ 5 km from the shelf break as the lower-layer vortex propagates past (parallel to the topography) can be calculated. Initially small velocities are measured,

due to the transient waves. Later, larger velocities (≈ 1 cm s^{-1}) are generated as the vortex passes closest to the measuring station. These velocities are due to the steady localised image disturbance. Subsequently, regularly oscillating velocities (≈ 0.8 cm s^{-1}) are measured due to the topographic wave in the wake of the eddy. The numerical model gives maximum velocities of ≈ 1 cm s^{-1}. Thus, lower-layer vortices produce small velocities on the shelf. It is expected that upper-layer vortices will produce much more significant velocities, due to nonlinear interaction.

Loop Current Eddies in the Gulf of Mexico and their associated velocities may be described by this model. Loop Current Eddies initially propagate west across the Gulf owing to the β-effect whereupon they encounter steep continental shelf topography. Typically they then propagate parallel to the topography and radiate topographic waves much as is described in this part of the thesis. Loop Current Eddies are surface trapped vortices and, although linear theory doesn't necessarily apply well to upper-layer vortices, the upper-layer model of section 3.6 is used to estimate Loop Current Eddy intensities, i.e. the length scale, $L_D \approx 50$ km is of the same order as the radii of Loop Current Eddies and Γ could be chosen such that model eddies propagate at similar speeds to Loop Current Eddies (0.05 m s^{-1}) and produce typical surface currents (1-2 m s^{-1}). Then, nonlinear simulations using contour dynamics could be performed to model subsequent Loop Current Eddy motions and topographic wave generation. As figures 4.6 and 4.7 indicate, large mixing effects in the vicinity of the step will occur as Loop Current Eddies impinge upon shelf topography and that subsequent dipole formation may influence the evolution. Indeed, motion of a Loop Current Eddy similar to that shown in figures 4.2 and 4.6 (i.e. parallel to topography) has been observed by Kirwan et al. [1984a] and

to some extent in the numerical simulations of Sutyrin et al. [2003]. Further, Cooper et al. [1990] have observed Loop Current Eddies that generate currents so strong that equipment has been damaged and lost. This is of concern to the offshore oil industry who have begun to drill in regions affected by Loop Current Eddies and provides motivation for modeling and predicting the motion of Loop Current Eddies detailed in part II.

In conclusion, the motion of single point vortices, hetons and dipoles near large amplitude topography has been studied. A linear theory was developed to describe the interaction of lower-layer vortices with topography. These analytical results are in excellent agreement with numerical experiments when describing the motion of single lower-layer vortices and lower-layer dipoles. An important conclusion is that lower-layer vortices admit topographic waves in their wakes, depending on the sign of their circulation.

The numerical algorithm (contour dynamics) was used to further investigate the nonlinear cases involving vortices in the upper layer, including single upper-layer vortices, hetons and upper-layer dipoles. Single vortices in the upper layer either cross the step or are reflected through a dipole mechanism, again, depending on their sign. In general, hetons split apart and the component vortices subsequently evolve as if they are separate entities. Upper-layer dipoles exhibit different behaviour depending on the direction from which they approach the topography. They either oscillate over the step or (like the hetons) separate.

While these chapters have only considered point vortices, it is worth noting that in the one-and-a-half layer problem of vortex interaction with topography, Dunn et al. [2002] and Dunn [2002] found that the behaviour of point vortices often compares well to that of vortex patches (with constant vorticity). John-

son and McDonald [2004a,b] have also found excellent agreement between the behaviour of barotropic point vortices and vortex patches interacting with non-trivial boundaries such as islands and gaps. Provided that the boundary of a vortex patch does not deviate too far from circular, Johnson and McDonald [2004a,b] are able to explain this close behaviour using ideas based on the vortex Hamiltonian. However, Zavala Sansón and van Heijst [2000], Sutyrin et al. [2001] and Herbette et al. [2003] find that the shape of a vortex patch can be greatly distorted when passing over (rather than close to) topography. Thus, a vortex patch may produce significantly different results to the point vortex experiment of figure 4.7, in particular.

It would be of interest to extend the present study to include the effects of a finite width shelf in the single-layer region and compare the effects of a continuous topography. Notably, Wang [1992] investigates the behaviour of vortices near exponential type topography and finds that many features of the interaction carry over to the continuously varying case. Sutyrin et al. [2003] studied the collision of Loop Current Eddies onto the shelf in the western region of the Gulf of Mexico. In their two-layer shallow water numerical simulations they found that the behaviour of the Loop Current Eddy depended critically on the width of the shelf.

Similarly, it would be of interest to examine the behaviour of hetons made up of patches of vorticity and the effects of different topography, e.g. shelves and continuous topography. Hetons consisting of patches of vorticity might be expected to split as in the point vortex case, the lower-layer component evolving according to its image in the topography. However, the upper-layer component may exhibit significantly different behaviour owing to the fact that it could distort. Also, Chao and Shaw [2000] have numerically examined the

behaviour of heton like structures made up of patches of vorticity on linearly sloping topography. They find that each component of the heton is able to tear the other apart and that the slope enhances this fission. Similar 'tearing' of hetons consisting of vorticity patches might be observed near large amplitude topography like that considered in this study. Further study could also include that of hetons and dipoles approaching the topography at an oblique angle.

Part II

Modeling and predicting the motion of Loop Current Eddies in the Gulf of Mexico

Chapter 8

Introduction and review

One of the dominant semi-permanent features of the circulation in the Gulf of Mexico is the intense Loop Current system in the eastern Gulf. A strong persistent current flows into the Gulf through the Yucatan Strait as the Yucatan Current and exits through the Florida Strait as the Florida Current. The clockwise flow extending into the Gulf to join the two is known as the Loop Current, see figure 8.1. The Loop Current periodically intrudes northward into the eastern Gulf of Mexico. It is suspected that near the maximum northward penetration of the Loop Current an instability occurs and a Loop Current Eddy is shed. These Loop Current Eddies are major warm core features of approximately 150 km in diameter that rotate clockwise (anticyclonically). Figure 8.2 shows one such eddy recently shed from the Loop Current. The eddy can be clearly made out in the contours of sea surface height anomaly. The colours indicate the deviation in height from the mean sea surface level, red being a large positive deviation through to blue, being a large negative deviation. The Loop Current Eddy corresponds to the large positive sea surface height anomaly centred on 27°N, 89°W. Notice that there are many other features,

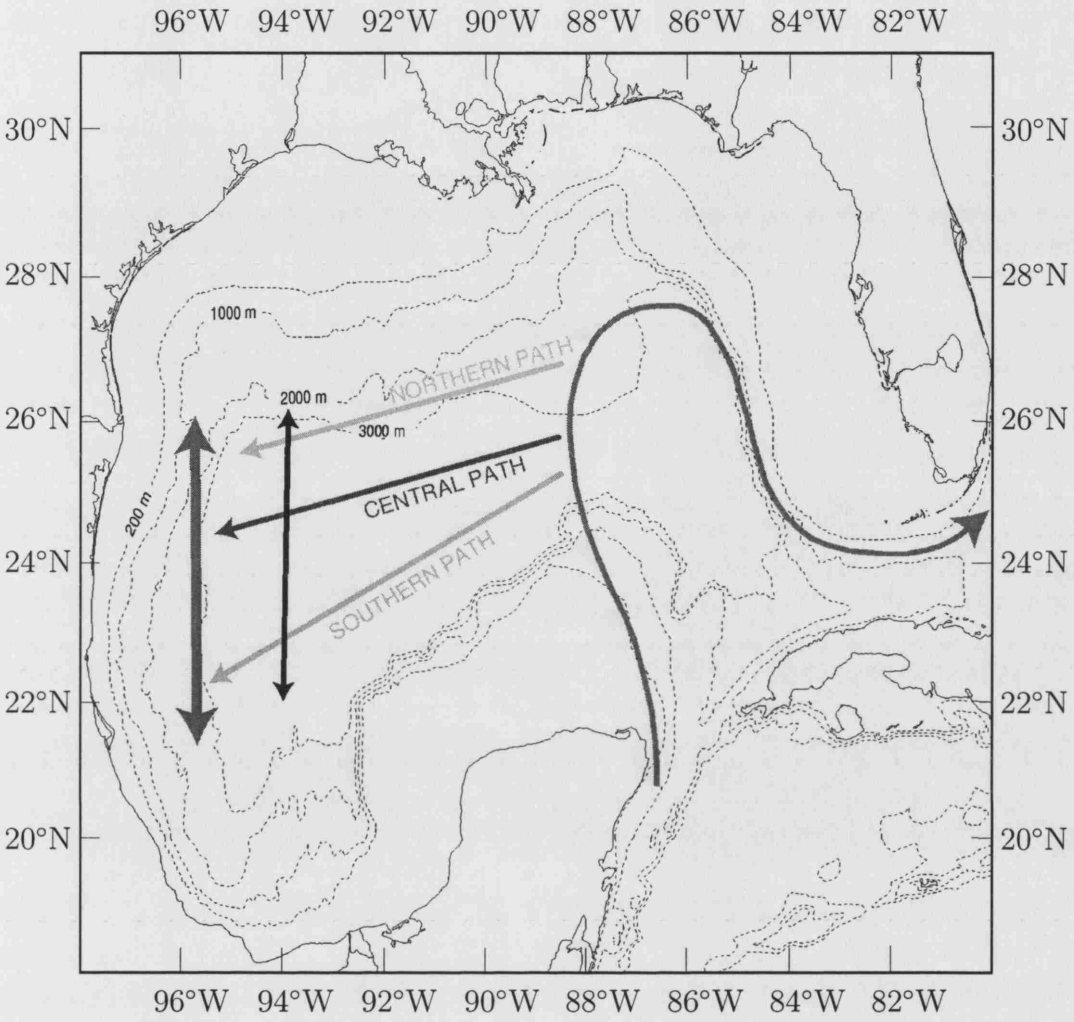

Figure 8.1: The Gulf of Mexico Loop Current and Loop Current Eddy paths (from Schmitz 2004).

both anticyclonic (e.g. older Loop Current Eddies) and cyclonic which may affect the motion and structure of Loop Current Eddies. The subsequent motion of a Loop Current Eddy is to follow a largely westward path across the Gulf until they hit the western boundary where they quickly dissipate through interaction with older Loop Current Eddies and the steep topography here (Kirwan et al. 1984a). It is vital to understand the paths that these Loop Current Eddies take as they transport vast quantities of salt, heat and mo-

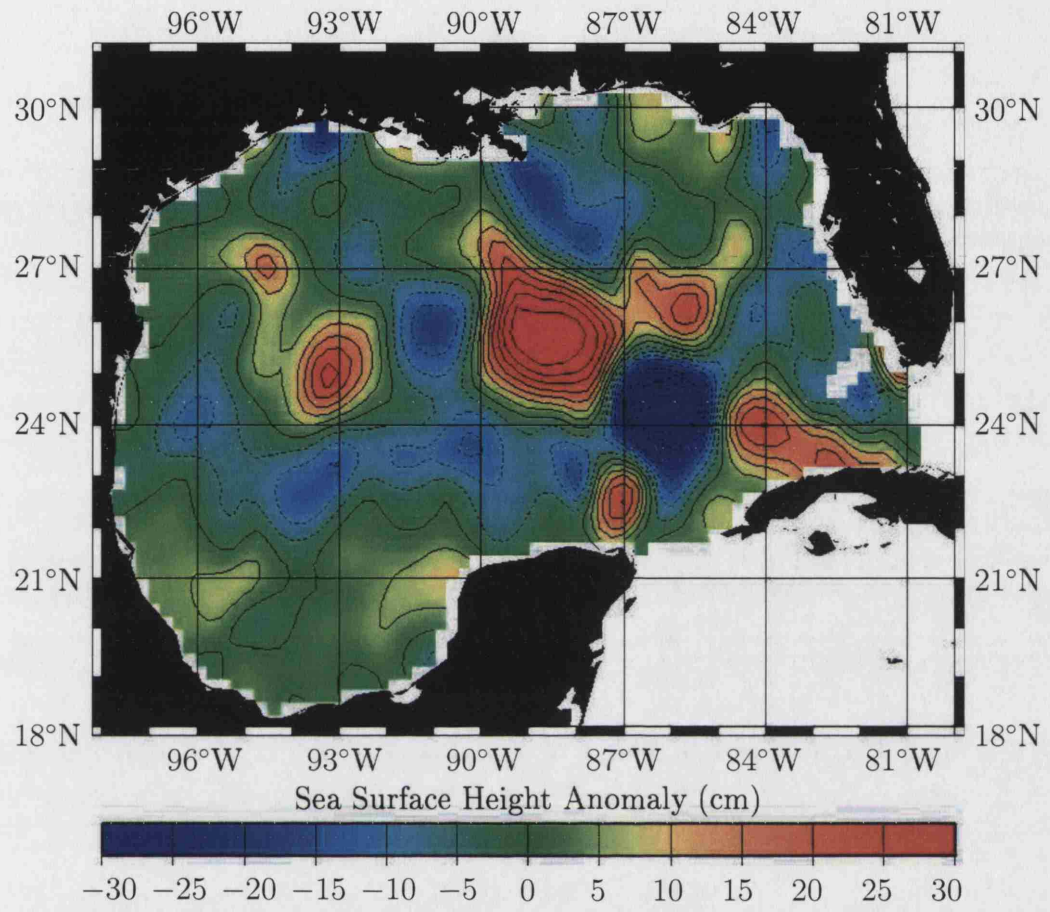

Figure 8.2: Sea surface height anomalies of a Loop Current Eddy. Picture reproduced from the Gulf of Mexico Near Real-Time Sea Surface Height Data Viewer at the Colorado Center for Astrodynamics Research, `http://e450.colorado.edu/realtime/gsfc_gom-real-time_ssh/`.

mentum across the Gulf into the western deep water region. Also, locally, Loop Current Eddies give rise to large velocities which may disrupt offshore oil operations. The Gulf of Mexico is a particularly oil rich region and oil companies have invested much time and money into examining the structure, paths and currents due to Loop Current Eddies[1]. This gives the motivation to develop a predictive model of Loop Current Eddies. The aim is to discover

[1]In fact, one such company is partly reponsible for sponsoring this thesis.

if it is possible to deduce the characteristics of a distant eddy from a set of velocities measured at a given fixed location (e.g. an offshore oil platform). Further, prediction of the subsequent motion of the eddy and behaviour of the eddy induced currents at the given location is attempted by incorporating the major features of Loop Current Eddies into a simple model.

There exists a large amount of literature concerning Loop Current Eddies and their associated currents and trajectories. Here, a brief overview of some of the present research is given. From these, the major features of Loop Current Eddies can be identified. Further, there have been previous attempts to model eddies (in particular, Gulf Stream Rings and Loop Current Eddies) and a comparison of some of the models used is also presented here.

Using a summary of historical data sets of hydrographic data, Elliott [1982] was the first to track (three) Loop Current Eddies to the western boundary of the Gulf of Mexico. Loop Current Eddy length scales (average radius of 183 km), life spans ($\approx$ 1 year) and westward translational velocities (2.1 km day^{-1} on average) are accurately quantified. Thus, Elliott [1982] is the first to document the large sizes of Loop Current Eddies and hence concludes that they must have a profound effect on the circulation of the Gulf of Mexico. Any account of the dynamics of the Gulf must, therefore, consider the effects of these rings.

Kirwan et al. [1984a] use satellite tracked drifters giving continuous data covering the movement and velocity characteristics of a Loop Current Eddy. Surface currents in excess of 50 cm s^{-1}, then the strongest measured to date, were observed.

As technology advanced, different and more accurate methods of observing eddies were developed. Vukovich and Crissman [1986] use continuous satellite

infrared data to derive characteristics of Loop Current Eddies. They compare the three westerly paths (figure 8.1) that Loop Current Eddies (observed to have diameters of 300-400 km) take across the Gulf. Temperature sections (deep water isotherms) show that significant currents due to Loop Current Eddies occur up to 800 m in depth. Furthermore they find that the eddy translation velocity across the Gulf of Mexico has distinct 'sprints' ($8\,\mathrm{km\,day^{-1}}$) and 'stalls' ($4\,\mathrm{km\,day^{-1}}$). Recently, Hamilton et al. [1999], who summarise measurements and characteristics of many Loop Current Eddies recorded over an extensive period, attribute these stalls to the interaction with vigourous lower continental slope cyclones. Note, in the models of chapters 9 and 10, the translational velocities are assumed to be constant.

As in the present work, Cooper et al. [1990] were motivated by the offshore oil industry who began to drill in areas suspected to be affected by Loop Current Eddies. They measured currents exceeding $2\,\mathrm{m\,s^{-1}}$ which were strong enough to cause damage and loss of equipment. Forristall et al. [1992] extend the work of Cooper et al. [1990] by making further direct current measurements and are the first to observe the Loop Current to shed two eddies, essentially, at the same time.

A simple circular eddy model has been proposed by Flierl [1979] in which an upper layer of constant potential vorticity fluid overlies a stationary lower layer. The flows are not constricted to be quasi-geostrophic, thus the interface between the two layers is allowed to rise to the surface. Using potential vorticity arguments, it is found that the shapes of both warm core and cold core rings agree well with observations (of Gulf Stream Rings), although predicted velocities are too large. This, however, gives encouraging evidence that simple models, such as that developed in this part of the thesis, are useful in

describing oceanic rings such as Loop Current Eddies.

Cushman-Roisin et al. [1985] propose a time-dependent model of elliptical warm-core rings. As in Flierl [1979], a two-layer reduced-gravity model is used and the interface intersects the surface, i.e. warm eddies form lenslike structures embedded in a stationary ocean. The solution of the shallow water equations such that the depth is quadratic function of space and the velocity, a linear function, is chosen. This solution permits two forms for the time dependence. The first is a clockwise rotating, elliptical anticyclonic vortex of fixed shape. (This 'rodon' solution is similar to the present, though quasi-geostrophic, model proposed in chapter 10 and indeed some properties of the two will be compared.) The second is a pulsating circular eddy. Note also that Cushman-Roisin [1986] use frontal geostrophic dynamics to derive the rodon solution. Young [1986] also obtains the rodon solution and further examines the waves excited in the underlying fluid by size, shape and orientation variations.

Models with more direct application to observed oceanic eddies are developed by Kirwan et al. [1984b] and Glenn et al. [1990]. Kirwan et al. [1984b] develop a model such that characteristics of Loop Current Eddies can be inferred from drifter tracks. They achieve good correlation between model and measured values of translational velocities, eccentricities and current magnitudes. Thus, their study provides evidence that the similar present problem of deducing Loop Current Eddy characteristics from a time series of velocity data should also produce promising results. Glenn et al. [1990] derive a warm core ring feature model and apply it to Gulf Stream Ring data. The data is modeled by an elliptic paraboloid with linearly increasing swirl velocity. Best fit model parameters are deduced and used to interpret the life history of a ring. Similar least squares best fit techniques are used here to deduce model

parameters of Loop Current Eddies.

Thus, the major features of Loop Current Eddies that are incorporated into the present model are a westward translation of a circular or elliptical shaped eddy confined to the upper few hundred metres of the ocean in solid body or near solid body rotation. The westward motion of the Loop Current Eddies across the largely constant depth western Gulf of Mexico is due to the local planetary curvature or β-effect (i.e. β represents the effect of latitudinally varying Coriolis parameter). It is well known that in the absence of topography or advection by mean flow the internal dynamics of rings on a β-plane induce a translation velocity with a westward component (see McDonald 1999 for a review of this mechanism). Therefore, in the present model an eddy in near geostrophic balance is described by the displacement of the interface between the two layers of a one-and-a-half-layer fluid. In chapter 9 a simple circular model is assumed. Although oceanic rings are almost always observed to have an elliptical shape, the circular model has been shown to give a good first approximation (Warren 1967, Flierl 1979). The more complicated and realistic precessing, elliptic model is developed in chapter 10. The problem then is to construct expressions for the flow of fluid around this eddy. From these expressions the characteristics of the eddy (e.g. translational velocity, position) are derived using the model equations.

Chapter 9

Circular eddies

9.1 Introduction

In this chapter the equations by which the Gulf of Mexico is modeled are introduced. A circular eddy model is developed to simulate velocities generated by a Loop Current Eddy and the results are tested against both synthetically generated and actual data gathered in the Gulf.

This chapter is organised as follows. In the first section, the governing equations are stated and the model is formulated. The problem of determining the characteristics of this model from remotely measured data is examined in sections 9.3 and 9.4. The robustness of the model with respect to noise in the data is investigated in section 9.5, followed by application to actual Loop Current Eddy data in section 9.6. Finally, conclusions are presented in section 9.7.

9.2 The eddy model

The upper layers of the Gulf of Mexico in which Loop Current Eddies reside are assumed to be well approximated by a one-and-a-half-layer ocean model where an upper layer of fluid overlies a deep motionless lower layer. In the far-field, the non-dimensional equations governing the motion of an eddy in a reduced-gravity fluid on the β-plane are

$$\boldsymbol{u}'_t + (\boldsymbol{u}' \cdot \nabla)\,\boldsymbol{u}' + \boldsymbol{k}\left(1 + \hat{\beta} y\right) \times \boldsymbol{u}' = -\nabla \eta', \tag{9.1}$$

$$\eta'_t + \nabla \cdot [(1 + \eta')\,\boldsymbol{u}'] = 0, \tag{9.2}$$

where $\boldsymbol{u}' = u'\boldsymbol{e_x} + v'\boldsymbol{e_y}$ is the velocity field, and η' is the displacement of the interface between the two layers from the background depth of unity, see Pedlosky [1987]. Variables have been made non-dimensional using the inverse of the Coriolis parameter, f, as the time scale, and the deformation radius, $L = (g'H)^{1/2}/f$, as the length scale, where g' is the reduced gravity and H is the undisturbed layer depth. The non-dimensional parameter $\hat{\beta}$ is defined by $\hat{\beta} = \beta L/f$. These equations are identical to (2.3) and (2.4) stated in the introduction to part I. Hence the model used in this chapter (and chapter 10) is also quasi-geostrophic in the far-field, where $\boldsymbol{u}'$ is small, and the theory developed in chapter 2 is valid accordingly. Note that, in this and subsequent sections, it will be necessary to compare non-dimensional model parameters to real oceanographic data. In particular, the reduced gravity has a value of $g' = 0.02\,\mathrm{m\,s^{-2}}$, the Coriolis parameter, $f = 6 \times 10^{-5}\,\mathrm{s^{-1}}$ and $\beta = 2.3 \times 10^{-11}\,\mathrm{m^{-1}\,s^{-1}}$ at Gulf of Mexico latitudes. The undisturbed layer depth is $H = 300\,\mathrm{m}$. Hence, parameters are made dimensional by multiplying by the appropriate time scale, 0.2 days, length scale, 40 km, and speed scale, $2.5\,\mathrm{m\,s^{-1}}$.

Figure 9.1 shows a sketch of the proposed eddy model. Here r is the coordinate describing the radial distance of some measuring station, located at (x_{ms}, y_{ms}), from the centre of the propagating eddy (x_i, y_i), at time t_i, i.e.

$$r^2 = (x_{ms} - x_i(t_i))^2 + (y_{ms} - y_i(t_i))^2 . \tag{9.3}$$

The other parameters are U, the (westward) eddy translational velocity and η_0, the maximum displacement of the interface between the two fluid layers, which occurs at the centre of the eddy. This displacement can be regarded as the maximum depth of the eddy or equivalently the depth beyond which the eddy has no significant velocity signature. Note that the effects of β are not explicitly included but, rather, are implicit in that a constant westward translational velocity is imposed.

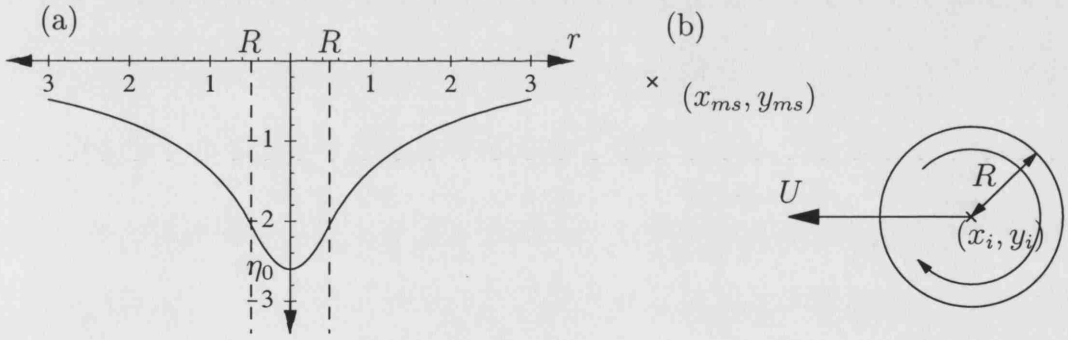

Figure 9.1: The eddy model parameters at time t_i. (a) Side view showing a typical deformation of the interface between the two fluid layers which has a maximum, η_0, at the eddy centre (x_i, y_i). (b) Top view, where the (fixed) measuring station located at (x_{ms}, y_{ms}) is also indicated.

In the interior region of the eddy, $0 < r < R$, velocities are assumed to be $O(1)$, as are interface displacements and quasi-geostrophic theory no longer applies. Therefore an appropriate interior solution, valid for $0 < r < R$, is to

be developed. This interior solution is based on observations of Loop Current Eddies and is matched to the far-field, quasi-geostrophic solution across $r = R$.

The eddy is assumed to translate solely in the westward direction (Elliott 1982). Implicit in this is the neglect of any mean flow and eddy-eddy interaction, i.e. the eddy is truly isolated and propagates due to the β-effect only. Also, for anticyclones (such as Loop Current Eddies), the translational speed, U', is always greater in magnitude than the long Rossby wave speed so that Rossby waves are not radiated (Cushman-Roisin et al. 1990). As in McDonald [1998a] this condition is satisfied if $U' < -\hat{\beta}$ and shallow water anticyclones like the present model eddy are considered to be steady.

The shallow water equations (9.1) and (9.2) are expanded in the small non-dimensional parameter $\hat{\beta}$. (Note, for Gulf of Mexico latitudes $\hat{\beta}$ is indeed small, i.e. $\hat{\beta} \approx 0.015$.) The appropriate expansion is to let $\boldsymbol{u'} = \hat{\beta}\boldsymbol{u} + \hat{\beta}^2\boldsymbol{u_2} + \cdots$, $U' = \hat{\beta}U + \hat{\beta}^2U_2 + \cdots$ and $\eta' = \hat{\beta}\psi + \hat{\beta}^2\psi_2 + \cdots$, where ψ is the geostrophic streamfunction (McDonald 1998a, Benilov 1996). In a frame of reference moving steadily with the eddy at velocity $\hat{\beta}U$, time derivatives in (9.1) and (9.2) can be replaced by $-\hat{\beta}U\partial/\partial x$. Hence, in component form, (9.1) and (9.2) become

$$\hat{\beta}(-Uu_x + uu_x + vu_y) + (\psi + \hat{\beta}\psi_2)_x = (1 + \hat{\beta}y)v + \hat{\beta}v_2, \tag{9.4}$$

$$\hat{\beta}(-Uv_x + uv_x + vv_y) + (\psi + \hat{\beta}\psi_2)_y = -(1 + \hat{\beta}y)u - \hat{\beta}u_2, \tag{9.5}$$

$$\hat{\beta}U\psi_x + \Big[(1 + \hat{\beta}\psi)u + \hat{\beta}u_2\Big]_x + \Big[(1 + \hat{\beta}\psi)v + \hat{\beta}v_2\Big]_y = 0, \tag{9.6}$$

where terms of $O(\hat{\beta}^2)$ have been neglected. Examining $O(1)$ terms gives the standard geostrophic equations,

$$\psi_x = v, \tag{9.7}$$

$$\psi_y = -u, \tag{9.8}$$

$$u_x + v_y = 0. \tag{9.9}$$

Examining $O(\hat{\beta})$ terms gives,

$$-Uu_x + uu_x + vu_y + \psi_{2,x} = yv + v_2, \tag{9.10}$$

$$-Uv_x + uv_x + vv_y + \psi_{2,y} = -yu - u_2, \tag{9.11}$$

$$-U\psi_x + \psi u_x + \psi_x u + u_{2,x} + \psi v_y + \psi_y v + v_{2,y} = 0. \tag{9.12}$$

Differentiating (9.11) with respect to x and (9.10) with respect to y and subtracting yields,

$$U(u_{xy} - v_{xx}) - uu_{xy} + uv_{xx} - vu_{yy} + vv_{xy} = -v - u_{2,x} - v_{2,y}, \tag{9.13}$$

after cancellation through substitution of equations (9.7)–(9.9). Now, using the geostrophic equations (9.7) and (9.8) again, note that

$$\nabla^2\psi \equiv \psi_{xx} + \psi_{yy} = v_x - u_y, \tag{9.14}$$

hence

$$-U(\nabla^2\psi)_x = Uu_{xy} - Uv_{xx}. \tag{9.15}$$

Similarly, the Jacobian may be written,

$$\begin{aligned} J(\psi, \nabla^2\psi) &\equiv \psi_x(\nabla^2\psi)_y - \psi_y(\nabla^2\psi)_x \\ &= v(v_x - u_y)_y + u(v_x - u_y)_x = vv_{xy} - vu_{yy} + uv_{xx} - uu_{xy}. \end{aligned} \tag{9.16}$$

Also equation (9.12) can be simplified using (9.7) and (9.8) to give,

$$-U\psi_x + u_{2,x} + v_{2,y} = 0. \tag{9.17}$$

Substituting (9.15), (9.16) and (9.17) into equation (9.13) gives,

$$U\psi_x - U(\nabla^2\psi)_x + J(\psi, \nabla^2\psi) + \psi_x = 0. \tag{9.18}$$

This equation can be written as

$$J\left[\psi + Uy, \nabla^2\psi + (U+1)y\right] = 0, \tag{9.19}$$

which has solution

$$\nabla^2\psi + (U+1)y = F(\psi + Uy), \tag{9.20}$$

where F is some arbitrary differentiable function. A mathematically convenient choice for F, for which (9.20) becomes homogeneous is $F(z) = (U+1)z/U$. In this case ψ satisfies the linear Helmholtz equation,

$$\nabla^2\psi - \frac{(U+1)}{U}\psi = 0. \tag{9.21}$$

As discussed previously, $O(\hat{\beta}^2)$ terms can be neglected and so the anticyclonic model eddy has a velocity, $U' = \hat{\beta}U < -\hat{\beta}$, i.e. $U < -1$. Thus it is valid to let $b^2 = (U+1)/U = (U'\hat{\beta}^{-1}+1)/U'\hat{\beta}^{-1}$ and the equation for the streamfunction ψ, (9.21), becomes

$$\nabla^2\psi - b^2\psi = 0. \tag{9.22}$$

This then gives the form of the streamfunction for the flow in the far-field of the eddy, i.e. sufficiently far from the eddy centre so that $|\boldsymbol{u}| = O(\hat{\beta})$ and $\eta = O(\hat{\beta})$. From expressions for the streamfunction it is possible to calculate fluid velocities in this region due to the model eddy. Demanding that the interface height anomaly vanish at infinity gives the boundary condition

$$\psi \to 0 \text{ as } r \to \infty. \tag{9.23}$$

The radially symmetric solution to (9.22) subject to (9.23) is

$$\psi = CK_0(br), \tag{9.24}$$

where K_0 is the zero'th order modified Bessel function. The value of the constant, C, is found by matching to the interior of the eddy at $r = R$

(see figure 9.1). Forristall et al. [1992] find that velocities near the centre of Loop Current Eddies are well described by simple solid body rotation models. (Note, similar solid body rotation models have been successfully applied to Gulf Stream Rings, see Joyce 1984.) In such geostrophic models the interior velocities are a linear function of the radial coordinate, r, and the interior streamfunction has a parabolic form. However, in the present model, the interior and exterior streamfunctions and velocities are required to match continuously across the radius $r = R$. In particular, the interior velocities won't match smoothly with those derived from the exterior solution, (9.24), if a parabolic profile is chosen for the interior streamfunction. Therefore, in the interior, the eddy interface (which can be regarded as a streamfunction) is chosen to have the form,

$$\eta = \eta_0 e^{-r^2}, \tag{9.25}$$

where η_0 is the unknown maximum depth of the interface between the two fluid layers. Implicit here is the assumption that the parameter associated with the decay length scale is unity. This assumption is made since it is undesirable to introduce another parameter into the problem and moreover, it is consistent with the (non-dimensional) eddy scale being unity. This Gaussian profile and the associated velocities will match continuously with the exterior solution, (9.24), across $r = R$ and further, in the limit $r \to 0$,

$$\eta \to \eta_0 \left(1 - r^2\right), \tag{9.26}$$

i.e. the streamfunction is parabolic. Therefore the interior streamfunction, (9.25), will produce velocities that at least tend to solid body rotation (in the limit $r \to 0$) like those observed in Loop Current Eddies by Forristall et al. [1992]. Note that $\eta_0 = O(1)$, and in the far-field $\psi = O(\hat{\beta})$, therefore the Bessel function solution for ψ (which does indeed grow large as $r \to 0$) is extended

back into the non-quasi-geostrophic region so that $\psi = O(1)$ when matching at $r = R$. Matching the streamfunctions and the tangential velocities across $r = R$ gives,

$$\psi|_{r=R} = CK_0(bR) = \eta_0 e^{-R^2} = \eta|_{r=R}, \tag{9.27}$$

$$v^+ = \left.\frac{\partial \psi}{\partial r}\right|_{r=R} = -CbK_1(bR) = -2R\eta_0 e^{-R^2} = \left.\frac{\partial \eta}{\partial r}\right|_{r=R} = v^-. \tag{9.28}$$

Equations (9.27) and (9.28) can be combined to give,

$$2RK_0(bR) = bK_1(bR). \tag{9.29}$$

Since $b = b(U)$, equation (9.29) can be rewritten,

$$g(R, U) = 0, \tag{9.30}$$

where $g \equiv 2RK_0(bR) - bK_1(bR)$. Therefore, given the translational velocity, U, the roots $g = 0$ determine the 'matching radius', R, where the eddy profile changes from Gaussian to a Bessel function structure. Due to the nature of equation (9.29), these roots must be found numerically. Figure 9.2 shows how the function g varies with the matching radius, R, for the following values of the translational velocities; (a) $U = -1.1$ (or $b \approx 0.3$), which, through multiplying by the dimensional speed scale derived at the beginning of this section, corresponds to $\approx 0.04\,\mathrm{m\,s^{-1}}$. Note that this is a realistic value for the translational velocity of a Loop Current Eddy (Vukovich and Crissman 1986); (b) $U = -2.5$ (or $b \approx 0.77$) that is $\approx 0.1\,\mathrm{m\,s^{-1}}$, an approximate lower bound for Loop Current Eddy translational velocities (Hamilton et al. 1999) and (c) $U \to -\infty$ (or $b \to 1$). Figure 9.2 suggests that faster eddies have larger matching radii, and are therefore, in a sense, 'bigger'. Note that since the translational velocity is constrained to lie in the range $-\infty < U < -1$, so $0 < b < 1$ and the matching radius, R, will be correspondingly bounded.

Solving (9.29) numerically it is found that $0 < R < 0.7709$. Note, the matching radii are found to be $R = 0.487$ and $R = 0.680$ for figures 9.2(a) and (b) respectively.

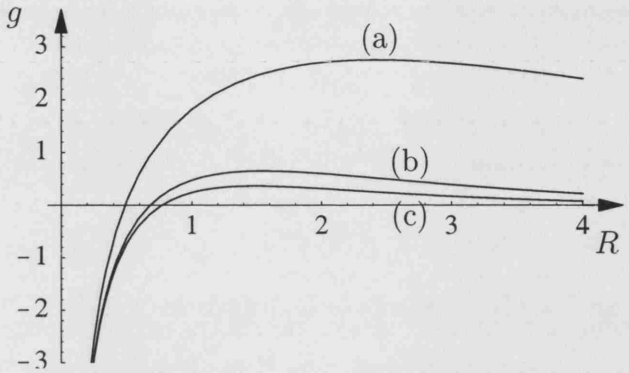

Figure 9.2: Plots of $g(R, U)$ as a function of R for (a) $U = -1.1$, (b) $U = -2.5$ and (c) $U \to -\infty$. The roots $g = 0$ determine the matching radius, R for the given value of U.

In summary, a circular model of a Loop Current Eddy satisfying the governing equations in the far-field and capable of producing $O(1)$ velocities in the interior has been developed. Thus, expressions for the streamfunction and velocities are given everywhere. Therefore it is now possible, in principal, to investigate whether, given a time series of remotely measured velocity data, the parameters of the model eddy can be determined and then used to predict the subsequent motion of the eddy and forecast the velocities it will produce. This task is tackled in the following sections.

9.3 The time series problem

A measuring station located at (x_{ms}, y_{ms}) will measure fluid velocities u and v in the x- and y-directions respectively due to the presence of an eddy centred

at (x_i, y_i). These velocities are obtained by differentiating (9.24) or (9.25) depending on the distance, r (equation (9.3)), between the measuring station and the eddy centre, i.e.,

$$u = \begin{cases} -\left.\dfrac{\partial \psi}{\partial y}\right|_{(x_{ms}, y_{ms})}, & \text{if } r > R, \\ -\left.\dfrac{\partial \eta}{\partial y}\right|_{(x_{ms}, y_{ms})}, & \text{if } r < R, \end{cases} \tag{9.31}$$

i.e.

$$u = \begin{cases} \dfrac{bC(y_{ms} - y_i) K_1\left(b\sqrt{(x_{ms} - x_i)^2 + (y_{ms} - y_i)^2}\right)}{\sqrt{(x_{ms} - x_i)^2 + (y_{ms} - y_i)^2}}, & \text{if } r > R, \\ 2\eta_0 (y_{ms} - y_i) e^{-\left((x_{ms} - x_i)^2 + (y_{ms} - y_i)^2\right)}, & \text{if } r < R, \end{cases} \tag{9.32}$$

and

$$v = \begin{cases} \left.\dfrac{\partial \psi}{\partial x}\right|_{(x_{ms}, y_{ms})}, & \text{if } r > R, \\ \left.\dfrac{\partial \eta}{\partial x}\right|_{(x_{ms}, y_{ms})}, & \text{if } r < R, \end{cases} \tag{9.33}$$

i.e.

$$v = \begin{cases} -\dfrac{bC(x_{ms} - x_i) K_1\left(b\sqrt{(x_{ms} - x_i)^2 + (y_{ms} - y_i)^2}\right)}{\sqrt{(x_{ms} - x_i)^2 + (y_{ms} - y_i)^2}}, & \text{if } r > R, \\ -2\eta_0 (x_{ms} - x_i) e^{-\left((x_{ms} - x_i)^2 + (y_{ms} - y_i)^2\right)}, & \text{if } r < R. \end{cases} \tag{9.34}$$

Plots of typical time series of u and v velocities measured at (x_{ms}, y_{ms}) as the eddy propagates by (given by equations (9.32) and (9.34)) are shown in figures 9.4(a) and (b). The parameter values used are $U = -1.1$, $(x_0, y_0) = (3, -0.2)$ and $C = 1$. The position of the eddy, relative to the measuring station, at selected times during the model evolution, which generated the velocities shown in figure 9.4, is also shown in figure 9.3. Figure 9.4 describes velocities measured at (x_{ms}, y_{ms}) (which is here and in all subsequent plots taken to be the origin, without loss of generality) due to an eddy which is

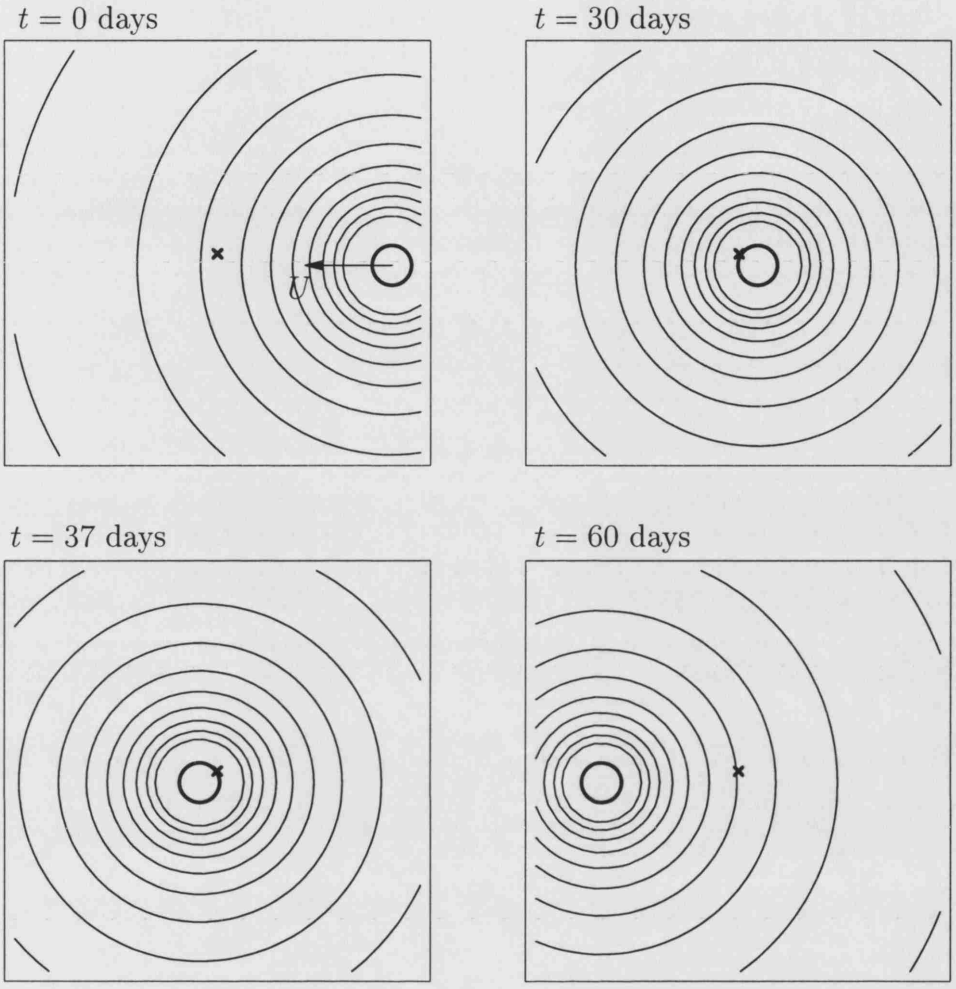

Figure 9.3: Time evolution of the model anticyclonic circular eddy and the associated outer streamfunction, ψ (equation (9.24)). The cross indicates the position of the measuring station, (x_{ms}, y_{ms}).

initially located in the far-field ($r > R$, corresponding to figure 9.3, $t = 0$ days), travels in a straight line, due westward, at a constant speed towards the measuring station, 'hits' it ($r < R$, figure 9.3, $30 < t < 37$ days), and continues on into the far-field (figure 9.3, $t = 60$ days). The plots in figure 9.4 have been made dimensional according to the scalings introduced in section 9.2. In this case, the velocity in the x-direction is always positive since the position of

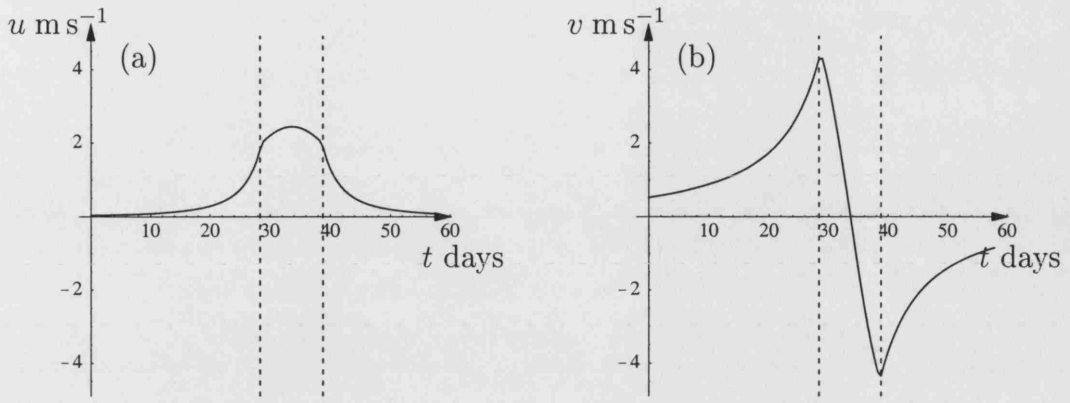

Figure 9.4: Typical velocity profiles of a model eddy passing through a measuring station, (a) u velocity and (b) v velocity. The dashed vertical lines represent the boundaries $r = R$ where the velocities switch from Bessel type to Gaussian, i.e. when the eddy radius $r = R$ hits the measuring station. The parameter values used to create these data are $U = -1.1$, $(x_0, y_0) = (3, -0.2)$ and $C = 1$.

the centre of the clockwise rotating eddy is always south of the measuring station, i.e. $y_i = -0.2 < 0 = y_{ms}$. This u velocity increases until $t = 34$ days at which point the eddy centre has the same longitude as the measuring station and is therefore at its closest proximity, thus producing maximum u velocities. Similarly, the velocity in the y-direction increases as the eddy approaches. Once the eddy hits the measuring station, the equations used to determine measured velocities change and equation (9.34) ($r < R$) requires the v velocities to decrease. When the eddy centre is at the same longitude as the measuring station, clearly (from (9.34)), the v velocity is zero. Once the eddy passes this point, v velocities become negative as such model anticyclonic eddies advect fluid to the east (west) of their centres so that the fluid velocity has a negative (positive) y-component. The velocities decrease as the eddy propagates away from the measuring station.

An application of this model is to predict the local velocities at a fixed point owing to the passage of a nearby Loop Current Eddy. A time series of velocities measured at the measuring station could be used to determine the eddy parameters U, (x_0, y_0) and C, and subsequently predict its motion. A particular case of interest involves the offshore oil industry in which prediction of currents at the measuring station is important in the day-to-day running of operations. In this case it would be useful to know if, on the basis of a limited data set, observed increasing local currents are due to an approaching eddy and if so, if and when the eddy passes closest to the measuring station causing maximal currents. Loop Current Eddies are capable of producing sufficiently large currents (e.g. 1–2 $\mathrm{m\,s^{-1}}$, Kirwan et al. 1984a, Cooper et al. 1990) to cause damage to risers. It is, therefore, desirable to have advanced warning of such events so that operations can be suspended averting danger to equipment and, potentially, the environment. It is hoped that the application of this model can provide such an early warning system.

Concentrating on this situation, the algorithm is developed assuming measured velocities used for prediction are only of the Bessel type given by equations (9.32) and (9.34) (otherwise the eddy centre has already passed closest to the measuring station and the largest currents have been recorded). This is the natural situation to consider as the eddy is initially in the 'far-field' with respect to the measuring station. Since the eddy is assumed to translate solely in the westward direction, the y-coordinate of the eddy centre remains constant, i.e. $y_i = y_0$ and the x-coordinates are given by $x_i = x_0 + Ut_i$. Therefore, given a set of velocity measurements, a system of equations in the four unknowns, C, U, x_0 and y_0 can be constructed. For example, suppose the velocities (u_i, v_i) are measured at time $t = t_i$, then equations (9.32) and (9.34)

yield

$$\frac{bC(y_{ms}-y_0)K_1\left(b\sqrt{(x_{ms}-x_0-Ut_i)^2+(y_{ms}-y_0)^2}\right)}{\sqrt{(x_{ms}-x_0-Ut_i)^2+(y_{ms}-y_0)^2}}-u_i=0, \tag{9.35}$$

$$-\frac{bC(x_{ms}-x_0-Ut_i)K_1\left(b\sqrt{(x_{ms}-x_0-Ut_i)^2+(y_{ms}-y_0)^2}\right)}{\sqrt{(x_{ms}-x_0-Ut_i)^2+(y_{ms}-y_0)^2}}-v_i=0. \tag{9.36}$$

Recall that $b = b(U)$. Equations (9.35) and (9.36) can be solved for the westward eddy translational velocity, U, the location of the eddy centre at time $t_0 = 0$, (x_0, y_0) and the constant C. Then, using the assumption that the eddy moves westward only at the constant speed U, the eddy position can be predicted for all time.

Equations (9.35) and (9.36) can be simplified even further. Dividing (9.36) by (9.35) gives

$$\frac{x_{ms}-x_0-Ut_i}{y_{ms}-y_0}=-\frac{v_i}{u_i}, \tag{9.37}$$

for any time t_i. Evaluating (9.37) at the times t_i and t_j, $i \neq j$ gives two equations between which the unknown x_0 can be eliminated giving,

$$y_{ms}-y_0=\frac{U\left(t_j-t_i\right)u_iu_j}{u_iv_j-v_iu_j}, \tag{9.38}$$

which, in turn, implies (from (9.37)) that

$$x_{ms}-x_0=-\frac{v_i}{u_i}\frac{U\left(t_j-t_i\right)u_iu_j}{u_iv_j-v_iu_j}+Ut_i. \tag{9.39}$$

Note that an explicit equation for the parameter C can be easily deduced from, say, (9.35), i.e.

$$C=\frac{u_i\sqrt{(x_{ms}-x_0-Ut_i)^2+(y_{ms}-y_0)^2}}{b(y_{ms}-y_0)K_1\left(b\sqrt{(x_{ms}-x_0-Ut_i)^2+(y_{ms}-y_0)^2}\right)}, \tag{9.40}$$

which can be restated in terms of the translational velocity only, by substituting (9.38) and (9.39),

$$C = \frac{\sqrt{u_i^2 + v_i^2}}{bK_1\left(b\sqrt{\left(\frac{U(t_j - t_i)u_j}{u_i v_j - v_i u_j}\right)^2 (u_i^2 + v_i^2)}\right)}. \tag{9.41}$$

Substituting this equation for C into (9.35) evaluated at the time t_j together with equations (9.38) and (9.39), gives one equation for the unknown translational velocity, U,

$$\begin{aligned} &\text{sgn}\,(u_i)\sqrt{u_i^2 + v_i^2}K_1\left(b\sqrt{\left(\frac{U\,(t_j - t_i)\,u_i}{u_i v_j - v_i u_j}\right)^2 (u_j^2 + v_j^2)}\right) \\ &-\text{sgn}\,(u_j)\sqrt{u_j^2 + v_j^2}K_1\left(b\sqrt{\left(\frac{U\,(t_j - t_i)\,u_j}{u_i v_j - v_i u_j}\right)^2 (u_i^2 + v_i^2)}\right) = 0. \end{aligned} \tag{9.42}$$

Equation (9.42) needs to be solved numerically due to the fact that the unknown appears in the argument of the Bessel function, K_1. A least squares approximation is used, the method of which is outlined in the following section. Let $F_{i,j}(U)$ represent the left-hand side of (9.42). Some plots of the function $F_{i,j}(U)$ for three different values of i,j (i.e. three different pairs of velocities) are shown in figure 9.5. The solid, short-dashed and dashed lines correspond to each different i,j pair. The data used to plot the typical velocity profiles shown in figure 9.4 has here been used to create figure 9.5(a). In this case the solution of (9.42) is $U = -1.1$ for all i, j. This is to be expected since, in each case, the velocities (u_i, v_i) and (u_j, v_j) were calculated from (9.32) and (9.34) using this value ($U = -1.1$) for the translational velocity. If, however, the velocity data is noisy, as in figure 9.5(b), the solutions for U vary and indeed may not have roots within a reasonable range (dashed line). Noise and the consequent effects on the eddy model are discussed in section 9.5.

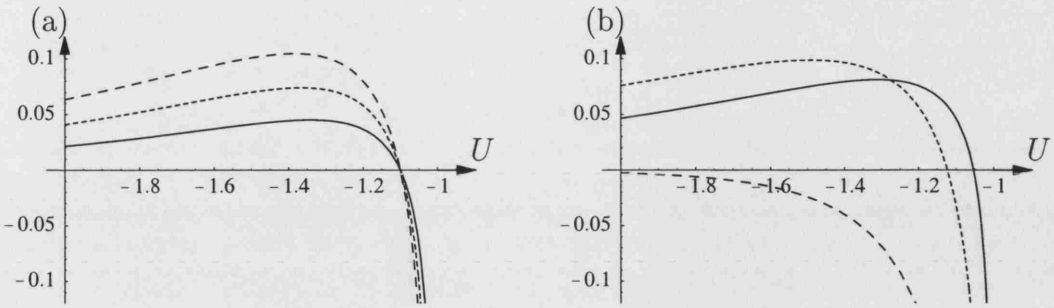

Figure 9.5: Typical plots of the function $F_{i,j}(U)$, defined by equation (9.42) for (a) synthetic data and (b) noisy data. The solid, short-dashed and dashed lines correspond to each different i,j pair.

9.4 Least squares solution

The method of least squares is particularly suitable for solving equation (9.42) for the translational velocity since the measuring station will record velocities continuously building up a time series of velocity data. Suppose the measuring station records n velocities, (u_i, v_i), at times t_i, $i = 0, \ldots, n-1$. Let $\boldsymbol{u_{i,j}}$ represent the pair of velocities (u_i, v_i) and (u_j, v_j), $i \neq j$. Then, any velocity pair, $\boldsymbol{u_{i,j}}$, may be substituted into (9.42) in order to solve for U. However, the velocities measured will not, in general, be exactly described by the proposed model due to assumptions made in formulating the eddy model and 'noise' in the actual measurements. Therefore it is better to calculate an 'average' translational velocity from solving (9.42) using all possible velocity pairs from the time series.

Essentially this is what the least squares method does. It solves a system having more equations than unknown variables and for this reason is appropriate for solving (9.42). Since there are more equations than variables, the solution will not be exactly correct for each equation, rather the process minimises the square of the difference between the model solution and the observed

values (Press et al. 1992). The equations are nonlinear therefore an initial guess (or guesses) at the unknown is required. Note that, in this system, there are C_2^n equations (since $i \neq j$ and $F_{i,j}(U) = F_{j,i}(U)$) and just the one unknown, U.

Let $k_{i,j}$ represent the right-hand side of (9.42). Further, let $\boldsymbol{K}$ be the residual vector (the difference between $k_{i,j}$ and equation (9.42) calculated using the estimate for the sought parameter, $F_{i,j}(U)$), i.e.

$$\boldsymbol{K} = [k_{0,1} - F_{0,1}(U), \ldots, k_{n-2,n-1} - F_{n-2,n-1}(U)]\,. \tag{9.43}$$

In this model $k_{i,j} \equiv 0$ for all i, j and the residual is,

$$\boldsymbol{K} = [-F_{0,1}(U), \ldots, -F_{n-2,n-1}(U)]\,. \tag{9.44}$$

Next seek, in turn, a value of U such that the square of each component of $\boldsymbol{K}$ is a minimum. A method of steepest descent is used in which an initial guess at the translational velocity, U, is required (see, for example, Press et al. 1992). This is a numerical procedure as opposed to an analytical method of steepest descent. An initial estimate is specified, and the method tries to get progressively more accurate approximations to a minimum. To improve computational efficiency upper and lower bounds on the translational velocity are given and the search for a minimum is stopped if the approximation ever falls outside this range. The result is guaranteed to correspond to at least a local minimum of the function (the square of each component of $\boldsymbol{K}$) in that range. However, it is important to understand that the result may not be the global minimum point. Analogously, the function can be though of as defining the height of a surface. The method essentially starts at the point specified, then follows the path of steepest descent (using derivatives) on the surface. Except in pathological cases, this path always leads to at least a local

minimum of the function on the surface.

In this way the value of U which minimises the square of the difference between the model solution and the $k_{i,j}$ for each equation is found. An average of these translational velocities is then taken to obtain the final value for U.

This algorithm is tested using synthetic data generated from equations (9.32) and (9.34). Choosing the parameters $C = 1$, $U = -1.1$ and $(x_0, y_0) = (3, -0.2)$, a velocity time series may be generated by evaluating (9.32) and (9.34). It is decided to record, say, $n = 101$ velocities measured at times $t_i = t_0 + idt$, $i = 0, \ldots, n-1$, where $t_0 = 0$ and $dt = 3$ (again, with the presumption that the measuring station, (x_{ms}, y_{ms}), is located at the origin). Now, assume the parameters C, U and (x_0, y_0) are unknown. The following demonstrates that it is possible to deduce these parameters from the given time series.

An initial guess (and range) for the translational velocity, U is required. As argued in section 9.2, shallow water anticyclones have $|U|$ large enough so that Rossby waves are not radiated, i.e. $U < -1$. Hence -1 is an upper bound for the parameter U and $U = -1 - \delta$, where $0 < \delta \ll 1$, is a natural initial guess for U. Indeed, it can be seen from figure 9.5 that there is an asymptote in the functions $F_{i,j}$ (the square of which are being minimised to find U), at $U = -1$. The (most suitable) minimising routine employed (the method of steepest descent) requires a range for the parameter U. Therefore a lower bound for U is also required. This is deduced from historical data, i.e. the translational velocity of a Loop Current Eddy is never likely to exceed $\approx 0.1\,\mathrm{m\,s^{-1}}$ (see chapter 1, Hamilton et al. 1999 and the text accompanying figure 9.2), in non-dimensional units this corresponds to $U \approx -2.5$ being a suitable lower bound. Thus, the routine searches for the minimum in the

range $-2.5 < U < -1$ with $U = -1 - \delta$ as the initial guess.

For the synthetic data, the residual vector, $\boldsymbol{K}$, is calculated according to (9.44), squared and the minimum is found to be at $U = -1.1$ for every velocity pair (as expected, see figure 9.5(a)). Therefore, the mean translational velocity gives the correct value, $U = -1.1$, used to generate the original velocity time series. It remains to deduce the other three parameters C and (x_0, y_0). Given a velocity pair, $\boldsymbol{u}_{i,j}$, they can be easily calculated using equations (9.38), (9.39) and (9.41). However, it is undesirable to use just one velocity pair to calculate these parameters since, when noise is introduced, certain velocity pairs may give inaccurate values. It is better then to employ the least squares method again on each of the equations (9.38), (9.39) and (9.41). However, since equations (9.38), (9.39) and (9.41) are linear in the unknown variables x_0, y_0 and C, respectively, and there is only one unknown per equation, the least squares method reduces to taking an average of the observations. This method does indeed yield the remaining parameters, $C = 1$ and $(x_0, y_0) = (3, -0.2)$ for the synthetic test data, exactly, as required.

In the next section the effects of noise on the data are examined. It can be seen from figure 9.5(b) that some measured velocity pairs can be so 'noisy' such that equation (9.42) doesn't have a root in the prescribed range. In this case the minimum found will just be the lower bound. Such velocity pairs will be discarded as they give unrealistic translational velocities and would skew the solution.

9.5 Measurement noise

Noise or deviation from the expected measurements is almost inevitable when analysing real data. This noise may be due to many different effects and take

a number of forms. For example, fluctuations due to some ubiquitous background signal, measuring inaccuracies and physical factors not described by the model (in the present work these could, for example, be tides, the presence of other eddies or topographic waves) are some ways in which noise may be produced, each of which may have a very different signature. Consequently, there are several different ways to model the effects of noise in a data set.

Measurement noise is usually taken to be independent at each time point. Whereas dynamical noise, arising from, for example, the aforementioned physical factors not described by the present model, will propagate in time in a much more complex fashion. In the interests of simplicity, time independent measurement noise is added to the model to test its robustness.

In this section, in an attempt to mimic real data, this measurement noise is simulated and the eddy model applied to the generated synthetic noisy data to see whether it still produces reasonable results. If the algorithm is successful the model can be confidently applied to real Loop Current Eddy data. The following equation is most appropriate for modeling measurement noise in the velocity measurements for this system,

$$\boldsymbol{u} = \boldsymbol{u_v} + \varepsilon \boldsymbol{u_n}, \tag{9.45}$$

where $\boldsymbol{u_v}$ is the measured velocity due solely to the eddy and $\boldsymbol{u_n}$ is a randomly generated velocity field representing the noise. The components of $\boldsymbol{u_n}$ are $O(1)$ and ε is a scale factor which determines the size of the noise relative to the eddy velocities. The velocities $\boldsymbol{u_v}$ are of $O(1)$ (see, for example, figure 9.4) and typically measurement noise will introduce inaccuracies of an order of magnitude less than the measured velocities (mathematically rigourous evidence supporting this statement can be found in Bevington and Robinson 2003). In this way a value for the scale factor ε can be estimated and synthetic data with high

frequency fluctuations due to measurement noise can be generated. Further, by restricting attention to $\varepsilon \ll 1$, only isolated eddies are being considered, i.e. the velocity field is due to a single eddy. If $\varepsilon = O(1)$, then two or more eddies could be contributing to the velocity field at the measuring station - this case is precluded.

Note that when noise is introduced it is possible for equation (9.42) to have no roots (see figure 9.5(b)). The algorithm is tested on noisy data generated by equation (9.45), where $\boldsymbol{u_v}$ is the synthetic data used in section 9.4 and figure 9.4 (recall the parameters used to create these data were $U = -1.1$, $(x_0, y_0) = (3, -0.2)$ and $C = 1$). The scale factor used is $\varepsilon = 0.1$ and figure 9.6 shows a typical velocity time series of noisy data generated using these parameters. Again the velocities are recorded at the discrete times $t_i = t_0 + idt$, $i =$

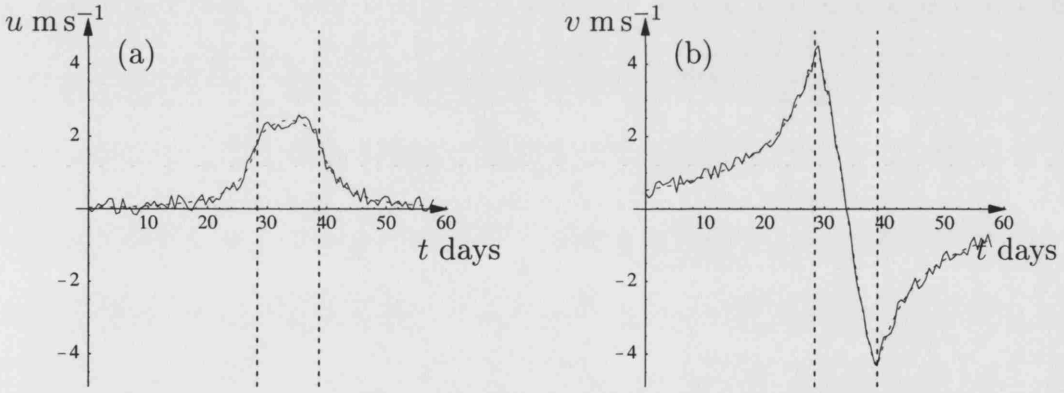

Figure 9.6: Noisy data generated by equation (9.45). The exact eddy velocities, $\boldsymbol{u_v}$, are represented by the short-dashed line, (a) u velocity and (b) v velocity. The dashed vertical lines represent the boundaries $r = R$ where the velocities switch from Bessel type to Gaussian.

$0, \ldots, n-1$ where $t_0 = 0$, $dt = 3$ and $n = 101$. In dimensional space $dt \approx 0.579$ days and therefore the time series runs over ≈ 60 days as shown in figure 9.6.

The ultimate aim is for the algorithm to calculate the governing parameters

of an approaching eddy and thus predict when the eddy passes closest to a measuring station, producing the largest velocities. Therefore it is assumed that the present time is $t_p = t_0 + pdt$ where, in this case, $p = 47$ and only velocities measured previous to this are known. The algorithm is run on the noisy data for $t_0 < t_i < t_p$ and only those velocity pairs for which roots for the translational velocity exist in the initial guess range for U are used. (The effects of varying the time, t_p, are investigated in section 9.6 where the algorithm is applied to the Loop Current Eddy data.) The parameters are found to be $U = -1.07605$, $C = 1.25188$ and $(x_0, y_0) = (2.9014, -0.185399)$. These are then used to forecast subsequent velocities due to the eddy using equations (9.32) and (9.34), assuming that the eddy translates solely in the westward direction. The results are shown in figure 9.7. The solid vertical line indicates the present time, t_p, which corresponds to $t \approx 27$ days in dimensional units. Notice that the maximum velocity of the whole time series occurs at $t_i > t_p$. The percentage

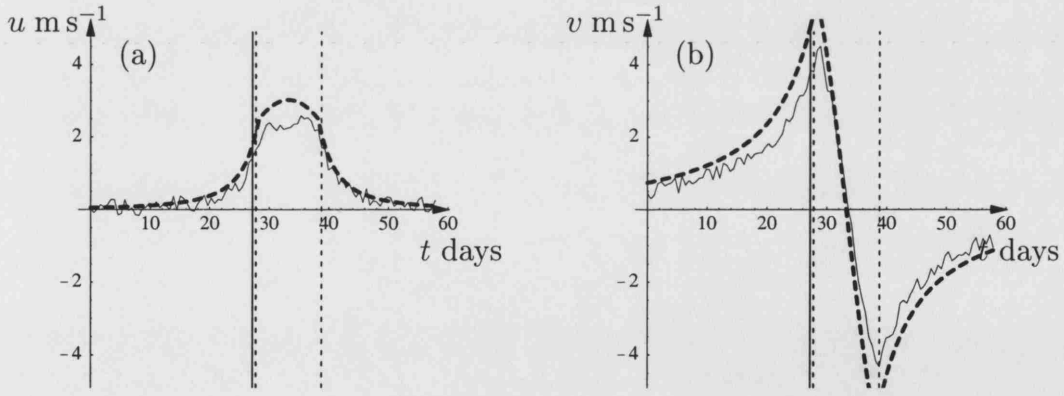

Figure 9.7: Predicted data generated by the algorithm (dashed). The original noisy data is given by the solid line, (a) u velocity and (b) v velocity. The dashed vertical lines represent the boundaries $r = R$ where the velocities switch from Bessel type to Gaussian. The solid vertical line represents the time t_p.

errors in using this algorithm to calculate the translational velocity, U, and the

initial position of the eddy centre, (x_0, y_0), are 2% and (3%, 7%) respectively. The percentage error in the estimation of the constant, C, is somewhat larger at 25%. However, this constant only affects the velocities in the outer solution and the error in C is also compensated for by the estimated magnitude of the translational velocity being smaller than the actual value. Therefore the predicted eddy data and the original noisy data agree qualitatively extremely well, e.g. the plots of the original synthetic noisy data and the predicted data (figure 9.7) follow the same trends and the times at which the maximum u and v velocities occur coincide. Quantitatively the results are also good. The predictions slightly overestimate the actual velocities but for the purposes of predicting velocities at, say, an offshore oil platform where operations must cease in the event of large currents, it is safer to over-predict velocities as under-prediction could result in environmental damage or even loss of life. These errors are very reasonable and it is concluded that this algorithm can be applied to noisy data which has fluctuations on the order of ε confidently. Note, further tests (again with $\varepsilon = 0.1$) using different randomly generated velocities, $\boldsymbol{u_n}$ (equation (9.45)), were conducted and similar agreements found. Thus, the circular eddy model is fairly robust and it is now more rigourously tested by applying it to real oceanic data which may be affected by more significant measurement inaccuracies, dynamical noise or other physical factors.

9.6 Application to Loop Current Eddies

In this section the effectiveness and stability of the algorithm is tested by applying it to real Loop Current Eddy data. A historical data set from the Gulf of Mexico containing several upper-layer high current events is considered. The data takes the form of a time series of velocities in the east-west and

north-south directions, which are identified as the x- and y-directions in this model respectively. These u (x-direction) and v (y-direction) velocity data are plotted in figure 9.8. (Gaps in these figures correspond to missing or invalid data.) Through comparison with sea surface height images it is concluded that the high current events correspond to the nearby passage of three Loop Current Eddies, (chronologically) denoted LCE1, LCE2 and LCE3 (figure 9.8). These data were kindly supplied by Fugro GEOS [2003] and were measured on behalf of BHP Billiton Petroleum (Americas) Inc.

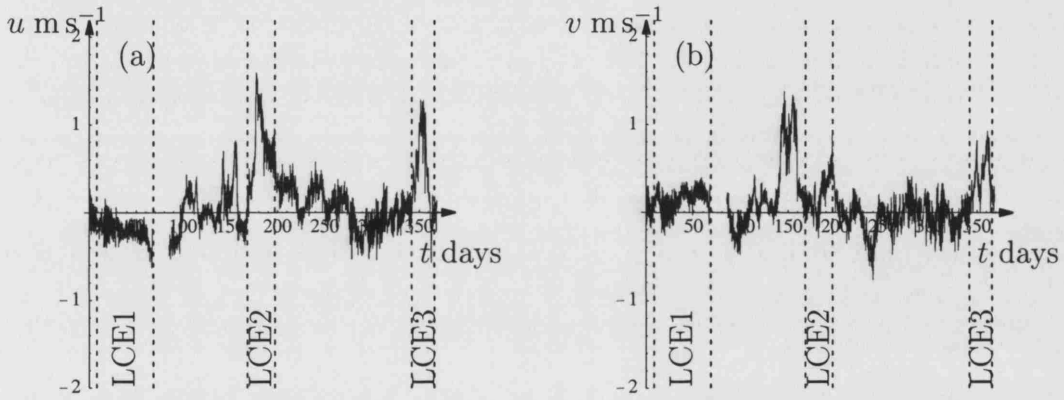

Figure 9.8: The historical data set, (a) u velocity and (b) v velocity. The dashed vertical lines represent the boundaries of the 'high current events'.

Although producing a significant enough signal to be classed a 'high current event' (according to definitions in Fugro GEOS 2003), LCE1 was relatively small and the velocities it generated were not large or distinct enough from the background flow to be well modeled by the present algorithm. The model was applied to the data corresponding to LCE2 and LCE3 with varying success. The velocity data was measured every 30 minutes. This gives a non-dimensional model time step length of $dt = 0.108$. In an effort to reduce computing time and smooth some of the high frequency noise, the data was 'filtered' by taking an average velocity over every 5 measurements. The

model was then applied to this new filtered data where $dt = 0.108 \times 5 = 0.54$, corresponding to 2.5 hours. (Compare this to the synthetic data generated in sections 9.3, 9.4 and 9.5 where velocities were measured every 0.579 days, i.e. there is significantly more data here.) The results are shown in figures 9.9 and 9.10.

The second Loop Current Eddy, LCE2 (figure 9.9), model parameters are found to be $U = -1.5323$, $C = 0.920756$ and $(x_0, y_0) = (0.788078, -1.35227)$. In dimensional units this corresponds to an eddy translating in the westward direction at $\approx 0.059\,\mathrm{m\,s^{-1}}$ ($\approx 5\,\mathrm{km\,day^{-1}}$). This is comparable to known eddy translational speeds which average $0.05\,\mathrm{m\,s^{-1}}$ ($\approx 4\,\mathrm{km\,day^{-1}}$, Vukovich and Crissman 1986, Hamilton et al. 1999). The model implies the eddy centre is initially located ≈ 32 km to the east and ≈ 55 km south of the measuring station. Further, the model predicts that the maximum depth at the eddy centre is $\eta_0 = 1.61456$. This implies that significant currents due to the eddy may be measured up to depths of $\eta_0 H \approx 480$ m. Again, this is consistent with observations, e.g. Vukovich and Crissman [1986] observe currents due to Loop Current Eddies at depths on the order of hundreds of metres.

The model predictions underestimate the magnitude of the velocities experienced at the measuring station in the x-direction (east-west). As stated in section 9.5, for operational reasons, under-prediction is undesirable. For instance, in the offshore oil industry, application of this model infers currents due to the approaching eddy, LCE2, will not be strong enough to require operations to be shut down whereas the currents actually measured are larger than predicted and could potentially cause damage to equipment in use. One reason for this under-estimation could be the large jump in velocity magnitude at $t = 6$ days. The model velocities are, by design, smoothly varying and

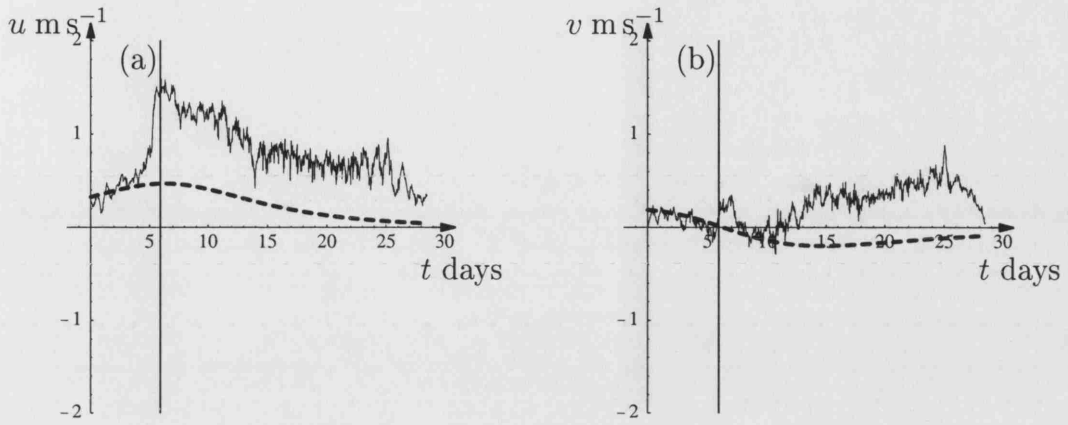

Figure 9.9: Predicted data for LCE2 generated by the algorithm (dashed). The original LCE2 data is given by the solid line, (a) u velocity and (b) v velocity. The solid vertical line represents the time t_p.

can not account for such discontinuities. The predicted velocities are therefore constrained to follow the general trend of the weak current data measured for times previous to the jump at $t = 6$ days. Nevertheless, the model accurately predicts the time period at which maximal velocities in the x-direction are experienced (t between 5 and 8 days). This would suggest that the eddy is closest to the measuring station at approximately 6 days after the time series begins. Further, the correlation between the data and the predictions for the north-south component is good. The model accurately predicts that the north-south velocities are zero at $t = 6$ days, reinforcing the conclusion that this is the time at which the eddy is closest to the measuring station (see also section 9.3 for an explanation of the shape of the velocity profiles). North-south velocities are well modeled up to $t = 12$ days, i.e. an accurate forecast for 6 days into the future. Beyond this the LCE2 velocity data has a positive y-component, possible reasons for which are discussed later. Further, note that the predicted value for the radius R is such that $R < y_0$, i.e. the predicted

path of the eddy does not pass sufficiently close to the measuring station as to generate velocities given by the interior solutions (equation (9.25)).

For the third Loop Current Eddy, LCE3 (figure 9.10), model parameters are found to be $U = -1.47104$, $(x_0, y_0) = (1.39973, -0.351354)$ and $C = 1.01673$. In dimensional units this corresponds to an eddy translating in the westward direction at $\approx 0.056\ \mathrm{m\,s^{-1}}$ ($\approx 5\ \mathrm{km\,day^{-1}}$). Again, this is comparable to known eddy translational speeds. The model implies the eddy centre is initially located ≈ 57 km to the east and ≈ 14 km south of the measuring station. Further, the model predicts that the maximum depth at the eddy centre is $\eta_0 = 1.83619$. This implies that significant currents due to the eddy may be measured up to depths of $\eta_0 H \approx 550$ m. Again, this value is consistent with observations.

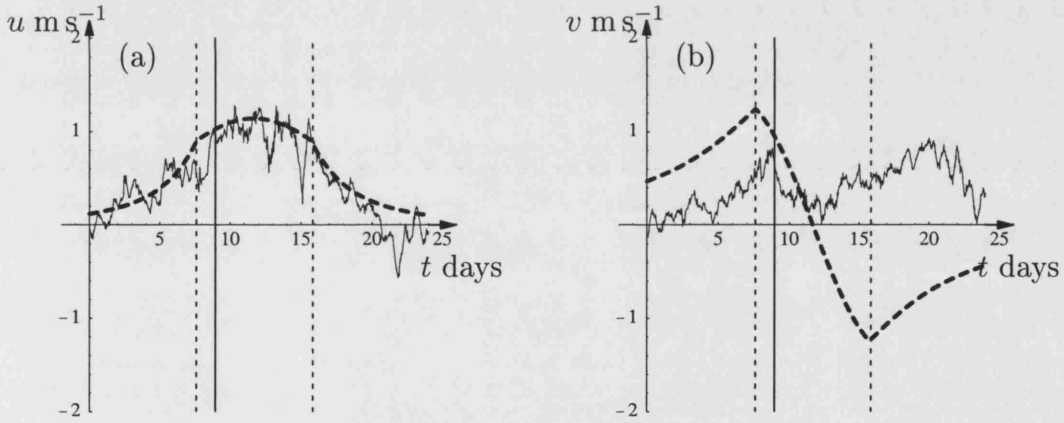

Figure 9.10: Predicted data for LCE3 generated by the algorithm (dashed). The original LCE3 data is given by the solid line, (a) u velocity and (b) v velocity. The dashed vertical lines represent the boundaries $r = R$ where the velocities switch from Bessel type to Gaussian. The solid vertical line represents the time t_p.

For this eddy the model gives a good prediction of the magnitude of the

velocities experienced at the measuring station in both the x- (east-west) and y- (north-south) directions and is more successful here than when applied to the LCE2 data. The correlation between the data and the predictions is especially good for the east-west component, see figure 9.10(a). The model accurately predicts the time period at which maximal velocities in the x-direction are experienced (t between 10 and 16 days). This would suggest that the eddy is closest to the measuring station at approximately 13 days after the time series begins.

The model accurately predicts (the slowly varying) changes in the direction of the u velocity for the whole time series and in the v velocity up to $t = 13$ days. However, beyond this time the data shows the v velocity to turn positive (north) again whereas the model has predicted that the eddy has passed the measuring station and, since it is anticyclonic, will produce velocities in the negative y-direction. A similar discrepancy also occurs in the LCE2 case and could be due to many factors. The most likely cause is that the eddy has deformed in such a way as to be no longer well modeled by a circle. Indeed, the eddy may have split and a second eddy may be producing the anomalous velocities in the y-direction. Evidence for such deformation is shown in figure 8.2 which depicts sea surface height anomalies in the Gulf of Mexico at the time of measurement of the LCE3 data. It clearly shows the Loop Current Eddy and a deformation at the northwestern edge. Further, there appears to be another eddy to the northeast. Both of these factors could affect measurements so as to cause anomalous velocities in the y-direction. It should be noted that a number of assumptions (in particular, that velocities are owing to a single eddy event) have been made, but despite this fact, the model represents the data (even for LCE2) remarkably well.

Graph	t_p (days)	$\|U\|$ ($\mathrm{m\,s^{-1}}$)	x_0 (km)	y_0 (km)	C
(a)	7.0	0.057	118.2	111.6	5.93880
(b)	7.5	0.056	80.7	50.9	1.80957
(c)	8.0	0.055	61.5	23.7	1.04958
(d)	8.5	0.056	58.2	16.1	1.02440
(e)	9.0	0.056	57.1	14.3	1.01673

Table 9.1: Model parameters corresponding to figure 9.11. The values shown for the initial position of the eddy centre, x_0 and y_0, are distances to the east and south of the measuring station respectively. Note, as t_p is increased, the westward translational speed, $|U|$, remains roughly constant while the eddy passes closer to the measuring station.

The predictions of the velocity profiles improve as more data is measured, as shown for the LCE3 case in figure 9.11. Here the time, t_p, is varied and the parameters are calculated using only 7 days worth of data in figure 9.11(a) through to 9 days worth in figure 9.11(e) (Note that figure 9.11(e) is the same as that shown in figure 9.10.). In each case the model gives a fairly consistent value of the translational velocity, see table 9.1. However, as more data is used so the model predicts the initial position of the eddy centre to be closer to the measuring station, i.e. $|x_0|$ and $|y_0|$ decrease as t_p increases (again see table 9.1). Therefore the time at which maximum u and v velocities are predicted tends to occur earlier as t_p is increased. Further, as the initial position of the centre of the eddy is predicted closer to the measuring station, so the predicted velocity profiles tend to the observed values, i.e. the forecasts improve.

9.7 Discussion

In this chapter a circular model of Loop Current Eddies in the Gulf of Mexico has been developed. This model satisfies the shallow water equations in the far-field but is also capable of generating $O(1)$ velocities when the eddy is close to a measuring station. The large velocity, interior solution is based on observations and consists of an eddy in near solid body rotation. Further, the exterior and interior solutions are matched so that streamfunctions and velocities are continuous. Implicit in the model is the fact that the eddy translates solely in the westward direction under the influence of the β-effect.

Given a time series of velocities measured at a remote point, a numerical method of least squares incorporating a steepest descent algorithm was developed to find the characteristics of the model eddy. First, a range for the translational velocity, U, (based on observations) is specified and the least squares equations minimised to find an accurate value for U. Next, the remaining characteristics of the model (its initial position and the constant, C) can be derived using similar techniques so that it is possible to predict subsequent velocities generated by the eddy. The model is also relatively stable to the addition of noise to the time series data.

The model has been applied to two data sets representing the passage of two Loop Current Eddies past a measuring station. The model predicts general trends in the velocity profile shape well. However, for the LCE2 data, the magnitude of the velocities are underestimated. This is owing to a sharp jump in the velocity data which the model fails to account for. The model is more successful in forecasting velocities from the LCE3 data. Velocity magnitudes are well predicted as are the times at which maximum velocities occur. Also, the translation speeds given by the model are comparable to those of observed

Loop Current Eddies. Further, it is shown that the forecast improves as more data is used.

The discrepancies between the model predictions and the actual data can be due to a number of factors. For example, deformation of the eddy, eddy-eddy interactions, background mean flows, tides and winds are all neglected by this simplified circular model. In the next chapter a more realistic model is developed. The restriction that the model eddy should be circular is relaxed and an elliptical model is used (e.g. Hamilton et al. 1999 observe elliptical Loop Current Eddies with a broad range of eccentricities). An improvement in the correlation between model predictions and the real data is expected.

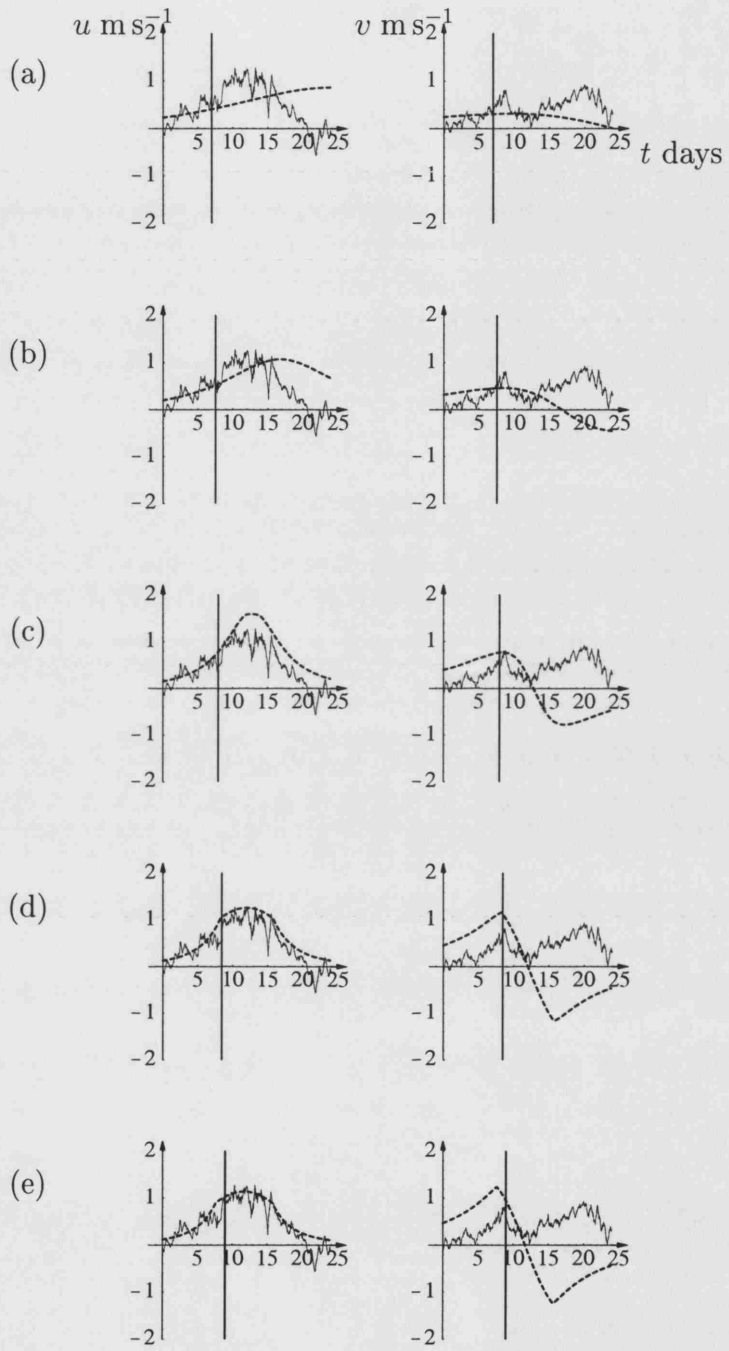

Figure 9.11: The algorithm prediction (dashed) improves as t_p increases. The original LCE3 data is given by the solid line and the solid vertical lines represent the time t_p where in (a) $t_p = 7$, (b) $t_p = 7.5$, (c) $t_p = 8$, (d) $t_p = 8.5$ and (e) $t_p = 9$.

Chapter 10

Elliptic eddies

10.1 Introduction

In this chapter the circular eddy model used to predict the motion of Loop Current Eddies in chapter 9 is generalised. Using the same governing equations a model of elliptic eddies is formulated. The resultant velocities produced at a given location due to a propagating (and precessing) elliptical eddy are compared with those of the circular model and are tested against Loop Current Eddy data gathered in the Gulf of Mexico. Note that the elliptical model (being more general) has more parameters to be determined than the circular model.

This chapter is organised as follows. In section 10.2, the governing equations derived in section 9.2 are solved for the streamfunction outside an ellipse. Various limiting cases of the solution are investigated. Section 10.3 introduces the form of the streamfunction used in the interior of the elliptic eddy model and in section 10.4 the exterior and interior solutions are matched at the ellipse boundary yielding a set of equations to be solved for the elliptic eddy model parameters. The problem of determining the characteristics of the elliptic model

from remotely measured data is examined in section 10.5. In section 10.6 the elliptical model is applied to actual Loop Current Eddy data and a comparison with the circular model results is detailed. Finally, conclusions are presented in section 10.7.

10.2 The outer solution

The initial shallow water equation analysis of chapter 9 can be similarly applied to elliptic eddies. However, in order to generalise the circle algorithm to predict the motion of elliptic eddies, the Helmholtz equation, (9.22), must now be solved outside an ellipse. Note that, as will be seen, the ellipse precesses, but for the moment the equations are solved in a frame in which the ellipse is stationary.

Transform to elliptic coordinates by writing

$$x + iy = \gamma \cosh(\xi + i\phi), \tag{10.1}$$

or, equating real and imaginary parts,

$$x = \gamma \cosh\xi \cos\phi \qquad \text{and} \qquad y = \gamma \sinh\xi \sin\phi, \tag{10.2}$$

where $(x, y) = (\pm\gamma, 0)$ are the common foci of the family of confocal ellipses (or hyperbolae) illustrated in figure 10.1. In these coordinates, the Helmholtz equation, (9.22), becomes

$$\frac{1}{\sinh^2\xi + \sin^2\phi}\left(\frac{\partial^2\psi}{\partial\xi^2} + \frac{\partial^2\psi}{\partial\phi^2}\right) - \gamma^2 b^2 \psi = 0. \tag{10.3}$$

Writing,

$$\psi(\xi, \phi) = \Xi(\xi)\Phi(\phi), \tag{10.4}$$

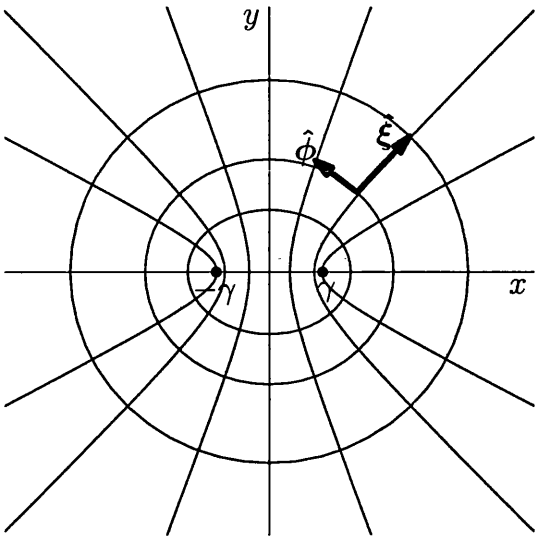

Figure 10.1: Elliptic coordinates. The common foci of the family of confocal ellipses, $(x, y) = (\pm\gamma, 0)$, are also shown.

and substituting into equation (10.3) yields

$$\left(\frac{1}{\Xi}\frac{d^2\Xi}{d\xi^2} - \gamma^2 b^2 \sinh^2\xi\right) + \left(\frac{1}{\Phi}\frac{d^2\Phi}{d\phi^2} - \gamma^2 b^2 \sin^2\phi\right) = 0. \tag{10.5}$$

This equation can be separated into,

$$\frac{1}{\Xi}\frac{d^2\Xi}{d\xi^2} - \gamma^2 b^2 \sinh^2\xi = c, \tag{10.6}$$

and

$$c + \frac{1}{\Phi}\frac{d^2\Phi}{d\phi^2} - \gamma^2 b^2 \sin^2\phi = 0, \tag{10.7}$$

or,

$$\frac{d^2\Xi}{d\xi^2} - (c + \gamma^2 b^2 \sinh^2\xi)\Xi = 0, \tag{10.8}$$

and

$$\frac{d^2\Phi}{d\phi^2} + (c - \gamma^2 b^2 \sin^2\phi)\Phi = 0, \tag{10.9}$$

where c is the separation constant. Rewriting using double angle formulae, equations (10.8) and (10.9) become

$$\frac{d^2\Xi}{d\xi^2} - (a + 2q\cosh(2\xi))\Xi = 0, \tag{10.10}$$

and

$$\frac{d^2\Phi}{d\phi^2} + (a + 2q\cos(2\phi))\Phi = 0, \tag{10.11}$$

where $a = c - (\gamma^2 b^2)/2$ and $q = \gamma^2 b^2/4$. These, respectively, are the modified Mathieu and Mathieu equations (McLachlan 1947) whose solutions are Mathieu functions. Note that, in this problem, the coefficient of q is positive. The solution for the exterior streamfunction, ψ, must be periodic in the angle ϕ. Therefore, the even and odd periodic solutions, namely, the even and odd Mathieu functions $\mathrm{ce}_n(\phi, -q)$ and $\mathrm{se}_n(\phi, -q)$, are chosen as the appropriate solutions to (10.11). Note that $\mathrm{ce}_n(\phi, -q)$ is 'even' in the sense that $\mathrm{ce}_n(-\phi, -q) = \mathrm{ce}_n(\phi, -q)$, similarly, $\mathrm{se}_n(-\phi, -q) = -\mathrm{se}_n(-\phi, -q)$ is 'odd'. It should be observed that non-periodic solutions to (10.11) also exist but are not required here.

The solution to (10.10) must decay as $\xi \to \infty$. Such solutions are the modified Mathieu functions of the third kind, denoted $\mathrm{Fek}_n(\xi, -q)$ and $\mathrm{Gek}_n(\xi, -q)$ (McLachlan 1947).

The numbers a and q must be related for the solutions ce_n, se_n, Fek_n and Gek_n to exist, i.e.

$$a = n^2 + \alpha_1 q + \alpha_2 q^2 + \ldots. \tag{10.12}$$

The values of the α_i are found by substituting (10.12) and the appropriate expansion of ce_n (or se_n) into (10.11) and equating coefficients of like powers of q. Thus the α_i depend on the order n of the periodic solution ce_n (or se_n). For a given q the value of a is found from (10.12) and is called the characteristic of the Mathieu function. It is denoted a_n or b_n according to whether it is even or odd, with the subscript used to identify it with the appropriate Mathieu function. Hence, the general solution for the streamfunction ψ comprises of the product of Mathieu functions and modified Mathieu functions of the third

kind for the same values of a and q.

Therefore only even terms corresponding to the even characteristics $a = a_n$ may be grouped together and odd terms corresponding to odd characteristics $a = b_n$ may be grouped together. Similarly, only products where the summation variables are equal are valid solutions, i.e.

$$\psi = \sum_{n=0}^{\infty} C_n \mathrm{Fek}_n(\xi, -q)\mathrm{ce}_n(\phi, -q) + \sum_{n=1}^{\infty} D_n \mathrm{Gek}_n(\xi, -q)\mathrm{se}_n(\phi, -q). \quad (10.13)$$

Equation (10.13) is, therefore, the general solution of the Helmholtz equation outside an ellipse which decays in the far-field. The constants C_n and D_n are found by appealing to the boundary conditions and this problem is considered in subsection 10.2.3. Before this, however, two known limits where $q \to 0$ are examined; *a*) the Laplacian limit where $q \to 0$ due to $b \to 0$, i.e. the Helmholtz equation reduces to Laplace's equation and *b*) the circle limit where $q \to 0$ due to $\gamma \to 0$, i.e. the solution of the Helmholtz equation as the foci approach the origin and the ellipse becomes a circle.

10.2.1 Laplacian limit, $b \to 0$

In letting $b \to 0$, which implies $q \to 0$, equation (9.22) becomes Laplace's equation and the solution (10.13) is expected to tend to the general Laplace solution, namely

$$\psi = \alpha\xi + A_0 + \sum_{n=1}^{\infty} e^{-n\xi} \left(A_n \cos(n\phi) + B_n \sin(n\phi)\right). \quad (10.14)$$

The $\mathrm{Fek}_n(\xi, -q)$ and $\mathrm{Gek}_n(\xi, -q)$ can be expanded in series of Bessel functions and $\mathrm{ce}_n(\phi, -q)$ and $\mathrm{se}_n(\phi, -q)$ can be expanded in series of trigonometric

functions (appendix A). Hence (10.13) can be rewritten,

$$\begin{aligned}
\psi = &\sum_{n=0}^{\infty} C_{2n} \sum_{r=0}^{\infty} A_{2r}^{(2n)} I_r(\sqrt{q}e^{-\xi}) K_r(\sqrt{q}e^{\xi}) \\
&\qquad \times (-1)^n \sum_{r=0}^{\infty} (-1)^r A_{2r}^{(2n)} \cos(2r\phi) \\
&+ \sum_{n=0}^{\infty} C_{2n+1} \sum_{r=0}^{\infty} B_{2r+1}^{(2n+1)} \left(I_r(\sqrt{q}e^{-\xi}) K_{r+1}(\sqrt{q}e^{\xi}) - I_{r+1}(\sqrt{q}e^{-\xi}) K_r(\sqrt{q}e^{\xi}) \right) \\
&\qquad \times (-1)^n \sum_{r=0}^{\infty} (-1)^r B_{2r+1}^{(2n+1)} \cos((2r+1)\phi) \\
&+ \sum_{n=0}^{\infty} \mathcal{D}_{2n+1} \sum_{r=0}^{\infty} A_{2r+1}^{(2n+1)} \left(I_r(\sqrt{q}e^{-\xi}) K_{r+1}(\sqrt{q}e^{\xi}) + I_{r+1}(\sqrt{q}e^{-\xi}) K_r(\sqrt{q}e^{\xi}) \right) \\
&\qquad \times (-1)^n \sum_{r=0}^{\infty} (-1)^r A_{2r+1}^{(2n+1)} \sin((2r+1)\phi) \\
&+ \sum_{n=0}^{\infty} \mathcal{D}_{2n+2} \sum_{r=0}^{\infty} B_{2r+2}^{(2n+2)} \left(I_r(\sqrt{q}e^{-\xi}) K_{r+2}(\sqrt{q}e^{\xi}) - I_{r+2}(\sqrt{q}e^{-\xi}) K_r(\sqrt{q}e^{\xi}) \right) \\
&\qquad \times (-1)^n \sum_{r=0}^{\infty} (-1)^r B_{2r+2}^{(2n+2)} \sin((2r+2)\phi), \quad (10.15)
\end{aligned}$$

where $A_r^{(n)}$ and $B_r^{(n)}$ are known constants relating to the Mathieu characteristics, a_n and b_n and depend on the value of q, i.e. the physical properties of the ellipse. Importantly, the restrictions $C_{2n} \propto \left(A_0^{(2n)}\right)^2$, $C_{2n+1} \propto q \left(B_1^{(2n+1)}\right)^2$, $D_{2n+1} \propto q \left(A_1^{(2n+1)}\right)^2$ and $D_{2n+2} \propto q^2 \left(A_2^{(2n+2)}\right)^2$ have been enforced in the definitions of $\mathcal{C}_n$ and $\mathcal{D}_n$, i.e.

$$C_{2n} = \frac{\mathcal{C}_{2n} \pi A_0^{(2n)}}{p'_{2n}}, \quad (10.16)$$

$$C_{2n+1} = \frac{\mathcal{C}_{2n+1} \pi B_1^{(2n+1)}}{s'_{2n+1}}, \quad (10.17)$$

$$D_{2n+1} = \frac{\mathcal{D}_{2n+1} \pi A_1^{(2n+1)}}{p'_{2n+1}}, \quad (10.18)$$

and

$$D_{2n+2} = \frac{\mathcal{D}_{2n+2} \pi B_2^{(2n+2)}}{s'_{2n+2}}, \quad (10.19)$$

where the p'_n and s'_n are also defined in appendix A. Now, from Abramowitz and Stegun [1964], in the limits $z_I, z_K \to 0$ and for r fixed,

$$I_r(z_I) \to \frac{\left(\frac{1}{2}z_I\right)^r}{\Gamma(r+1)}, \tag{10.20}$$

$$K_0(z_K) \to -\log z_K, \tag{10.21}$$

and

$$K_r(z_K) \to \frac{1}{2}\Gamma(r)\left(\frac{1}{2}z_K\right)^{-r} \qquad r > 0. \tag{10.22}$$

So, in the limit $q \to 0$, with $z_I = \sqrt{q}e^{-\xi}$ and $z_K = \sqrt{q}e^{\xi}$,

$$I_0(\sqrt{q}e^{-\xi})K_0(\sqrt{q}e^{\xi}) \to \log\left(\frac{1}{\sqrt{q}}\right) - \xi, \tag{10.23a}$$

$$I_r(\sqrt{q}e^{-\xi})K_r(\sqrt{q}e^{\xi}) \to \frac{1}{2}\frac{\Gamma(r)}{\Gamma(r+1)}e^{-2r\xi} \qquad r > 0, \tag{10.23b}$$

and

$$I_0(\sqrt{q}e^{-\xi})K_1(\sqrt{q}e^{\xi}) \pm I_1(\sqrt{q}e^{-\xi})K_0(\sqrt{q}e^{\xi}) \to \left(\frac{1}{\sqrt{q}} \pm \frac{\sqrt{q}}{2}\frac{1}{\Gamma(2)}\left(\log\left(\frac{1}{\sqrt{q}}\right) - \xi\right)\right)e^{-\xi}, \tag{10.24a}$$

$$I_r(\sqrt{q}e^{-\xi})K_{r+1}(\sqrt{q}e^{\xi}) \pm I_{r+1}(\sqrt{q}e^{-\xi})K_r(\sqrt{q}e^{\xi}) \to \left(\frac{1}{\sqrt{q}} \pm \frac{\sqrt{q}}{4}\frac{\Gamma(r)}{\Gamma(r+2)}\right)e^{-(2r+1)\xi} \qquad r > 0, \tag{10.24b}$$

and

$$I_0(\sqrt{q}e^{-\xi})K_2(\sqrt{q}e^{\xi}) - I_2(\sqrt{q}e^{-\xi})K_0(\sqrt{q}e^{\xi}) \to \left(\frac{2}{q}\Gamma(2) - \frac{q}{4}\frac{1}{\Gamma(3)}\left(\log\left(\frac{1}{\sqrt{q}}\right) - \xi\right)\right)e^{-2\xi}, \tag{10.25a}$$

$$I_r(\sqrt{q}e^{-\xi})K_{r+2}(\sqrt{q}e^{\xi}) - I_{r+2}(\sqrt{q}e^{-\xi})K_r(\sqrt{q}e^{\xi}) \to \left(\frac{2}{q}\frac{\Gamma(r+2)}{\Gamma(r+1)} - \frac{q}{8}\frac{\Gamma(r)}{\Gamma(r+3)}\right)e^{-(2r+2)\xi} \qquad r > 0. \tag{10.25b}$$

Note also that in the limit $q \to 0$ the constants relating to the Mathieu characteristics have the simple form,

$$A_r^{(n)} = B_r^{(n)} = \begin{cases} 0 & r \neq n, \\ 1 & r = n. \end{cases} \tag{10.26}$$

Finally, using all the above simplifications, in the limit $q \to 0$, (10.15) becomes

$$\begin{aligned} \psi = -\mathcal{C}_0\xi + \mathcal{C}_1 e^{-\xi}\cos(\phi) + \sum_{n=1}^{\infty} \mathcal{C}_{2n}\frac{1}{2}\frac{\Gamma(n)}{\Gamma(n+1)}e^{-2n\xi}\cos(2n\phi) \\ + \sum_{n=1}^{\infty} \mathcal{C}_{2n+1}e^{-(2n+1)\xi}\cos((2n+1)\phi) \\ + \mathcal{D}_1 e^{-\xi}\sin(\phi) + 2\Gamma(2)\mathcal{D}_2 e^{-2\xi}\sin(2\phi) + \sum_{n=1}^{\infty} \mathcal{D}_{2n+1}e^{-(2n+1)\xi}\sin((2n+1)\phi) \\ + \sum_{n=1}^{\infty} \mathcal{D}_{2n+2}\frac{2\Gamma(n+2)}{\Gamma(n+1)}e^{-(2n+2)\xi}\sin((2n+2)\phi). \end{aligned} \tag{10.27}$$

where, without loss of generality the constant $\log(1/q)$ term is ignored. This is precisely the required Laplacian solution, (10.14) where

$$\begin{gathered} \alpha = -\mathcal{C}_0, \\ A_0 = 0, \qquad A_1 = \mathcal{C}_1, \qquad A_{2n} = \mathcal{C}_{2n}\frac{1}{2}\frac{\Gamma(n)}{\Gamma(n+1)}, \qquad A_{2n+1} = \mathcal{C}_{2n+1}, \\ B_1 = \mathcal{D}_1, \qquad B_2 = 2\Gamma(2)\mathcal{D}_2, \\ B_{2n+1} = \mathcal{D}_{2n+1}, \qquad B_{2n+2} = \mathcal{D}_{2n+2}\frac{2\Gamma(n+2)}{\Gamma(n+1)}. \end{gathered} \tag{10.28}$$

10.2.2 Circle limit, $\gamma \to 0$

The solution for the streamfunction, ψ, is expected to tend to that of the Helmholtz equation outside a circle in the limit that the ellipse tends to a circle. Let $R_{\max}$ be the major axis length (of the ellipse), $R_{\min}$, the minor axis length and E, the eccentricity, where

$$E = \sqrt{1 - \frac{R_{\min}^2}{R_{\max}^2}}. \tag{10.29}$$

In the limit, $R_{\max} \to R_{\min}$, $E \to 0$ and the ellipse tends to a circle of radius $R_{\min}$. Since $\gamma = ER_{\max} = (R_{\max}^2 - R_{\min}^2)^{1/2}, \gamma \to 0$, and the foci tend to coalesce at the origin with the proviso that,

$$\gamma \cosh \xi \to \gamma \sinh \xi \to R_{\min}. \tag{10.30}$$

In this circle limit, $\xi \to +\infty$ which implies that $2q\cosh(2\xi) = 2q(e^{2\xi} - e^{-2\xi})/2 \to qe^{2\xi}$. Further, $a \to n^2$ for a function of integral order, n and the modified Mathieu equation, (10.10), degenerates to

$$\frac{d^2\Xi}{d\xi^2} - (n^2 + qe^{2\xi})\Xi = 0. \tag{10.31}$$

McLachlan [1947] details the above derivations more rigourously. Letting $R_{\min} = 1/2\gamma e^{\xi}$, equation (10.31) becomes the Bessel equation

$$\frac{d^2\Xi}{dR_{\min}^2} + \frac{1}{R_{\min}}\frac{d\Xi}{dR_{\min}} - \left(b^2 + \frac{n^2}{R_{\min}^2}\right) = 0, \tag{10.32}$$

where the relation $q = \gamma^2 b^2/4$ has been used. The solutions that are bounded as $R_{\min} \to \infty$ are required, i.e. $K_n(bR_{\min})$. Thus, by comparing these solutions to the (modified Mathieu function of the third kind) solutions of (10.10) in the limit $\gamma \to 0$ it can be deduced that

$$\mathrm{Fek}_{2n}(\xi, -q) \to \frac{p'_{2n}}{\pi} K_{2n}(bR_{\min}), \tag{10.33a}$$

$$\mathrm{Fek}_{2n+1}(\xi, -q) \to \frac{s'_{2n+1}}{\pi} K_{2n+1}(bR_{\min}), \tag{10.33b}$$

and

$$\mathrm{Gek}_{2n}(\xi, -q) \to \frac{p'_{2n+1}}{\pi} K_{2n+1}(bR_{\min}), \tag{10.34a}$$

$$\mathrm{Gek}_{2n+2}(\xi, -q) \to \frac{s'_{2n+2}}{\pi} K_{2n+2}(bR_{\min}), \tag{10.34b}$$

in the circle limit (again, the p'_n and s'_n are defined in appendix A). Moreover, the two expressions in equation (10.2) can be combined to give

$$\frac{x^2}{\cos^2\phi} + \frac{y^2}{\sin^2\phi} = \gamma^2, \tag{10.35}$$

hence as $\gamma \to 0$, $y/x \to \pm\tan\phi$ and so the coordinate ϕ must tend to the polar angle, θ in the circle limit. In the limit $q \to 0$ the constant coefficients, $A_r^{(n)}$ and $B_r^{(n)}$, relating to the Mathieu characteristics in the expansions of the Mathieu functions (equations (A.1)–(A.4)) are given by (10.26) and hence

$$\mathrm{ce}_n(\phi, -q) \to \cos(n\theta) \qquad \text{and} \qquad \mathrm{se}_n(\phi, -q) \to \sin(n\theta). \tag{10.36}$$

Therefore substituting (10.33), (10.34) and (10.36) into (10.13) gives

$$\psi = \sum_{n=0}^{\infty} \left(A_n \cos(n\theta) + B_n \sin(n\theta)\right) K_n(bR_{\min}), \tag{10.37}$$

which is again the solution of Helmholtz equation outside a circle of radius $R_{\min}$, with

$$A_{2n} = \frac{C_{2n}p'_{2n}}{\pi}, \qquad A_{2n+1} = \frac{C_{2n+1}s'_{2n+1}}{\pi}, \tag{10.38a}$$

$$B_{2n+1} = \frac{D_{2n+1}p'_{2n+1}}{\pi}, \qquad B_{2n+2} = \frac{D_{2n+2}s'_{2n+2}}{\pi}. \tag{10.38b}$$

10.2.3 Determination of C_n, D_n

In order to make progress with the general elliptical eddy model, the coefficients C_n and D_n in (10.13) need to be determined. As in chapter 9, the outer solution, (10.13), will be matched to an inner solution consisting of an ellipse of fluid in near solid body rotation (the model eddy). In the absence of rotation and stratification, there exists an exact analytical solution to the Euler equations representing a precessing elliptical patch of uniform vorticity. This solution is called Kirchoff's vortex (Lamb 1932). Such ellipses in a fluid described by the shallow water equations must also precess (Cushman-Roisin et al. 1985, Young 1985) and thus this precession rate must be incorporated into the present elliptic model eddy and is here denoted, Ω. In general, Ω must be determined as part of the solution. In the reference frame now rotating with

the ellipse, the exterior streamfunction, ψ_{rot}, can be written as

$$\psi_{\text{rot}} = \psi_R + \psi, \tag{10.39}$$

where

$$\psi_R = -\frac{\Omega}{2}\left(x^2+y^2\right) = -\frac{\Omega\gamma^2}{4}\left(\cosh(2\xi)+\cos(2\phi)\right), \tag{10.40}$$

and ψ is given by equation (10.13). The eddy is fixed in this rotating frame and hence the boundary of the ellipse ($\xi = \xi_0$) must be a streamline, i.e. ψ_{rot} is constant on $\xi = \xi_0$. In particular ψ_{rot} doesn't vary with the angle ϕ and therefore, as an initial simplification the coefficients in the expression for ψ, (10.13), are chosen such that $C_{2n+1} = D_n = 0$ for all n and the solution becomes

$$\begin{aligned}\psi_{\text{rot}} = &-\frac{\Omega\gamma^2}{4}\left(\cosh(2\xi)+\cos(2\phi)\right)\\ &+\sum_{n=0}^{\infty} C_{2n}\text{Fek}_{2n}(\xi,-q)(-1)^n\sum_{r=0}^{\infty}(-1)^r A_{2r}^{(2n)}\cos(2r\phi),\end{aligned} \tag{10.41}$$

where the even Mathieu function, ce_{2n}, has been expressed in terms of its trigonometric expansion, (A.1). Expression (10.41) can be rewritten as

$$\begin{aligned}\psi_{\text{rot}} = &-\frac{\Omega\gamma^2}{4}\left(\cosh(2\xi)+\cos(2\phi)\right)\\ &+\left[C_0\text{Fek}_0(-1)^0A_0^{(0)} - C_2\text{Fek}_2(-1)^0A_0^{(2)} + C_4\text{Fek}_4(-1)^0A_0^{(4)} - \ldots\right]\\ &+\left[C_0\text{Fek}_0(-1)^1A_2^{(0)} - C_2\text{Fek}_2(-1)^1A_2^{(2)} + C_4\text{Fek}_4(-1)^1A_2^{(4)} - \ldots\right]\cos(2\phi)\\ &+\left[C_0\text{Fek}_0(-1)^2A_4^{(0)} - C_2\text{Fek}_2(-1)^2A_4^{(2)} + C_4\text{Fek}_4(-1)^2A_4^{(4)} - \ldots\right]\cos(4\phi)\\ &+\ldots.\end{aligned} \tag{10.42}$$

In section 10.4, the C_{2n} are carefully chosen so that ψ_{rot} is constant on the ellipse boundary. This requires the coefficients of $\cos(2n\phi) = 0$ for all n. In particular, from equation (10.42), the coefficients of $\cos(2n\phi)$ are equal to zero for all $n \neq 1$ and the coefficients of $\cos(2\phi)$ must balance.

The solution (10.42) can be further simplified by examining the relative sizes of the constants $C_0, C_2, \ldots$ in the exterior region $\xi > \xi_0$. To find the coefficients $C_0, C_2, \ldots$ the matrix equation

$$\begin{pmatrix} \mathrm{Fek}_0 A_0^{(0)} & -\mathrm{Fek}_2 A_0^{(2)} & \mathrm{Fek}_4 A_0^{(4)} & \cdots \\ -\mathrm{Fek}_0 A_2^{(0)} & \mathrm{Fek}_2 A_2^{(2)} & -\mathrm{Fek}_4 A_2^{(4)} & \cdots \\ \mathrm{Fek}_0 A_4^{(0)} & -\mathrm{Fek}_2 A_4^{(2)} & \mathrm{Fek}_4 A_4^{(4)} & \cdots \\ \vdots & \vdots & \vdots & \ddots \end{pmatrix} \begin{pmatrix} C_0 \\ C_2 \\ C_4 \\ \vdots \end{pmatrix} = \begin{pmatrix} 0 \\ \Omega\gamma^2/4 \\ 0 \\ \vdots \end{pmatrix}, \tag{10.43}$$

must be solved, i.e.

$$\begin{pmatrix} C_0 \\ C_2 \\ C_4 \\ \vdots \end{pmatrix} = \begin{pmatrix} \mathrm{Fek}_0 A_0^{(0)} & -\mathrm{Fek}_2 A_0^{(2)} & \mathrm{Fek}_4 A_0^{(4)} & \cdots \\ -\mathrm{Fek}_0 A_2^{(0)} & \mathrm{Fek}_2 A_2^{(2)} & -\mathrm{Fek}_4 A_2^{(4)} & \cdots \\ \mathrm{Fek}_0 A_4^{(0)} & -\mathrm{Fek}_2 A_4^{(2)} & \mathrm{Fek}_4 A_4^{(4)} & \cdots \\ \vdots & \vdots & \vdots & \ddots \end{pmatrix}^{-1} \begin{pmatrix} 0 \\ \Omega\gamma^2/4 \\ 0 \\ \vdots \end{pmatrix}. \tag{10.44}$$

In general, the above matrices are infinite and therefore to get any results the series in (10.41) must be truncated. Further, both series in (10.41) must be truncated at the same values of n and r otherwise a non-square matrix which is not invertible is obtained. In the next subsection values of the constants $C_0, C_2, \ldots$ are calculated for two different test cases. As will be demonstrated, the values of these constants motivate a simplified form for the streamfunction, ψ.

In what follows, the Mathieu functions are computed numerically. Both the Mathieu functions and the modified Mathieu functions of the third kind are approximated by using the first few terms of their expansions given in appendix A, i.e. computing the first ten terms gives values for Mathieu and modified Mathieu functions accurate to at least eight decimal places. The constants $A_r^{(n)}$ and $B_r^{(n)}$ are calculated through a set of recurrence relations,

see NBS [1951] for more detail. Results agree with tables of Mathieu functions published in NBS [1951] and Kirkpatrick [1960] to at least eight decimal places.

10.2.4 Simplification of the outer solution

Motivation for the simplification of the outer solution is provided through the following two examples.

Example 1: An ellipse with major axis, $R_{\max} = 2$ and minor axis, $R_{\min} = 0.5$ propagating at velocity $U = -2.1$

In this case

$$q = \frac{1}{4}\gamma^2 b^2 = \frac{1}{4}\left(R_{\max}^2 - R_{\min}^2\right)\frac{U+1}{U} = 0.491071, \tag{10.45}$$

and the eddy boundary is given (from, for example (10.1)) by

$$\xi_0 = \mathrm{Re}\left\{\cosh^{-1}\left(\frac{R_{\max}}{\gamma}\right)\right\} = 0.255413. \tag{10.46}$$

Choosing the reference value $\xi = 0.3 > \xi_0$ outside the ellipse at which to calculate the streamfunction and substituting (10.45) into (10.43) gives the following numerical values for the matrix to be inverted,

$$\begin{pmatrix} 0.069957 & -0.664659 & 21.668516 & -2163.647883 & \cdots \\ 0.016747 & 5.545827 & -706.355619 & 158630.239100 & \cdots \\ 0.000510 & 0.228952 & 17229.029987 & -1033370.884126 & \cdots \\ 0.000007 & 0.003525 & 423.311331 & 420777647.387603 & \cdots \\ \vdots & \vdots & \vdots & \vdots & \ddots \end{pmatrix}. \tag{10.47}$$

With the above parameter values the constants are found to be,

$$\begin{pmatrix} C_0 \\ C_2 \\ C_4 \\ C_6 \\ \vdots \end{pmatrix} = \begin{pmatrix} 1.55936556196 17\Omega \\ 0.16405354572 85\Omega \\ -0.00000222577 17\Omega \\ 0.00000000000 08\Omega \\ \vdots \end{pmatrix}. \tag{10.48}$$

Note that the constants, C_{2n} rapidly tend to zero and ψ_{rot} can be calculated at $\xi = 0.3$ by substituting the above values into equation (10.42),

$$\psi_{\text{rot}} = \Omega\,(0.004542 + 0.843885\cos(2\phi) + 0.002666\cos(4\phi) + 0.000017\cos(6\phi))\,. \tag{10.49}$$

Example 2: An ellipse with major axis, $R_{\max} = 4$ and minor axis, $R_{\min} = 0.5$ propagating at velocity $U = -1.1$

In this case

$$q = \frac{1}{4}\gamma^2 b^2 = \frac{1}{4}\left(R_{\max}^2 - R_{\min}^2\right)\frac{U+1}{U} = 0.357955, \tag{10.50}$$

and

$$\xi_0 = \text{Re}\left\{\cosh^{-1}\left(\frac{R_{\max}}{\gamma}\right)\right\} = 0.125657. \tag{10.51}$$

Again using $\xi = 0.3 > \xi_0$ and substituting (10.50) into (10.43) gives the following numerical values for the matrix to be inverted,

$$\begin{pmatrix} 0.104040 & -1.274584 & 70.459922 & -12378.521558 & \cdots \\ 0.018367 & 14.429938 & -3150.289016 & 1244988.898385 & \cdots \\ 0.000409 & 0.432475 & 105506.430118 & -111279664.791034 & \cdots \\ 0.000004 & 0.004846 & 1888.981638 & 6216854553.841640 & \cdots \\ \vdots & \vdots & \vdots & \vdots & \ddots \end{pmatrix}. \tag{10.52}$$

With the above parameter values the constants are found to be,

$$\begin{pmatrix} C_0 \\ C_2 \\ C_4 \\ C_6 \\ \vdots \end{pmatrix} = \begin{pmatrix} 3.28939582192820\Omega \\ 0.26844028102420\Omega \\ -0.00000111297810\Omega \\ 0.00000000000010\Omega \\ \vdots \end{pmatrix}. \tag{10.53}$$

Again the constants rapidly tend to zero and the value of ψ_{rot} at $\xi = 0.3$ is,

$$\psi_{\text{rot}} = \Omega\,(0.047929 + 2.65892\cos(2\phi) + 0.021934\cos(4\phi) + 0.000134\cos(6\phi))\,. \tag{10.54}$$

In both the above examples, the term corresponding to the $n = r = 1$ term in (10.41), i.e. the $\cos(2\phi)$ term, is by far the dominant. Therefore a good approximation to the solution for the outer streamfunction, ψ_{rot}, would be given by assuming $\psi \sim C_2\text{Fek}_2(\xi, -q)\cos(2\phi)$. However, it is also required that in the far-field the velocity field of an ellipse has the same structure as that of a circle, i.e.

$$\psi \to CK_0(bR_{\min}) \qquad \text{as} \qquad \xi \to \infty. \tag{10.55}$$

The limiting form of the Mathieu functions of the third kind, equation (10.33), are Bessel functions of the same order, and so to satisfy (10.55) a term involving Fek_0 must be kept in the solution for ψ_{rot}.

Hence, from the above evidence, a reasonable, approximate solution for the streamfunction outside the ellipse in the rotating frame is $\psi_{\text{rot}} = \psi_R + \psi$, where

$$\psi = C_0\text{Fek}_0(\xi, -q) + C_2\text{Fek}_2(\xi, -q)\cos(2\phi), \tag{10.56}$$

is the streamfunction in the non-rotating frame and ψ_R is the term due to the

rotation of the coordinate system, given by (10.40). Therefore

$$\psi_{\rm rot} = -\frac{\Omega\gamma^2}{4}\left(\cosh(2\xi)+\cos(2\phi)\right) + C_0 \mathrm{Fek}_0(\xi,-q) + C_2 \mathrm{Fek}_2(\xi,-q)\cos(2\phi). \quad (10.57)$$

Further, the tangential velocity according to (10.57) in the rotating frame, required for matching to the interior solution, is given by

$$-\frac{\partial \psi_{\rm rot}}{\partial \xi} = \frac{\Omega\gamma^2}{2}\sinh(2\xi) - C_0\frac{\partial}{\partial\xi}\mathrm{Fek}_0(\xi,-q) - C_2\frac{\partial}{\partial\xi}\mathrm{Fek}_2(\xi,-q)\cos(2\phi). \quad (10.58)$$

It remains to find the form of the precession rate, Ω, and the constants C_0 and C_2. In the next section the interior structure of the elliptic eddy model is described. This inner solution is then matched to the exterior streamfunction and tangential velocity, enabling the determination of these unknown parameters.

10.3 The inner solution

As in chapter 9, a Gaussian profile for the streamfunction inside the ellipse is chosen. In a frame rotating with the ellipse the assumed profile is

$$\eta_{\rm rot}(x,y) = \eta_0 e^{-\left(x^2+\left(\frac{R_{\rm max}}{R_{\rm min}}y\right)^2\right)}, \quad (10.59)$$

where $R_{\rm min}$ and $R_{\rm max}$ are a further two unknown parameters. Note that in the circle limit, $R_{\rm max} \to R_{\rm min}$, (10.59) is of exactly the same form as (9.25). Also, as for the circular model, (10.59) is not necessarily an exact solution of the nonlinear shallow water equations, but merely one that decays rapidly

enough so that quasi-geostrophic theory becomes appropriate at some distance from the eddy. Writing x and y in terms of the elliptic coordinates ξ and ϕ (definitions (10.2)), equation (10.59) becomes

$$\eta_{\rm rot}(\xi,\phi) = \eta_0 e^{-\gamma^2\left(\cosh^2\xi\cos^2\phi + \frac{R_{\rm max}^2}{R_{\rm min}^2}\sinh^2\xi\sin^2\phi\right)}. \tag{10.60}$$

Now, from the definitions (10.2),

$$\cosh\xi_0 = \frac{R_{\rm max}}{\gamma} \qquad \text{and} \qquad \sinh\xi_0 = \frac{R_{\rm min}}{\gamma}, \tag{10.61}$$

and the inner solution on the boundary, $\xi = \xi_0$, in a frame rotating with the ellipse is

$$\eta_{\rm rot}(\xi_0,\phi) = \eta_0 e^{-R_{\rm max}^2}. \tag{10.62}$$

Therefore this inner streamfunction is constant on the boundary of the ellipse, i.e. the ellipse boundary is a streamline, as required. Furthermore, the tangential velocity due to the inner solution is

$$-\frac{\partial\eta_{\rm rot}}{\partial\xi}(\xi,\phi) = 2\gamma^2\cosh\xi\sinh\xi\left(\cos^2\phi + \frac{R_{\rm max}^2}{R_{\rm min}^2}\sin^2\phi\right)\eta_{\rm rot}(\xi,\phi), \tag{10.63}$$

and on the ellipse boundary this becomes, using (10.61) and double angle formulae,

$$-\left.\frac{\partial\eta_{\rm rot}}{\partial\xi}\right|_{\xi=\xi_0} = \eta_0 e^{-R_{\rm max}^2}\frac{R_{\rm max}}{R_{\rm min}}\left(\left(R_{\rm min}^2 + R_{\rm max}^2\right) + \left(R_{\rm min}^2 - R_{\rm max}^2\right)\cos(2\phi)\right). \tag{10.64}$$

10.4 Matching

As stated previously (and as in the case of a circular eddy) the inner and outer streamfunctions and tangential velocities must match across the ellipse boundary, $\xi = \xi_0$. Matching the inner solution streamfunction, (10.62), and the

outer solution streamfunction, (10.57), in the rotating frame at the boundary $\xi = \xi_0$ yields,

$$\eta_0 e^{-R_{\max}^2} = -\frac{\Omega\gamma^2}{4}(\cosh(2\xi_0) + \cos(2\phi)) + C_0 \mathrm{Fek}_0(\xi_0, -q) + C_2 \mathrm{Fek}_2(\xi_0, -q)\cos(2\phi). \quad (10.65)$$

Also matching the tangential velocities (10.64) and (10.58) at $\xi = \xi_0$ gives

$$-\eta_0 e^{-R_{\max}^2}\frac{R_{\max}}{R_{\min}}\left((R_{\min}^2 + R_{\max}^2) + (R_{\min}^2 - R_{\max}^2)\cos(2\phi)\right) = -\frac{\Omega\gamma^2}{2}\sinh(2\xi_0) + C_0\left.\frac{\partial}{\partial\xi}\left(\mathrm{Fek}_0(\xi, -q)\right)\right|_{\xi=\xi_0} + C_2\left.\frac{\partial}{\partial\xi}\left(\mathrm{Fek}_2(\xi, -q)\right)\right|_{\xi=\xi_0}\cos(2\phi). \quad (10.66)$$

Note, from (10.61),

$$\cosh(2\xi_0) = \cosh^2\xi_0 + \sinh^2\xi_0 = \frac{R_{\max}^2 + R_{\min}^2}{\gamma^2},$$
$$\sinh(2\xi_0) = 2\sinh\xi_0\cosh\xi_0 = \frac{2R_{\max}R_{\min}}{\gamma^2}. \quad (10.67)$$

Comparing constant terms and coefficients of $\cos(2\phi)$ in (10.65) and (10.66) gives four equations in the six unknowns, $R_{\max}$ and $R_{\min}$, the major and minor axis lengths, η_0, the maximum depth of the ellipse, the constants C_0 and C_2 and the rotation rate, Ω, i.e. using (10.67), the four equations are,

$$\eta_0 e^{-R_{\max}^2} = -\frac{\Omega}{4}(R_{\max}^2 + R_{\min}^2) + C_0\mathrm{Fek}_0(\xi_0, -q), \quad (10.68)$$

$$-\frac{\Omega}{4}(R_{\max}^2 - R_{\min}^2) + C_2\mathrm{Fek}_2(\xi_0, -q) = 0, \quad (10.69)$$

$$-\eta_0 e^{-R_{\max}^2}\frac{R_{\max}}{R_{\min}}\left(R_{\max}^2 + R_{\min}^2\right) = -\Omega R_{\max}R_{\min} + C_0\left.\frac{\partial}{\partial\xi}\left(\mathrm{Fek}_0(\xi, -q)\right)\right|_{\xi=\xi_0}, \quad (10.70)$$

$$\eta_0 e^{-R_{\max}^2}\frac{R_{\max}}{R_{\min}}\left(R_{\max}^2 - R_{\min}^2\right) = C_2\left.\frac{\partial}{\partial\xi}\left(\mathrm{Fek}_2(\xi, -q)\right)\right|_{\xi=\xi_0}, \quad (10.71)$$

where the definition $\gamma^2 = R_{\max}^2 - R_{\min}^2$ has been used in (10.69). Implicit in the above is the supposition that the translational velocity, U, is known. Clearly some assumptions have to be made to make further progress. It is assumed that $R_{\min}$ and η_0 are known (good first approximations to $R_{\min}$, η_0 and U can be calculated by using the algorithm for a circular eddy of chapter 9). Further, the appropriate Bessel functions are used as approximations to the modified Mathieu functions. Equations (10.68)–(10.71) are then four equations in the four unknowns Ω, $R_{\max}$, C_0 and C_2. They can be rearranged to form one equation for $R_{\max}$ depending only on the other ellipse parameter, $R_{\min}$, in the following way. First, note (10.69) gives

$$C_2 = \frac{1}{K_2(\chi)} \frac{\Omega}{4} \left(R_{\max}^2 - R_{\min}^2 \right), \tag{10.72}$$

where

$$\chi = \frac{1}{2} b\gamma e^{\xi_0} = \frac{1}{2} b \sqrt{|R_{\max}^2 - R_{\min}^2|} \exp\left(\mathrm{Re}\left\{ \cosh^{-1}\left(\frac{R_{\max}}{\sqrt{R_{\max}^2 - R_{\min}^2}} \right) \right\} \right). \tag{10.73}$$

Substitution of the expression for C_2, (10.72), into (10.71) yields an expression for the precession rate, Ω, which depends on the ellipse axis lengths, $R_{\max}$ and $R_{\min}$, i.e.

$$\Omega = -8\eta_0 e^{-R_{\max}^2} \frac{R_{\max}}{R_{\min}} \frac{K_2(\chi)}{\chi(K_1(\chi) + K_3(\chi))}. \tag{10.74}$$

Note, Cushman-Roisin et al. [1985] and Cushman-Roisin [1986] also derive expressions for the precession rate, Ω, of a shallow water, elliptical eddy which are dependent on the ellipse size parameters. Comparison to their expressions will be made later. Equation (10.68) can be rearranged to give C_0 as

$$C_0 = \frac{1}{K_0(\chi)} \left(\eta_0 e^{-R_{\max}^2} + \frac{\Omega}{4} \left(R_{\max}^2 + R_{\min}^2 \right) \right). \tag{10.75}$$

Finally, by substituting expression (10.75) for C_0, and (10.74) for Ω, equation (10.70) is one equation in the one unknown, $R_{\max}$. Furthermore, since C_0 and Ω

are proportional to η_0, the major axis length, $R_{\max}$, is uniquely determined by the translational velocity, U, and the minor axis length, $R_{\min}$, only. Equation (10.70) must be solved numerically for $R_{\max}$ and figure 10.2 depicts how the major axis length, $R_{\max}$, varies as a function of the minor axis length, $R_{\min}$, (according to (10.70)) for (a) $U = -1.1$ ($\approx 0.04\,\mathrm{m\,s^{-1}}$, a realistic value for the translational velocity of a Loop Current Eddy), (b) $U = -2.5$ ($\approx 0.1\,\mathrm{m\,s^{-1}}$, an approximate lower bound for Loop Current Eddy translational velocities) and (c) $U \to -\infty$. Notice that, in each case, that for $R_{\min}$ large enough, the

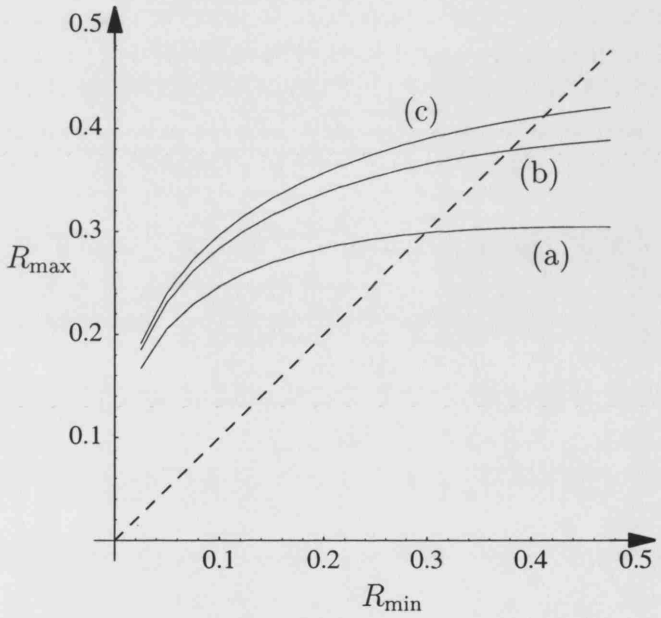

Figure 10.2: Solution for $R_{\max}$ as a function of $R_{\min}$ given by equation (10.70) for (a) $U = -1.1$, (b) $U = -2.5$ and (c) $U \to -\infty$. The line $R_{\min} = R_{\max}$ is also shown (dashed). Notice that, in each case, for $R_{\min}$ large enough, equation (10.70) implies $R_{\max} < R_{\min}$.

solution for the major axis is smaller than the minor axis, i.e. $R_{\max} < R_{\min}$. For such solutions the equations break down and streamfunctions and velocities no longer match on the ellipse boundary. Therefore, the algorithm must be

restricted to cases where $R_{\min} < R_{\max}$ with the consequence that given a minor axis length $R_{\min}$ there may not exist any permitted solutions for $R_{\max}$. This also seems to imply that only small eddies ($R_{\min} \lesssim 0.4$) are permitted by the ellipse model, however, $R_{\min}$ and $R_{\max}$ measure only the distances at which the streamfunction solution changes from Bessel type to Gaussian and therefore do not necessarily indicate the size of the eddy. Notice that, even with the constraint that $R_{\min} < R_{\max}$, equation (10.70) admits solutions for almost all ellipse eccentricities. For example, the region of figure 10.2 for which $R_{\min} < R_{\max}$ clearly depicts solutions that are nearly circular ($R_{\min} \sim R_{\max}$) through to highly elliptical solutions ($R_{\min} \ll 1$) for all values of U. Therefore, when solving (10.70), it is better to assume the eddy eccentricity, E, is known rather than the length $R_{\min}$, since this almost always guarantees a valid solution for $R_{\max}$. Therefore the substitution

$$R_{\min} = R_{\max}\sqrt{1 - E^2}, \tag{10.76}$$

is made and, given E, figure 10.3 shows the ellipses generated by solutions to (10.70). Kirwan et al. [1984b] have observed elliptical Loop Current Eddies which vary in size and shape throughout their life span and have eccentricities in the range $0.6 \lesssim E \lesssim 0.95$ (Hamilton et al. 1999 observe an even wider range of eccentricities for Loop Current Eddies). In this chapter only constant shape ellipses are considered and on the basis of the aforementioned observations an average eccentricity of $E = 0.7$ is used. The 'bold' ellipse in figure 10.3 represents this solution corresponding to $E = 0.7$.

Figure 10.4 shows how the precession rate, Ω, given by (10.74) varies with the eccentricity, E, for the case $U = -1.1$. Note that the precession rate depends on the maximum depth of the ellipse, η_0. This variable is assumed to be known and is found by appealing to the circle approximation, equation

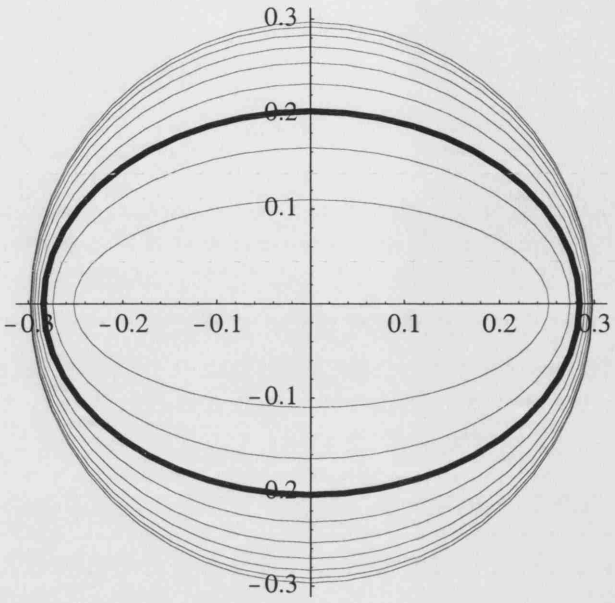

Figure 10.3: Ellipses generated by solutions to equation (10.70) for $U = -1.1$ and $E = 0.1i$, $i = 1, \ldots, 9$. The 'bold' ellipse represents the solution for typical Loop Current Eddy eccentricities, $E = 0.7$.

(9.27), with $R = \bar{R}$, where

$$\bar{R} = \frac{R_{\min} + R_{\max}}{2}. \tag{10.77}$$

Observe that, as expected (Lamb 1932), as the eddy becomes more elliptical ($E \to 1$), so the precession rate increases. Also, the precession rate is always negative implying that the eddy precesses in the clockwise direction. This is consistent with the direction of fluid rotation in Loop Current Eddies. In the present model and those of Cushman-Roisin et al. [1985] and Cushman-Roisin [1986], it is not necessarily true that $\Omega \to 0$ in the circle limit, $R_{\max} \to R_{\min}$. In fact, from equation (10.74),

$$\Omega \to -8\eta_0 e^{-R_{\min}^2} \frac{K_2(bR_{\min})}{bR_{\min}(K_1(bR_{\min}) + K_3(bR_{\min}))} \quad \text{as} \quad R_{\max} \to R_{\min}. \tag{10.78}$$

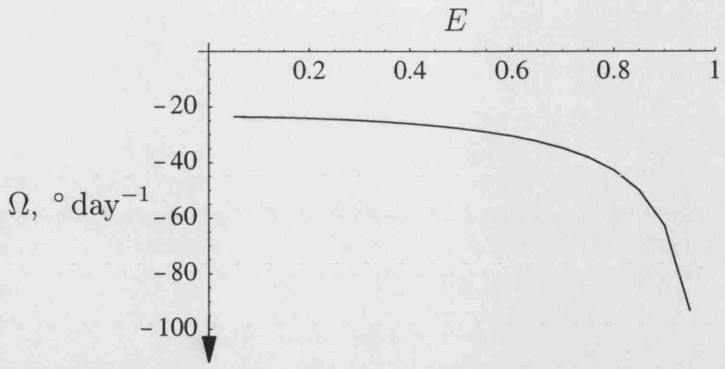

Figure 10.4: Variation of precession rate, Ω, with eccentricity, E.

In dimensional coordinates (using $U = -1.1$ and $R_{\min} \approx 0.3$, the approximate value at which $R_{\min} = R_{\max}$, see figure 10.2(a)) this corresponds to

$$\Omega \to -5.35227\hat{\beta}f \times (24 \times 60 \times 60) \times \frac{360}{2\pi} \approx 24.9^\circ \,\text{day}^{-1} \quad \text{as} \quad R_{\max} \to R_{\min}. \tag{10.79}$$

Indeed the curve in figure 10.4 appears to asymptote to this value as $R_{\max} \to R_{\min}$ or equivalently, as $E \to 0$. The precession rates generated by the ellipse model (figure 10.4) can be tentatively compared to the models of Cushman-Roisin et al. [1985] and Cushman-Roisin [1986]. Cushman-Roisin et al. [1985] develop a model based on frontal geostrophic dynamics and the precession rate has the form,

$$\Omega = \frac{\omega}{2} = \frac{f}{2} - \frac{f}{4}\left[\left(1 + \frac{8R_d^2}{R^2}\right)^{1/2} + \left(1 - \frac{8R_d^2}{R^2}\right)^{1/2}\right] \approx 0.024f, \tag{10.80}$$

using their example where $f \approx 10^{-4}\,\text{s}^{-1}$, the geometric mean radius, $R \approx 100$ km and the deformation radius, $R_d \approx 27$ km. This corresponds to

$$\Omega \approx 0.024f \times (24 \times 60 \times 60) \times \frac{360}{2\pi} \approx 12^\circ \,\text{day}^{-1}. \tag{10.81}$$

Also, Cushman-Roisin [1986] derive a precession rate from the asymptotic limit of (10.80) as the eddy becomes large, giving

$$\Omega = 4f\left(\frac{R_d}{R}\right)^4 \approx 0.021f, \tag{10.82}$$

which corresponds to

$$\Omega \approx 0.021f \times (24 \times 60 \times 60) \times \frac{360}{2\pi} \approx 11^\circ \,\mathrm{day}^{-1}. \tag{10.83}$$

Further, observations (of Gulf Stream rings, Cushman-Roisin et al. 1985 and references therein) show $\Omega \approx 9^\circ \,\mathrm{day}^{-1}$. Thus, the present model eddy gives precession rates in good agreement with (of the same order as) observations and previous models (although based on fundamentally different dynamics).

Moreover, since $\Omega \nrightarrow 0$ in the circle limit, generally, taking the circle limit of the precessing ellipse model gives a different velocity signature to the non-precessing circle of chapter 9. The outer streamfunction in the non-rotating frame, (10.56), in the circle limit does reduce to the form of that of the non-precessing circle, i.e. by equation (10.72), $C_2 \to 0$ as $R_{\max} \to R_{\min}$, and

$$\psi \to C_0 \frac{p_0'}{\pi} K_0(bR_{\min}), \tag{10.84}$$

using the limiting form of Fek_0, (10.33). Equation (10.84) is of exactly the same form as the outer streamfunction used in chapter 9, equation (9.24). However, the precessing inner streamfunction (in the non-rotating frame) differs by a term due to transforming from the rotating to the non-rotating frame, i.e. $\eta = \eta_{\mathrm{rot}} - \psi_R$ and therefore

$$\eta \to \eta_0 e^{-R_{\min}^2} + \frac{\Omega}{2} R_{\min}^2, \tag{10.85}$$

in the circle limit. This has the consequence that results produced here, in the (precessing) circle limit cannot, in general, be directly compared with those of chapter 9.

The differences, due to precession, between the models used in this and the previous chapter are further demonstrated by examining the circle limit of equations (10.65) and (10.66). As $R_{\max} \to R_{\min}$, equation (10.65) becomes

$$\eta_0 e^{-R_{\min}^2} = -\frac{\Omega}{2} R_{\min}^2 + C_0 \frac{p_0'}{\pi} K_0(bR_{\min}). \tag{10.86}$$

By analogy to the modified Mathieu functions of the first and second kinds detailed in McLachlan [1947]

$$\frac{\partial}{\partial \xi}\left(\mathrm{Fek}_{2n}(\xi,-q)\right) \rightarrow R_{\min}\frac{p'_{2n}}{\pi}\frac{\partial}{\partial R_{\min}}K_{2n}(bR_{\min}) \quad \text{as} \quad R_{\max} \rightarrow R_{\min}, \tag{10.87}$$

and so, in the circle limit, (10.66) becomes

$$-2R_{\min}^2\eta_0 e^{-R_{\min}^2} = -\Omega R_{\min}^2 - R_{\min}C_0\frac{p'_0}{\pi}bK_1(bR_{\min}). \tag{10.88}$$

Equations (10.86) and (10.88) are of exactly the same form as those derived for the circle case, (9.27) and (9.28), except with an extra term due to the rotation of the reference frame.

In summary, since the outer streamfunctions are identical in the far-field (equivalent to the circle limit), the same process as in chapter 9 can be employed to find the parameters U and (x_0, y_0) for the ellipse model. Then assuming the eccentricity, E, and the maximum depth of the ellipse η_0 are known, all remaining parameters can be calculated and subsequent velocities predicted according to the equations derived in the next section.

10.5 The time series problem

A measuring station located at (x_{ms}, y_{ms}) will measure fluid velocities u and v due to the presence of an elliptical eddy centred at (x_i, y_i) in the x- and y-directions, respectively, given by

$$u = \begin{cases} -\left.\dfrac{\partial \psi}{\partial y}\right|_{(x_{ms},y_{ms})}, & \text{if } \xi > \xi_0, \\ -\dfrac{\partial}{\partial y}\left(\eta_{\mathrm{rot}} - \psi_R\right)\Big|_{(x_{ms},y_{ms})}, & \text{if } \xi < \xi_0, \end{cases} \tag{10.89}$$

$$v = \begin{cases} \left.\dfrac{\partial \psi}{\partial x}\right|_{(x_{ms},y_{ms})}, & \text{if } \xi > \xi_0, \\ \left.\dfrac{\partial}{\partial x}\left(\eta_{\text{rot}} - \psi_R\right)\right|_{(x_{ms},y_{ms})}, & \text{if } \xi < \xi_0, \end{cases} \tag{10.90}$$

where ψ is given by (10.56), η_{rot} by (10.59) and ψ_R by (10.40), i.e.

$$u = \begin{cases} -\left.\left(\dfrac{\partial \psi}{\partial \xi}\dfrac{\partial \xi}{\partial y} + \dfrac{\partial \psi}{\partial \phi}\dfrac{\partial \phi}{\partial y}\right)\right|_{(x_{ms},y_{ms})}, & \text{if } \xi > \xi_0, \\ -\left.\left(\dfrac{\partial \eta_{\text{rot}}}{\partial y} + \Omega\left(y - y_i\right)\right)\right|_{(x_{ms},y_{ms})}, & \text{if } \xi < \xi_0, \end{cases} \tag{10.91}$$

$$v = \begin{cases} \left.\left(\dfrac{\partial \psi}{\partial \xi}\dfrac{\partial \xi}{\partial x} + \dfrac{\partial \psi}{\partial \phi}\dfrac{\partial \phi}{\partial x}\right)\right|_{(x_{ms},y_{ms})}, & \text{if } \xi > \xi_0, \\ \left.\left(\dfrac{\partial \eta_{\text{rot}}}{\partial x} + \Omega\left(x - x_i\right)\right)\right|_{(x_{ms},y_{ms})}, & \text{if } \xi < \xi_0. \end{cases} \tag{10.92}$$

Using the definition of ψ, (10.56),

$$u = \begin{cases} -\left[\left(C_0\dfrac{\partial}{\partial \xi}\text{Fek}_0(\xi,-q) + C_2\dfrac{\partial}{\partial \xi}\text{Fek}_2(\xi,-q)\cos(2\phi)\right)\dfrac{\partial \xi}{\partial y}\right. \\ \left. + \left(-2C_2\text{Fek}_2(\xi,-q)\sin(2\phi)\right)\dfrac{\partial \phi}{\partial y}\right]_{(x_{ms},y_{ms})}, & \text{if } \xi > \xi_0, \\ 2\eta_0\dfrac{R_{\max}}{R_{\min}}\left(y_{ms} - y_i\right)e^{-\left(\left(x_{ms}-x_i\right)^2 + \frac{R_{\max}^2}{R_{\min}^2}\left(y_{ms}-y_i\right)^2\right)} & \\ -\Omega\left(y_{ms} - y_i\right), & \text{if } \xi < \xi_0, \end{cases} \tag{10.93}$$

$$v = \begin{cases} \left[\left(C_0\dfrac{\partial}{\partial \xi}\text{Fek}_0(\xi,-q) + C_2\dfrac{\partial}{\partial \xi}\text{Fek}_2(\xi,-q)\cos(2\phi)\right)\dfrac{\partial \xi}{\partial x}\right. \\ \left. + \left(-2C_2\text{Fek}_2(\xi,-q)\sin(2\phi)\right)\dfrac{\partial \phi}{\partial x}\right]_{(x_{ms},y_{ms})}, & \text{if } \xi > \xi_0, \\ -2\eta_0\left(x_{ms} - x_i\right)e^{-\left(\left(x_{ms}-x_i\right)^2 + \frac{R_{\max}^2}{R_{\min}^2}\left(y_{ms}-y_i\right)^2\right)} & \\ +\Omega\left(y_{ms} - y_i\right), & \text{if } \xi < \xi_0. \end{cases} \tag{10.94}$$

Note that the the velocity field is measured in the non-rotating frame. Therefore (using (10.1)),

$$\xi = \text{Re}\left\{\cosh^{-1}\left(\frac{(x+iy)e^{-i\Omega t_i}}{\gamma}\right)\right\}, \tag{10.95}$$

and

$$\phi = \mathrm{Im}\left\{\cosh^{-1}\left(\frac{(x+iy)e^{-i\Omega t_i}}{\gamma}\right)\right\}, \tag{10.96}$$

where $x = x_{ms} - x_0 - Ut_i$ and $y = y_{ms} - y_0$, assuming the eddy translates solely in the westward direction.

Plots of typical time series of u and v velocities measured as elliptical eddies propagate by (given by equations (10.93) and (10.94)) are compared with those derived from the circular eddy equations (9.32) and (9.34) in figures 10.5(a) and (b). The graphs describe velocities measured at (x_{ms}, y_{ms}) due to eddies which are initially located in the far-field, travel in a straight line due westward at a constant speed towards the measuring station, 'hit' it, and continue on into the far-field. The short-dashed line represents the circular solution of chapter 9

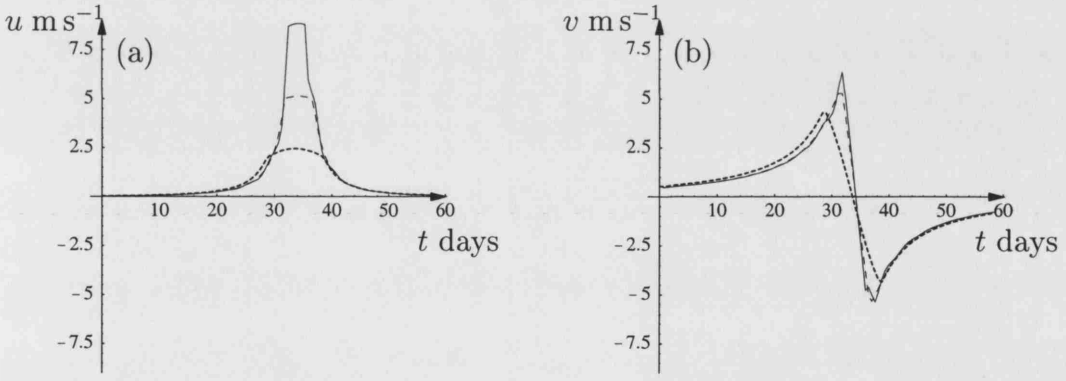

Figure 10.5: Comparison of velocity profiles generated by the circle and ellipse algorithms. The short-dashed line represents data given by the circle algorithm, the solid line corresponds to an ellipse with $E = 0.7$ (a typical Loop Current Eddy value) and the dashed line, an ellipse with $E = 0.1$, (nearly circular) (a) u velocity and (b) v velocity.

and is exactly as figure 9.4, i.e. the parameters used are, again, $U = -1.1$, $(x_0, y_0) = (3, -0.2)$ and $C = 1$ (giving a matching radius of $R = 0.486947$ and maximum eddy depth of $\eta_0 = 2.59965$). This is compared with two time series

generated by the ellipse algorithm, using the the same translational velocities ($U = -1.1$) and initial positions ($(x_0, y_0) = (3, -0.2)$) as for the circle. The dashed line shows the time series generated by an ellipse with eccentricity, E, chosen such that the ellipse is nearly circular, i.e. $E = 0.1$. Here, using equation (10.70), $R_{\max} = 0.298116$ and by equation (10.76), $R_{\min} = 0.296622$ (see also figure 10.2). Recall that the maximum depth of the eddy is also required and is estimated using equation (9.27) with $R = \bar{R}$, giving $\eta_0 = 2.76911$. The remaining parameters are found to be $C_0 = 0.910897$, $C_2 = -4.54819 \times 10^{-6}$ and $\Omega = -5.08267$ from equations (10.75), (10.72) and (10.74) respectively. This value of Ω corresponds to a precession rate of $\approx 23.6°\,\text{day}^{-1}$. The solid line represents a more typical ellipse shaped eddy where the eccentricity is $E = 0.7$, giving $R_{\max} = 0.284093$ and $R_{\min} = 0.202883$. In this case (given that $\eta_0 = 2.89949$) $C_0 = 0.895399$, $C_2 = 1.99576 \times 10^{-4}$ and $\Omega = -7.48058$ or $\approx 34.8°\,\text{day}^{-1}$.

As argued previously, the ellipse solutions tend to that of the circle in the far-field, hence the three velocity profiles in figure 10.5 are almost coincident for small and large times where the eddies are far from the measuring station. Differences in the velocity profiles (especially in the u velocity) are seen as as the eddy approaches the measuring station. The circle algorithm (short-dashed) predicts comparatively small velocities, whereas the near circular ellipse (dashed) generates larger velocities and the ellipse with $E = 0.7$ (solid), larger velocities still. This is because the 'sizes' of the eddies, or more accurately the radius at which the solution switches from Bessel type to Gaussian, decreases as the eccentricity increases. As the eddies approach the measuring station, due to the Bessel function nature of the outer solution, velocities begin to increase rapidly. The circle solution has the largest matching radius, R, and

so 'hits' the measuring station first and the velocities switch to the (bounded) Gaussian type. Since R is smaller for ellipses, they can get closer to the measuring station before switching and hence produce larger Bessel type velocities. This also explains the difference between the circle and near circular ellipse solutions. Note also that the effects of precession can be seen in the eccentric ellipse ($E = 0.7$) velocity profile. Deviations from the smooth, respectively symmetric and antisymmetric, u and v velocity profiles can be seen at $t = 29$ and $t = 37$ days.

Figure 10.6 shows the time evolution of an elliptical model eddy and the associated streamfunctions corresponding to the $E = 0.7$ ellipse (which generated the solid line velocity profile in figure 10.5) for the period $t = 30$ to $t = 38$ days. At $t = 30$ days, the ellipse is approaching the measuring station (marked by a cross in the figure). By $t = 33$ days the ellipse has 'hit' the measuring station and the predicted velocities will be of the Gaussian type. By $t = 36$ days the eddy has passed through the measuring station and continue on into the far-field. The precession rate of $\approx 34.8°\,\text{day}^{-1}$ is clear. Note that the outer streamfunction quickly tends to concentric circles in the far-field. Also shown (dashed) is the time evolution of the corresponding circular eddy calculated using the same parameter values as for the ellipse. It can be seen clearly that as the circle is larger, it 'hits' the measuring station first ($t = 31$ days) and therefore induces smaller Gaussian velocities over a longer time period.

The model can now be used to predict local velocities generated by the passage of a nearby rotating, precessing, elliptical eddy. As mentioned above, the ellipse solution approaches that of the circle in the far-field. Therefore the method detailed in section 9.4 can be used to determine some parameters, namely the initial position and the propagation speed, from a set of measured

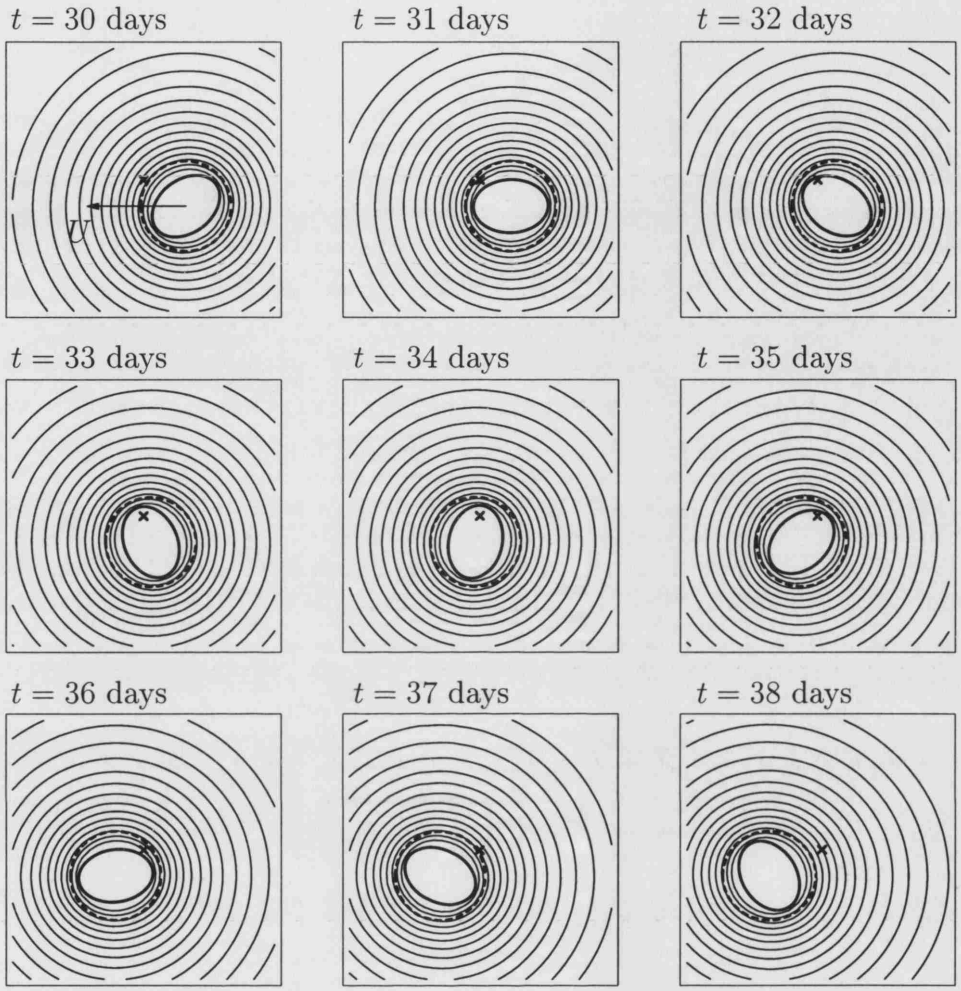

Figure 10.6: Time evolution of an elliptic eddy and the associated stream-function in a fixed frame of reference. The cross indicates the position of the measuring station, (x_{ms}, y_{ms}). The dashed circle represents the time evolution of the corresponding circular eddy of chapter 9 calculated using the same values of U, (x_0, y_0) and C as the ellipse.

velocity data. From these, given an eccentricity, E, and a maximum depth, η_0, the ellipse equations, (10.68)–(10.71), are used to determine the remaining properties of a rotating, precessing, elliptical eddy. Moreover, equations (10.93) and (10.94) can then be used to predict the subsequent velocities gen-

erated by the elliptic eddy.

It has been shown, in section 9.5, that the algorithm used to determine the translational velocity and the initial position of the eddy centre is fairly robust with respect to the introduction of noise. The ellipse equations are used only to calculate additional parameters and will not be further affected by any noise. Therefore it is now possible to apply the ellipse algorithm directly to the Loop Current Eddy data.

10.6 Application to Loop Current Eddies

The ellipse algorithm is now applied to the data relating to the two Loop Current Eddy events introduced in section 9.6. In each case the eccentricity is taken to be $E = 0.7$. This is a typical value for Loop Current Eddies (Kirwan et al. 1984b).

Results for the second Loop Current Eddy, LCE2, are shown in figure 10.7. The circle algorithm is used to calculate the translational velocities and the initial position of the eddy centre. Hence these parameters are found to have the same values as in section 9.6, namely $U = -1.5323$ (a westward translation of $\approx 0.059\ \mathrm{m\,s^{-1}}$) and $(x_0, y_0) = (0.788078, -1.35227)$ (ellipse initially centred ≈ 32 km to the east and ≈ 55 km south of the measuring station). Equation (10.70) is used to calculate the major axis length, $R_{\max} = 0.328928$ and by equation (10.76), $R_{\min} = 0.234902$, given that the maximum depth has a value of $\eta_0 = 1.92492$. The remaining parameters are found to be $C_0 = 0.793035$, $C_2 = -8.85265 \times 10^{-4}$ and $\Omega = -4.80577$ from equations (10.75), (10.72) and (10.74) respectively. This value of Ω corresponds to a precession rate of $\approx 22.3^\circ\,\mathrm{day}^{-1}$.

For the LCE2 eddy, there is no significance difference between the velocities

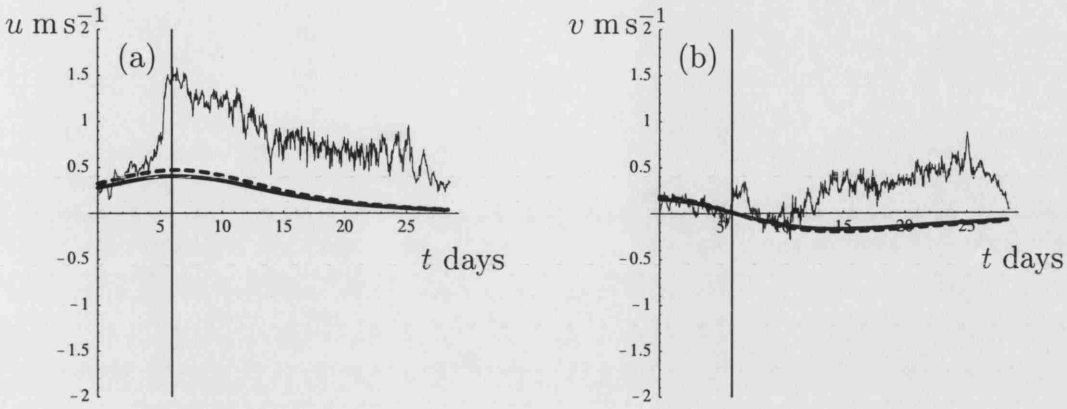

Figure 10.7: Predicted data for LCE2 generated by the ellipse algorithm (solid) compared with the circle algorithm (dashed). The original LCE2 data is given by the thin solid line, (a) u velocity and (b) v velocity. The solid vertical line represents the time t_p.

generated by the circle and ellipse algorithms (the solid (ellipse) and dashed (circle) lines in figure 10.7 are almost coincident). This is because the predicted path of the eddy does not pass sufficiently close to the measuring station as to generate velocities given by the interior solutions (equation (9.25) for the circle case and (10.62) for the ellipse case). Therefore the velocities predicted by the circular and elliptic models are essentially the same since the ellipse solution tends to that of the circle in the far-field. As explained in section 9.6, the models predict the general velocity trends fairly well but underestimate the velocity magnitudes. Recall that this is due to the discontinuity at $t = 6$ days. Nevertheless, the predicted precession rate of $\approx 22.3°\,\text{day}^{-1}$ is in good agreement with observed Loop Current Eddies (see section 10.5 for typical values).

Results for the third Loop Current Eddy, LCE3, are shown in figure 10.8. As in section 9.6, $U = -1.47104$ (a westward translation of $\approx 0.056\,\text{m s}^{-1}$) and $(x_0, y_0) = (1.39973, -0.351354)$ (ellipse initially centred ≈ 57 km to the

east and $\approx$ 14 km south of the measuring station). For the LCE3 data, the

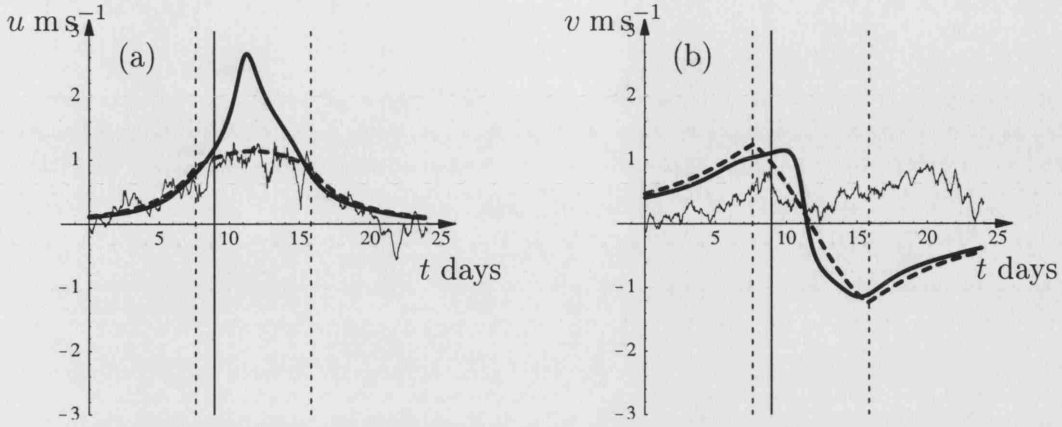

Figure 10.8: Predicted data for LCE3 generated by the ellipse algorithm (solid) compared with the circle algorithm (dashed). The original LCE3 data is given by the thin solid line, (a) u velocity and (b) v velocity. The dashed vertical lines represent the circular boundaries $r = R$ where the velocities switch from Bessel type to Gaussian. The solid vertical line represents the time t_p.

major axis length is found to be $R_{\max} = 0.325606$ and the minor axis, $R_{\min} = 0.232529$, given that the maximum depth has a value of $\eta_0 = 2.17631$. The remaining parameters are found to be $C_0 = 0.878389$, $C_2 = -8.87765 \times 10^{-4}$ and $\Omega = -5.44866$. This value of Ω corresponds to a precession rate of $\approx 25.3^\circ\,\text{day}^{-1}$.

In this case the predicted velocities for the circle and ellipse algorithms differ substantially when the eddy gets close to the measuring station. The ellipse algorithm (solid line, figure 10.8) substantially overestimates the magnitude of the u velocities. The v velocity profile is also significantly different from that predicted by the circle algorithm. These differences are due to the fact that elliptic eddy is, in a sense, smaller than the circular eddy, i.e. for the ellipse, $R_{\max} = 0.33$ whereas for the circle, $R = 0.60$. At its closest point,

the position of the eddy centre is a (nondimensional) distance $r = y_0 = 0.35$ away from the measuring station. Since $R_{\max} < y_0 < R$, the ellipse will never 'hit' the measuring station and so will always record the larger Bessel type velocities (see also section 10.5 and figure 10.5). Conversely, the circle solution hits the measuring station and reverts to the comparatively smaller Gaussian velocity profile between the times marked by the dashed vertical lines in figure 10.8. The circle algorithm predicts the actual eddy velocities in the x-direction more accurately than the ellipse algorithm. The velocities in the y-direction are equally well described by both models (and as explained in section 9.6 the deviation beyond $t = 13$ days could be due to eddy deformation or the presence of other eddies).

As with the LCE2 case the predicted precession rate is fairly consistent with those of observed Loop Current Eddies. Further, the effects of this precession can be seen, particularly in the v velocity prediction, in the deviation of the velocity profiles from symmetry or antisymmetry.

10.7 Discussion

In this chapter the circular model of Loop Current Eddies developed in chapter 9 has been generalised to describe elliptic eddies. Again, the model satisfies the quasi-geostrophic equations in the far-field and is capable of generating $O(1)$ velocities when the eddy is close to a measuring station. As in the circle case, it is assumed that the eddy translates solely in the westward direction under the influence of the β-effect. However, the elliptic eddy is also allowed to precess (as it must do according to Cushman-Roisin et al. 1985 and Young 1985). The Helmholtz equation is solved exterior to the ellipse and a solution found in terms of Mathieu functions. These solutions are shown to degenerate

to the appropriate functions in the Laplacian and circle limits. Approximations to the complicated Mathieu function solutions are used and the characteristics of a precessing, translating ellipse are estimated given a time series of measured velocity data. Subsequent velocities generated by the elliptical eddy can be predicted.

As in the circle case the model has been applied to two data sets representing the passage of two Loop Current Eddies past a measuring station. Velocities predicted are compared with the real data and with those given by the circular model. As expected the ellipse and circle models predict similar velocities in the far-field, as the ellipse solution tends to that of the circle in such regions. However, the models differ when the eddy is in close proximity to the measuring station. This is because solutions of the governing equations for the ellipse model must be restricted so that the minor axis length is smaller than the major axis length. Although these solutions admit eddies of all eccentricities, the eddy sizes are significantly 'smaller' than those predicted by the circular model. Therefore, generally, the elliptical eddies do not get close enough to the measuring station to record any interior velocities which are smaller in magnitude than equivalent exterior velocities.

Differences in the circle and elliptical models are most graphically illustrated in the application to the LCE3 data. The circular model gives excellent agreement between actual and predicted velocities whereas the ellipse model overestimates the velocities in the x-direction. As mentioned in section 9.5, overestimation is not necessarily a bad thing as it is better to be cautious when deciding whether large currents may affect offshore operations.

By generalising the circular model it was hoped that the elliptic eddies would improve the predictions of chapter 9. This has not been the case. It

should be noted, however, that the precession rates calculated by the elliptic model are in excellent agreement with previous models (Cushman-Roisin et al. 1985 and Cushman-Roisin 1986) and observed eddies. Some effects of this precession are seen in the velocity profiles derived from the elliptic eddy model.

The elliptic eddy model is expected to yield more accurate predictions if the governing equations can be reformed in such a way as to allow for eddies of comparable sizes to those of the circle case. This should be an interesting investigation for further study.

Chapter 11

Conclusions

In part II, the motion of Loop Current Eddies in the Gulf of Mexico has been modeled with a view to accurately predicting the currents they produce. Motivated by concerns of the offshore oil industry where large currents can adversely affect operations, time series of velocities measured at a single location (e.g. an oil platform) were used to infer characteristics of approaching eddies.

First, a circular model of Loop Current Eddies was adopted. The model is quasi-geostrophic in the far-field and in the interior, consistent with observations, has a near solid body rotation structure (Kirwan et al. 1984b, Glenn et al. 1990). This model is capable of producing $O(1)$ velocities such as those measured in Gulf. Further, the model was found to be relatively stable to the introduction of noise.

A more realistic elliptical model was then developed. As in the circular case the shallow water equations are solved exterior to the eddy. In this case solutions involving Mathieu functions are found. Again, the exterior solution is matched to an interior solution consisting of an eddy in near solid body rotation. The elliptical model introduces more parameters, namely the ellipse

dimensions and a precession rate. When tested on synthetic data the elliptical model gives precession rates consistent with observations of Loop Current Eddies.

The work presented here is extraordinary in that data gathered in the Gulf of Mexico corresponding to the passage of several Loop Current Eddies has been made available and the models can be applied to it. The circular model predicts velocities due to a Loop Current Eddy in extremely good correlation with actual data. Differences between model predicted and actual data are due to some deformation of the Loop Current Eddy and presence of other features. The elliptic model, being more sophisticated was expected to produce even better predictions for Loop Current Eddy induced currents. This was not the case. This was due to the fact the equations solved for the ellipse do not permit 'large' eddies and therefore predicted currents are due to the exterior solution solution only. These tend to overestimate the magnitudes of the velocities.

It would be desirable to resolve the problem that, according to the governing equations, ellipses cannot be 'large'. If this problem were to be solved, it is expected that the ellipse solutions would provide more accurate predictions.

Furthermore, the present work considers eddies which translate solely westward at a constant velocity. Recently 'sprints' and 'stalls' in the passage of Loop Current Eddies have been observed (Hamilton et al. 1999). The work here should be extended to include such variations in the translation velocity. It is also noted that the paths of Loop Current Eddies often deviate from due westward, i.e. they have a significant southward component (figure 8.1). This may be due to the influence of the topography of the Gulf of Mexico and such effects could be included.

It would also be desirable to examine the fate of Loop Current Eddies

as they approach the western boundary of the Gulf of Mexico and interact with older Loop Current Eddies and the steep topography there. This could combine the vortex-topography interaction work of part I, including heton and dipole studies, with the Loop Current Eddy modeling of part II.

Part III

Appendices

Appendix A

Expansions of Mathieu functions

The functions $\mathrm{ce}_n(\phi, -q)$ and $\mathrm{se}_n(\phi, -q)$ can be expanded in series of trigonometric functions (see McLachlan 1947), i.e.

$$\mathrm{ce}_{2n}(\phi, -q) = (-1)^n \sum_{r=0}^{\infty} (-1)^r A_{2r}^{(2n)} \cos(2r\phi), \tag{A.1}$$

$$\mathrm{ce}_{2n+1}(\phi, -q) = (-1)^n \sum_{r=0}^{\infty} (-1)^r B_{2r+1}^{(2n+1)} \cos((2r+1)\phi), \tag{A.2}$$

$$\mathrm{se}_{2n+1}(\phi, -q) = (-1)^n \sum_{r=0}^{\infty} (-1)^r A_{2r+1}^{(2n+1)} \sin((2r+1)\phi), \tag{A.3}$$

$$\mathrm{se}_{2n+2}(\phi, -q) = (-1)^n \sum_{r=0}^{\infty} (-1)^r B_{2r+2}^{(2n+2)} \sin((2r+2)\phi), \tag{A.4}$$

where $A_r^{(n)}$ and $B_r^{(n)}$ are constants relating to the Mathieu characteristics, a_n and b_n and depend on the value of q, i.e. the physical properties of the ellipse.

Also, the functions $\mathrm{Fek}_n(\xi, -q)$ and $\mathrm{Gek}_n(\xi, -q)$ can be expanded in series of Bessel functions, i.e.

$$\mathrm{Fek}_{2n}(\xi, -q) = \frac{p'_{2n}}{\pi A_0^{(2n)}} \sum_{r=0}^{\infty} A_{2r}^{(2n)} I_r(\sqrt{q}e^{-\xi}) K_r(\sqrt{q}e^{\xi}), \tag{A.5}$$

$$\mathrm{Fek}_{2n+1}(\xi,-q)=\frac{s'_{2n+1}}{\pi B_1^{(2n+1)}}\sum_{r=0}^{\infty}B_{2r+1}^{(2n+1)}\left(I_r(\sqrt{q}e^{-\xi})K_{r+1}(\sqrt{q}e^{\xi})\right.$$
$$\left.-I_{r+1}(\sqrt{q}e^{-\xi})K_r(\sqrt{q}e^{\xi})\right), \quad \text{(A.6)}$$

$$\mathrm{Gek}_{2n+1}(\xi,-q)=\frac{p'_{2n+1}}{\pi A_1^{(2n+1)}}\sum_{r=0}^{\infty}A_{2r+1}^{(2n+1)}\left(I_r(\sqrt{q}e^{-\xi})K_{r+1}(\sqrt{q}e^{\xi})\right.$$
$$\left.+I_{r+1}(\sqrt{q}e^{-\xi})K_r(\sqrt{q}e^{\xi})\right), \quad \text{(A.7)}$$

$$\mathrm{Gek}_{2n+2}(\xi,-q)=\frac{s'_{2n+2}}{\pi B_2^{(2n+2)}}\sum_{r=0}^{\infty}B_{2r+2}^{(2n+2)}\left(I_r(\sqrt{q}e^{-\xi})K_{r+2}(\sqrt{q}e^{\xi})\right.$$
$$\left.-I_{r+2}(\sqrt{q}e^{-\xi})K_r(\sqrt{q}e^{\xi})\right), \quad \text{(A.8)}$$

where,

$$p'_{2n}=\frac{(-1)^n\mathrm{ce}_{2n}(0,q)\mathrm{ce}_{2n}(\frac{\pi}{2},q)}{A_0^{(2n)}}, \quad \text{(A.9)}$$

$$s'_{2n+1}=\frac{(-1)^n\mathrm{se}'_{2n+1}(0,q)\mathrm{se}_{2n+1}(\frac{\pi}{2},q)}{\sqrt{q}B_1^{(2n+1)}}, \quad \text{(A.10)}$$

$$p'_{2n+1}=\frac{(-1)^{n+1}\mathrm{ce}_{2n+1}(0,q)\mathrm{ce}'_{2n+1}(\frac{\pi}{2},q)}{\sqrt{q}A_1^{(2n+1)}}, \quad \text{(A.11)}$$

and

$$s'_{2n+2}=\frac{(-1)^{n+1}\mathrm{se}'_{2n+2}(0,q)\mathrm{se}'_{2n+2}(\frac{\pi}{2},q)}{qB_2^{(2n+2)}}. \quad \text{(A.12)}$$

Note, the dashes in the right-hand sides of equations (A.9)–(A.12) denote differentiation with respect to the angular coordinate, ϕ.

It can also be shown that

$$\mathrm{ce}_{2n}(0,0)=1, \quad \text{(A.13a)}$$

$$\mathrm{ce}_{2n}\left(\frac{\pi}{2},0\right)=1, \quad \text{(A.13b)}$$

$$\mathrm{se}'_{2n+1}(0,0)=2n+1, \quad \text{(A.13c)}$$

$$\mathrm{se}_{2n+1}\left(\frac{\pi}{2},0\right)=(-1)^n. \quad \text{(A.13d)}$$

Bibliography

M. Abramowitz and I. Stegun. *Handbook of Mathematical Functions.* Dover, New York, 1964.

L. Armi and E. D'Asaro. Flow structures of the benthic ocean. *J. Geophys. Res.*, 85(C1):469–484, 1980.

G. K. Batchelor. *An Introduction to Fluid Dynamics.* Cambridge University Press, 1967.

J-. O. Beismann, R. H. Käse, and J. R. E. Lutjeharms. On the influence of submarine ridges on translation and stability of Agulhas rings. *J. Geophys. Res.*, 104(C4):7897–7906, 1999.

G. I. Bell. Interaction between vortices and waves in a simple model of geophysical flow. *Phys. Fluids A*, 2(4):575–586, 1990.

E. S. Benilov. Beta-induced translation of strong isolated eddies. *J. Phys. Oceanogr.*, 26:2223–2229, 1996.

P. R. Bevington and D. K. Robinson. *Data Reduction and Error Analysis for the Physical Sciences.* McGraw-Hill, 3rd edition, 2003.

D. A. Byrne, A. L. Gordon, and W. F. Haxby. Agulhas eddies: A synoptic view using Geosat ERM data. *J. Phys. Oceanogr.*, 25:902–917, 1995.

G. F. Carnevale, O. U. Velasco Fuentes, and P. Orlandi. Inviscid dipole-vortex rebound from a wall or coast. *J. Fluid Mech.*, 351:75–103, 1997.

S.-Y. Chao and P.-T. Shaw. Slope-enhanced fission of salty hetons under sea ice. *J. Phys. Oceanogr.*, 30:2866–2882, 2000.

D. B. Chelton and M. G. Schlax. Global observations of oceanic Rossby waves. *Science*, 272(5259):234–238, 1996.

P. Cipollini, D. Cromwell, M. S. Jones, G. D. Quartly, and P. G. Challenor. Concurrent altimeter and infrared observations of Rossby wave propagation near 34°N in the Northeast Atlantic. *Geophys. Res. Lett.*, 24(8):889–892, 1997.

C. K. Cooper, G. Z. Forristall, and T. M. Joyce. Velocity and hydrographic structure of two Gulf of Mexico warm-core rings. *J. Geophys. Res.*, 95(C2): 1663–1679, 1990.

Y. Couder and C. Basdevant. Experimental and numerical study of vortex couples in two-dimensional flows. *J. Fluid Mech.*, 173:225–251, 1986.

B. Cushman-Roisin. Frontal geostrophic dynamics. *J. Phys. Oceanogr.*, 16: 132–143, 1986.

B. Cushman-Roisin, E. P. Chassignet, and B. Tang. Westward motion of mesoscale eddies. *J. Phys. Oceanogr.*, 20:758–768, 1990.

B. Cushman-Roisin, W. H. Heil, and D. Nof. Oscillations and rotations of elliptical warm-core rings. *J. Geophys. Res.*, 90(C6):11756–11764, 1985.

W. P. M. de Ruijter, A. Biastoch, S. S. Drijfhout, J. R. E. Lutjeharms, R. P. Matano, T. Pichevin, P. J. van Leeuwen, and W. Weijer. Indian-Atlantic

interocean exchange: Dynamics, estimation and impact. *J. Geophys. Res.*, 104(C9):20885–20910, 1999.

D. G. Dritschel. The stability and energetics of corotating uniform vortices. *J. Fluid Mech.*, 157:95–134, 1985.

D. G. Dritschel. Contour surgery: A topological reconnection scheme for extended integrations using contour dynamics. *J. Comput. Phys.*, 77:240–266, 1988.

D. G. Dritschel and M. H. P. Ambaum. A contour-advective semi-Lagrangian numerical algorithm for simulating fine-scale conservative dynamical fields. *Q. J. R. Met. Soc.*, 123:1097–1130, 1997.

C. M. Duncombe Rae, S. L. Garzoli, and A. L. Gordon. The eddy field of the southeast Atlantic ocean: A statistical census from the Benguela sources and transports project. *J. Geophys. Res.*, 101(C5):11949–11964, 1996.

D. C. Dunn. The evolution of an initially circular vortex near an escarpment. Part II: Numerical results. *Eur. J. Mech. B Fluids*, pages 677–699, 2002.

D. C. Dunn, N. R. McDonald, and E. R. Johnson. The motion of a singular vortex near an escarpment. *J. Fluid Mech.*, 448:335–365, 2001.

D. C. Dunn, N. R. McDonald, and E. R. Johnson. The evolution of an initially circular vortex near an escarpment. Part I: Analytical results. *Eur. J. Mech. B Fluids*, pages 657–675, 2002.

B. A. Elliott. Anticyclonic Rings in the Gulf of Mexico. *J. Phys. Oceanogr.*, 12:1292–1309, 1982.

G. R. Flierl. A simple model for the structure of warm and cold core rings. *J. Geophys. Res.*, 84(C2):781–785, 1979.

G. Z. Forristall, K. J. Schaudt, and C. K. Cooper. Evolution and kinematics of a Loop Current Eddy in the Gulf of Mexico during 1985. *J. Geophys. Res.*, 97(C2):2173–2184, 1992.

Fugro GEOS. BHP Atwater Valley Block 618 Current Data. Technical report, Fugro GEOS Reference B79013_D001, 2003.

A. E. Gill. *Atmosphere-Ocean Dynamics.* Academic Press, 1982.

S. M. Glenn, G. Z. Forristall, P. Cornillon, and G. Milkowski. Observations of Gulf Stream Ring 83-E and their interpretation using feature models. *J. Geophys. Res.*, 95(C8):13043–13063, 1990.

K. A. Gorshkov, L. A. Ostrovsky, and I. A. Soustova. Perturbation theory for Rankine vortices. *J. Fluid Mech.*, 404:1–25, 2000.

I. S. Gradshteyn and I. M. Ryzhik. *Table Of Integrals, Series and Products.* Academic Press, Inc., 5th edition, 1994.

M. L. Gründlingh. Tracking eddies in the southeast Atlantic and southwest Indian oceans with TOPEX/POSEIDON. *J. Geophys. Res.*, 100(C12):24977–24986, 1995.

V. M. Gryanik, T. N. Doronina, D. J. Olbers, and T. H. Warncke. The theory of three-dimensional hetons and vortex-dominated spreading in localized turbulent convection in a fast rotating stratified fluid. *J. Fluid Mech.*, 423: 71–125, 2000.

P. Hamilton. Lower continental slope cyclonic eddies in the central Gulf of Mexico. *J. Geophys. Res.*, 97(C2):2185–2200, 1992.

P. Hamilton, G. S. Fargion, and D. C. Biggs. Loop Current eddy paths in the Western Gulf of Mexico. *J. Phys. Oceanogr.*, 29:1180–1207, 1999.

S. Herbette, Y. Morel, and M. Arhan. Erosion of a surface vortex by a seamount. *J. Phys. Oceanogr.*, 33:1664–1679, 2003.

J. S. Hesthaven, J. P. Lynov, and J. Nycander. Dynamics of nonstationary dipole vortices. *Phys. Fluids A*, 5(3):622–629, 1993.

N. G. Hogg and H. M. Stommel. The heton, an elementary interaction between discrete baroclinic geostrophic vortices, and its implications concerning eddy heat-flow. *Proc. R. Soc. Lond.* A, 397:1–20, 1985.

E. R. Johnson and N. R. McDonald. The motion of a vortex near a gap in a wall. *Phys. Fluids*, 16:462–469, 2004a.

E. R. Johnson and N. R. McDonald. The motion of a vortex near two circular cylinders. *Proc. Roy. Soc. A*, 460:939–954, 2004b.

E. R. Johnson and N. R. McDonald. Surf zone vortices over stepped topography. *J. Fluid Mech.*, 511:265–283, 2004c.

T. M. Joyce. Velocity and hydrographic structure of a Gulf Stream warm-core ring. *J. Phys. Oceanogr.*, 14:936–947, 1984.

E. T. Kirkpatrick. Tables of values of the modified Mathieu functions. *Math. of Computation*, 14(70):118–129, 1960.

A. D. Kirwan, Jr., W. J. Merrell, Jr., J. K. Lewis, and R. E. Whitaker. Lagrangian observations of an anticyclonic ring in the Western Gulf of Mexico. *J. Geophys. Res.*, 89(C3):3417–3424, 1984a.

A. D. Kirwan, Jr., W. J. Merrell, Jr., J. K. Lewis, R. E. Whitaker, and R. Legeckis. A model for the analysis of drifter data with an application to a warm core ring in the Western Gulf of Mexico. *J. Geophys. Res.*, 89(C3):3425–3438, 1984b.

J. S.-L. Lam and D. G. Dritschel. On the beta-drift of an initially circular vortex patch. *J. Fluid Mech.*, 436:107–129, 2001.

H. Lamb. *Hydrodynamics.* Cambridge University Press, 6th edition, 1932.

S. Legg and J. Marshall. A heton model of the spreading phase of open-ocean deep convection. *J. Phys. Oceanogr.*, 23:1040–1056, 1993.

N. R. McDonald. The decay of cyclonic eddies by Rossby wave radiation. *J. Fluid Mech.*, 361:237–252, 1998a.

N. R. McDonald. The motion of an intense vortex near topography. *J. Fluid Mech.*, 367:359–377, 1998b.

N. R. McDonald. The motion of geophysical vortices. *Phil. Trans. R. Soc. Lond.* A, 357:3427–3444, 1999.

N. R. McDonald and D. C. Dunn. Some interactions of a vortex with a seamount. *Il Nuovo Cimento*, 22(C6):885–898, 1999.

M. E. McIntyre. The stratospheric polar vortex and sub-vortex: fluid dynamics and midlatitude ozone loss. *Proc. R. Soc. Lond.* A, 352:227–240, 1995.

N. W. McLachlan. *Theory and application of Mathieu functions.* Oxford University Press, 1947.

J. C. McWilliams. The vortices of geostrophic turbulence. *J. Fluid Mech.*, 219: 387–404, 1990a.

J. C. McWilliams. The vortices of two-dimensional turbulence. *J. Fluid Mech.*, 219:361–385, 1990b.

W. J. Merrell, Jr. and J. M. Morrison. On the circulation of the Western Gulf of Mexico with observations from April 1978. *J. Geophys. Res.*, 86(C5): 4181–4185, 1981.

NBS. *Tables relating to Mathieu functions.* The Computation Laboratory of the National Applied Mathematics Laboratories National Bureau of Standards, New York Columbia University Press, 1951.

J. Nycander and M. B. Isichenko. Motion of dipole vortices in a weakly inhomogeneous medium and related convective transport. *Phys. Fluids B*, 2(9): 2042–2047, 1990.

P. Orlandi. Vortex dipole rebound from a wall. *Phys. Fluids A*, 2(8):1429–1436, 1990.

J. Pedlosky. *Geophysical Fluid Dynamics.* Springer, 2nd edition, 1987.

W. H. Press, S. A. Teukolsky, W. T. Vetterling, and B. P. Flannery. *Numerical Recipes in Fortran 77: The Art of Scientific Computing.* Cambridge University Press, 2nd edition, 1992.

G. M. Reznik. Dynamics of singular vortices on a beta-plane. *J. Fluid Mech.*, 240:405–432, 1992.

G. M. Reznik, R. Grimshaw, and E. S. Benilov. On the long-term evolution of an intense localized divergent vortex on the beta-plane. *J. Fluid Mech.*, 422:249–280, 2000.

G. Richardson. Vortex motion in shallow water with varying bottom topography and zero Froude number. *J. Fluid Mech.*, 411:351–374, 2000.

P. G. Saffman. The approach of a vortex pair to a plane surface in inviscid fluid. *J. Fluid Mech.*, 92:497–503, 1979.

W. J. Schmitz, Jr. On the circulation in and around the Gulf of Mexico - Volume I: A review of the deep water circulation, 2004. URL `http://deeweb.cbi.tamucc.edu/gomcirculation/`.

M. E. Stern and G. R. Flierl. On the interaction of a vortex with a shear flow. *J. Geophys. Res.*, 92(C10):10733–10744, 1987.

G. G. Sutyrin and G. R. Flierl. Intense vortex motion on the beta plane: Development of the beta gyres. *J. Atmos. Sci.*, 51:773–790, 1994.

G. G. Sutyrin, I. Ginis, and S. A. Frolov. Equilibration of baroclinic meanders and deep eddies in a Gulf Stream-type jet over a sloping bottom. *J. Phys. Oceanogr.*, 31:2049–2065, 2001.

G. G. Sutyrin, G. D. Rowe, L. M. Rothstein, and I. Ginis. Baroclinic eddy interactions with continental slopes and shelves. *J. Phys. Oceanogr.*, 33: 283–291, 2003.

V. Thierry and Y. Morel. Influence of a strong bottom slope on the evolution of a surface-intensified vortex. *J. Phys. Oceanogr.*, 28:911–924, 1999.

L. Thompson. Two-layer quasigeostrophic flow over finite isolated topography. *J. Phys. Oceanogr.*, 23:1297–1314, 1993.

S. Valcke and J. Verron. Interactions of baroclinic isolated vortices: The dominant effect of shielding. *J. Phys. Oceanogr.*, 27:524–541, 1997.

F. O. Vandermeirsch, X. J. Carton, and Y. G. Morel. Interaction between an eddy and a zonal jet Part I. One-and-a-half-layer model. *Dyn. Atmos. Oceans*, 36:247–270, 2003.

V. M. V. Vidal, F. V. Vidal, A. F. Hernández, E. Meza, and J. M. Pérez-Molero. Baroclinic flows, transports, and kinematic properties in a cyclonic-anticyclonic-cyclonic ring triad in the Gulf of Mexico. *J. Geophys. Res.*, 99(C4):7571–7597, 1994.

F. M. Vukovich and B. W. Crissman. Aspects of warm rings in the Gulf of Mexico. *J. Geophys. Res.*, 91(C2):2645–2660, 1986.

X. Wang. *Interaction of an eddy with a continental slope.* PhD thesis, M.I.T./W.H.O.I. Joint Program in Oceanography, 1992. 216 pp.

B. A. Warren. Notes on translatory movement of rings of current with application to Gulf Stream eddies. *Deep-Sea Res.*, 14:505–524, 1967.

A. J. White and N. R. McDonald. The motion of a point vortex near large amplitude topography in a two-layer fluid. *J. Phys. Oceanogr.*, 34:2808–2824, 2004.

W. R. Young. Some interactions between small numbers of baroclinic, geostrophic vortices. *Geophys. Astrophys. Fluid Dynamics*, 33:35–61, 1985.

W. R. Young. Elliptical vortices in shallow water. *J. Fluid Mech.*, 171:101–119, 1986.

N. J. Zabusky, M. H. Hughes, and K. V. Roberts. Contour dynamics for the Euler equations in two dimensions. *J. Comput. Phys.*, 30:96–106, 1979.

N. J. Zabusky and J. C. McWilliams. A modulated point-vortex model for geostrophic, β-plane dynamics. *Phys. Fluids*, 25(12):2175–2182, 1982.

L. Zavala Sansón. Vortex-ridge interaction in a rotating fluid. *Dyn. Atmos. Oceans*, 35:299–325, 2002.

L. Zavala Sansón and G. J. F. van Heijst. Interaction of barotropic vortices with coastal topography: Laboratory experiments and numerical simulations. *J. Phys. Oceanogr.*, 30:2141–2162, 2000.

L. Zavala Sansón, G. J. F. van Heijst, and J. J. J. Doorschoot. Reflection of barotropic vortices from a step-like topography. *Il Nuovo Cimento*, 22(C6): 909–929, 1999.